

# Modeling Multi-Scale Deformation Cycles in Subduction Zones with a Continuum Visco-Elastic-Brittle Framework

Véronique Dansereau<sup>1</sup>, Nikolai M. Shapiro<sup>2</sup>, Michel Campillo<sup>3</sup>, and Jérôme Weiss<sup>4</sup>

<sup>1</sup>Institut des Sciences de la Terre , Université Grenoble Alpes, CNRS UMR 5275

<sup>2</sup>Institut de Sciences de la Terre, Université Grenoble Alpes, CNRS

<sup>3</sup>Université Joseph Fourier, Grenoble

<sup>4</sup>French National Centre for Scientific Research (CNRS)

March 16, 2023

## Abstract

The overwhelming amount of seismic, geodesic and in-situ observations accumulated over the last 30 years clearly indicate that, from a mechanical point of view, faults should be considered as both damageable elastic solids in which highly localized features emerge as a result of very short-term brittle processes and materials experiencing ductile strains distributed in large volumes and over long time scales. The interplay of both deformation mechanisms, brittle and ductile, give rise to transient phenomena associating slow slip and tremors, known as slow earthquakes, which dissipate a significant amount of stress in the fault system. The physically-based numerical models developed to improve our comprehension of the mechanical and dynamical behaviour of faults must therefore have the capacity to treat simultaneously both deformation mechanisms and to cover a wide range of time scales in a numerically efficient manner. This capability is essential, both for simulating accurately their deformation cycles and for improving our interpretation of the available observations.

In this paper, we present a numerically efficient visco-elasto-brittle numerical framework that can simulate transient deformations akin to that observed in the context of subduction zones, over the wide range of time scales relevant for slow earthquakes. We implement the model in idealized simple shear simulations and explore the sensitivity of its behavior to the value of its main mechanical parameters.

1                   **Modeling Multi-Scale Deformation Cycles in**  
2                   **Subduction Zones with a Continuum**  
3                   **Visco-Elastic-Brittle Framework**

4                   **Véronique Dansereau<sup>1</sup>, Nikolai Shapiro<sup>1</sup>, Michel Campillo<sup>1</sup>, Jérôme Weiss<sup>1</sup>**

5                   <sup>1</sup>Institut des Sciences de la Terre, Université Grenoble Alpes, CNRS (5275), Grenoble, France

6                   **Key Points:**

- 7                   • We present a continuum model for the deformation of faults in which the mechan-  
8                   ical strength vary continuously as a function of the damage.  
9                   • The model's numerical scheme allows covering the very short and very long time  
10                  scale processes involved in the slow earthquake phenomenon.  
11                  • The model reproduces different types of transient deformations, akin to slow and  
12                  classical earthquakes in subduction zones.

---

Corresponding author: Véronique Dansereau, [veronique.dansereau@univ-grenoble-alpes.fr](mailto:veronique.dansereau@univ-grenoble-alpes.fr)

**Abstract**

The overwhelming amount of seismic, geodesic and in-situ observations accumulated over the last 30 years clearly indicate that, from a mechanical point of view, faults should be considered as both damageable elastic solids in which highly localized features emerge as a result of very short-term brittle processes and materials experiencing ductile strains distributed in large volumes and over long time scales. The interplay of both deformation mechanisms, brittle and ductile, give rise to transient phenomena associating slow slip and tremors, known as slow earthquakes, which dissipate a significant amount of stress in the fault system. The physically-based numerical models developed to improve our comprehension of the mechanical and dynamical behaviour of faults must therefore have the capacity to treat simultaneously both deformation mechanisms and to cover a wide range of time scales in a numerically efficient manner. This capability is essential, both for simulating accurately their deformation cycles and for improving our interpretation of the available observations.

In this paper, we present a numerically efficient visco-elasto-brittle numerical framework that can simulate transient deformations akin to that observed in the context of subduction zones, over the wide range of time scales relevant for slow earthquakes. We implement the model in idealized simple shear simulations and explore the sensitivity of its behaviour to the value of its main mechanical parameters.

**Plain Language Summary**

The outer part of the Earth, called the lithosphere, is a complex object that deforms both in a solid and a fluid manner. Where tectonic plates meet, such as in fault zones, this duality gives rise to a variety of phenomena. The solid behaviour is associated with earthquakes and very sudden slip movements of the fault that we feel at the surface. The fluid behaviour translates into a slow and steady slip at depth. In between, the mixed solid-fluid behaviour results in progressive accelerations and decelerations of the fault slip accompanied with very weak quakes, which are called *slow earthquakes*. These slow earthquakes modulate the deformation cycle of faults and most probably impact the occurrence of "real", or *classical*, earthquakes. It is therefore important to account for them in numerical models that aim to help us understand this cycle better. In this paper we present a model of the deformation of fault zones that we have developed with the particular goal of representing slow earthquakes and that allows the lithosphere to behave sometimes like a solid, sometimes like a fluid.

**1 Introduction**

Earth's materials are known to exhibit a variety of deformation mechanisms depending on temperature, pressure and loading conditions as well as on the time and spatial scales at which they are observed (e.g., Burov, 2011). In the most dynamic parts of the Earth's lithosphere, such as plate boundaries and fault zones, volcanic systems and landslides, the interplay between different mechanisms can result in a strong strain localization and a complex temporal behaviour. The slow deformation occurring over geological time scales can indeed be suddenly accelerated and give rise to catastrophic events (earthquakes, eruptions, landslides) that release huge amounts of energy in a very short time.

Historically, the deformation of the lithosphere has been studied either at the short time scales (seconds to minutes) of these catastrophic events or at the very large time scales (years to millions of years) of plate tectonic motion. However, the technological progresses in observational systems over the last 30 years has brought about a revolution in the comprehension of its dynamical behaviour, by allowing to explore the time scales in between. Global Positioning System (GPS), radar interferometry (Synthetic Aper-

62 ture Radar, InSAR) and satellite gravimetry data have indeed driven a huge leap for-  
 63 ward in terms of measuring the deformation of the Earth surface continuously in time  
 64 and space and at high resolution. These new geodetic observations have been accompa-  
 65 nished by rapid deployments of dense seismic networks and by the emergence of novel meth-  
 66 ods of analysis of continuous seismic data that allow exploring deformation mechanisms  
 67 over a significantly wider range of time scales.

68 In the case of earthquakes, the occurrence of co-seismic rupture processes that re-  
 69 redistribute Coulomb stresses over short time scales (on the order of seconds) and the as-  
 70 sociated scaling properties have been established for a long time (Omori, 1894; Guten-  
 71 berg & Richter, 1949; Turcotte, 1992). However, the recent advances in the observational  
 72 systems and data analysis methods have profoundly modified our vision of how plate tec-  
 73 tonic motions are accommodated and how stresses are dissipated along faults. In par-  
 74 ticular, the combination of high resolution geodetic and seismic data has resulted in im-  
 75 proved tracking of co-, post- and inter-seismic deformation patterns (e.g., K. Wang et  
 76 al., 2012) and in the discovery of new types of transient phenomena designated as “slow  
 77 earthquakes”. These slow earthquakes, associated because of their triggering depth with  
 78 the so-called brittle-ductile transition comprised between the brittle, seismic zone near  
 79 the surface and the ductile, aseismic zone below (e.g., Dragert et al., 2004; Peng & Gomberg,  
 80 2010; Obara & Kato, 2016, and many others), combine periodic accelerations of the fault  
 81 slip with weak seismic radiations known as tectonic tremors (e.g., Dragert et al., 2001;  
 82 Obara, 2002; Peng & Gomberg, 2010). Analyses based on the cross-correlations of am-  
 83 bient seismic noise have demonstrated that the transient deformations accompanying both  
 84 slow and major earthquakes are associated with changes in elastic properties of the ma-  
 85 terial in the vicinity of the fault, reminiscent of damaging processes and of a non-elastic,  
 86 or at least nonlinear elastic behaviour (e.g., Brenguier et al., 2008; Rivet et al., 2011; Q.-  
 87 Y. Wang et al., 2019). Seismic data (e.g., Audet et al., 2009), along with other sources  
 88 such as tomographic imagery (Shelly et al., 2006) and the observation of exhumed sub-  
 89 duction zones (Angiboust et al., 2015), have also allowed identifying fluids as another  
 90 major player in the transient deformation of faults. In the context of slow earthquakes  
 91 in particular, the increased pore-pressure from fluids trapped in the fault zone and as-  
 92 sociated pore-pressure variations and diffusion are indeed believed to partially control  
 93 the seismic and slow slip activity via the weakening and fracturing of the host rock, the  
 94 local reduction of the effective stress and friction along the shearing plane and the trig-  
 95 gering and migration of tremors (e.g., Brown et al., 2005; Frank, Shapiro, et al., 2015;  
 96 Shapiro et al., 2018; Cruz-Atienza et al., 2018; Dublanchet, 2019; Luo & Liu, 2019, 2021,  
 97 and many others).

## 98 1.1 Existing Modelling Approaches

99 The direct modelling approaches that exist to model the deformation of the Earth’s  
 100 lithosphere and faults in particular can be divided in several categories.

101 The first includes continuum frameworks based on a fluid mechanics approach, namely  
 102 viscous, visco-elastic, visco-plastic or elasto-visco-plastic models. Such models have been  
 103 developed to represent the diffuse, ductile and potentially large deformations associated  
 104 with plate tectonics motion, for instance the formation of mountain ranges and conti-  
 105 nental rifts (e.g., Royden et al., 1997; Frederiksen & Braun, 2001; Popov & Sobolev, 2008).  
 106 They can reproduce strain localization by including strain-weakening mechanisms, such  
 107 as a non-linear dependence of the viscous strain rate on the stress and thermo-mechanical  
 108 feedbacks. However, their applications are restricted to ductile deformations on geolog-  
 109 ical time scales. In the context of faults, visco-elastic models of the Maxwell or Burg-  
 110 ers type (see figure 1) have also been often used to represent the mechanical behaviour  
 111 of the combined Earth’s crust and mantle system (e.g. Nur & Mavko, 1974; Pollitz et  
 112 al., 2001; Pollitz, 2003, 2005; Hetland & Hager, 2005, 2006; K. Wang et al., 2012; Sun  
 113 & Wang, 2015). In such frameworks, the Maxwell component represents the lithosphere,

114 which can elastically transmit stresses over short time scales, while relaxing stresses in  
 115 an exponential manner over very long time scales. The Kelvin component is added to  
 116 represents the more ductile asthenosphere, which hosts mantle convection and is thought  
 117 to cause a delayed elastic response, measurable in the reversal of surface velocities after  
 118 after a major earthquake (e.g., Sun & Wang, 2015). However, with constant mechanical  
 119 parameters (elastic moduli and viscosities), these models cannot by themselves account  
 120 for the rheological stratification of fault zones, nor for the presence of a relatively localized  
 121 shearing zone that concentrates the deformation. They are therefore usually implemented  
 122 in "layered" frameworks (e.g., Hetland & Hager, 2005, 2006; K. Wang et al., 2012;  
 123 Sun & Wang, 2015), in which the structure of the system is prescribed and divided in  
 124 multiple pre-determined layers with different rheologies (e.g., an elastic layer of crust embedded  
 125 in a visco-elastic mantle) and is thus not allowed to evolve in time. With constant  
 126 mechanical parameters also, neither the Maxwell nor the Burgers model can reproduce  
 127 the transient deformations of fault systems over a wide enough range of time  
 128 scales (Ingleby & Wright, 2017; Periollat et al., 2022): deformations which translate for  
 129 instance in an Omori-like decay of post-seismic surface velocity (velocity inversely proportional  
 130 to the time since the earthquake), observed hours to ten of years after moderate to large  
 131 continental earthquakes (Ingleby & Wright, 2017).

132 A second category of models aim to represent the transition between stable and  
 133 unstable deformation regimes within the Earth crust by assimilating brittle and frictional  
 134 processes to the problem of friction on a material interface. This is the case for the well-  
 135 known block-slider framework, a parametric model stemming from experimental studies  
 136 of the frictional behaviour of various materials including rocks, which combines the  
 137 principle of linear elasticity and non-linear stick-slip friction between a sliding block and  
 138 an underlying surface. Purely conceptual models including these basic ingredients have  
 139 first been used to explain the statistical properties associated with major earthquakes,  
 140 such as the Gutenberg-Richter law (e.g., Burridge & Knopoff, 1967; Carlson & Langer,  
 141 1989). The rheology of frictional interfaces has been later formulated as a constitutive  
 142 law known as "rate-and-state friction" (Dieterich, 1978, 1979a, 1979b) which has been  
 143 widely used to model fault instabilities and earthquakes (e.g., Liu & Rice, 2005; Segall  
 144 & Bradley, 2012, and many others). This law establishes the following relation between  
 145 the measured friction coefficient,  $\mu$ , the sliding velocity,  $V$ , and the state of the slip plane,  
 146  $\theta$ :

$$147 \quad \mu(\theta, V) = \mu^* + a \ln \frac{V}{V^*} + b \ln \frac{V^* \theta}{D_c}$$

148 where  $\mu^*$  is a friction coefficient at a reference sliding velocity,  $V^*$ ,  $a$  and  $b$  are proportional-  
 149 ity constants for the magnitude of instantaneous and time-dependant displacements  
 150 respectively and  $D_c$  is a characteristic slip distance for the evolution of the system towards  
 151 a new stable state. It is often coupled to an evolution equation for the state parameter,  
 152  $\theta$ , which describes aging effects (Dieterich, 1979a; Ruina, 1983). For negative  
 153 values of  $(a-b)$ , the model describes a decrease of the friction coefficient with increasing  
 154 sliding velocity and hence an unstable, velocity-weakening state, assimilated to a brittle,  
 155 seismic behaviour. For positive values of  $(a-b)$ , it describes an increase of the friction  
 156 coefficient with the slip velocity, therefore a state of stable, velocity-hardening slip,  
 157 assimilated to an aseismic, ductile behaviour. By including additional levels of complexity  
 158 relevant to faults, which allow a change of sign of  $(a-b)$  along the interface (for instance,  
 159 a dependence of  $a$  and  $b$  on the temperature), this model can also reproduce transitions  
 160 between a brittle and a ductile behaviour and transient slip events (Liu & Rice,  
 161 2005, 2007; Segall & Bradley, 2012). Its main limitation, however, is that it is empirically-  
 162 based. As such, its extrapolation to the temporal and spatial scales of geophysical systems  
 163 such as faults on the basis of the results obtained in the laboratory is not trivial  
 164 and questionable (e.g., Chen et al., 2017; van den Ende et al., 2018). A second important  
 165 limitation is that it is an interface rheology, which implies a prescribed, non-evolving  
 166 location of the sliding plane and which does not take into account its microstructure or  
 167 its volumetric deformation. By this fact, it presents a limit to which it can be enriched

168 to include the highly relevant physico-chemical, mineralogical and hydro-mechanical pro-  
 169 cesses involved in the fault deformation cycle. It is also important to note that a "fault  
 170 plane" approach is in contradiction with seismic data and geological observations of ex-  
 171 humed faults, which suggest that the deformation occurs within a core zone made of gouge,  
 172 sandwiched between a metric to kilometric-scale zone of damaged rocks (Caine et al.,  
 173 1996; Angiboust et al., 2015; Hayman & Lavier, 2014; Gao & Wang, 2017).

174 Another category of models include continuum mechanics damage frameworks (e.g.,  
 175 Ashby & Sammis, 1990; Lyakhovsky, Reches, et al., 1997; Tang, 1997; Amitrano et al.,  
 176 1999; Bhat et al., 2012, and many others). So-called elasto-brittle schemes, which cou-  
 177 ple a damage variable to an elastic constitutive law, has indeed been used to represent  
 178 the fracturing processes and the associated strong localization of the deformation in faults  
 179 (e.g. Lyakhovsky, Ben-Zion, & Agnon, 1997; Lyakhovsky et al., 2001; Ben-Zion & Lyakhovsky,  
 180 2002, and later papers). Without accounting for the *dynamic* propagation of fractures  
 181 nor the generation of seismic waves, these models represent the redistribution of elas-  
 182 tic stresses caused by the generation and coalescence of micro-fractures and the complex  
 183 mechanical interactions in the material that stem from its micro-structural heterogene-  
 184 ity. They thereby present the advantage of simulating the emergence of a damaged shear-  
 185 ing or sliding zone (without the need to prescribe its location or geometry), the stable  
 186 to unstable transition of the system that precedes the macroscopic rupture as well as the  
 187 scaling laws associated with the localization of the deformation and the spatio-temporal  
 188 clustering of the seismic activity (e.g., Ben-Zion & Lyakhovsky, 2002; Turcotte et al.,  
 189 2003; Shcherbakov et al., 2005). An intrinsic limitation of such schemes, however, is that  
 190 they are based on an elastic constitutive law and as such, they cannot simulate any pre-  
 191 or post-rupture permanent deformation in the material. By this fact, it cannot repro-  
 192 duce the entire deformation cycle of faults. Hamiel et al., (Hamiel et al., 2004) and Dansereau  
 193 et al., (Dansereau et al., 2016a) therefore elaborated from elasto-brittle frameworks by  
 194 adding a viscous relaxation term that is coupled to the local level of damage in order to  
 195 represent, respectively, the small irreversible deformation that accumulate towards the  
 196 macro-rupture and the permanent and potentially large post-rupture deformation of the  
 197 fractured material. Their visco-elasto-brittle models have been shown to successfully sim-  
 198 ulate the scaling laws associated with brittle deformations in faults (e.g., Ben-Zion & Lyakhovsky,  
 199 2006) and a mechanically similar system: sea ice (Dansereau et al., 2016a; Rampal et  
 200 al., 2019; Ólason et al., 2021). However, in the context of faults, the numerically-coupled  
 201 treatment of damage propagation and viscous relaxation in these models makes them  
 202 too computationally expensive to cover the very long time scales associated with duc-  
 203 tile deformations and hence reproduce multiple deformation cycles.

204 Finally, other models have been developed to help understanding the dynamics of  
 205 fluids and its role in the deformation of faults (e.g. Segall & Rice, 1995, and many oth-  
 206 ers). In particular, recent idealized models of pressure diffusion in the host rock with rapidly  
 207 varying permeability have been able to explain the observed rapid tremor migrations and  
 208 their reversals (Cruz-Atienza et al., 2018; Farge et al., 2021). However, a very impor-  
 209 tant challenge remains to day: to couple these models with the two- or three-dimensional  
 210 deformation of the solid matrix and other near-fault processes to allow assessing their  
 211 impact on the geodetically observed strains.

## 212 1.2 Focus on the Slow Earthquake Phenomenon

213 Developing a single numerical modeling framework suitable for all of the above men-  
 214 tioned physical processes and that can cover the entire spectrum of associated time scales  
 215 is a very ambitious, perhaps unachievable, goal. Therefore, in this paper, we focus on  
 216 modelling the mechanical behaviour and deformation of fault zones, leaving aside for the  
 217 moment the role of fluids. We also concentrate over time scales intermediate between  
 218 those characterizing the cycle of major, or "classical", earthquakes (from decades to thou-

sands of years) and the one of dynamic rupture (faster than hundreds of seconds). Within this range, the deformation of faults is often controlled by slow earthquakes.

The slowest temporal scale associated with the slow earthquake phenomenon is revealed by geodetic observations of the accompanied slow and diffuse surface deformation, with typical event durations between weeks and months and inter-events gaps of the order of a few years (e.g., Dragert et al., 2001; Kostoglodov et al., 2003; Radiguet et al., 2012). The fastest temporal scale is related to seismic radiations, observed at frequencies above 1 Hz in the form of tectonic tremors (e.g., Obara, 2002; Payero et al., 2008) or low-frequency earthquakes (LFEs) (e.g., Shelly et al., 2006; Bostock et al., 2012; Frank et al., 2014) and which imply localized, brittle deformations and associated elastic strain variations in the source region on the order of fractions of a second. Therefore, even if ignoring the second-order effect of the long-term deformation of the system attributable to mantle relaxation, convection and delayed elastic deformations, as done in this paper, building a model for slow earthquakes entails dealing with localized, brittle deformations and diffuse, ductile deformations that are separated by about 8 orders of magnitudes of time scales. This huge separation requires developing a numerical scheme that allows simulating the relevant processes in reasonable simulation times.

This is the aim of the current work : developing a physically sound and numerically efficient continuum rheological framework for slow earthquakes. It is important to note however that doing so, we also keep in mind a future application to a wider range of time scales relevant to the entire seismic cycle. Another objective is that this framework be simple and versatile, so that to give valuable insights and eventually be transferable in the context of other geophysical systems that are characterized by a similar dynamics, that is, a dynamics comprised of mixed brittle/ductile and transient deformations, such as landslides and volcanic edifices (e.g., Peng & Gomberg, 2010; Lacroix et al., 2014; Carrier et al., 2015; Got et al., 2017; Handwerger et al., 2016; Poli, 2017; Parisio et al., 2019; Seydoux et al., 2020, and many others). A very important feature of the proposed modelling approach is that it accounts for rock fracturing processes via a progressive damage mechanism that is coupled to the mechanical strength of the material, which is described not only by an elastic moduli but also an apparent viscosity. As such, in addition to the long-term evolving strain of the system (observed with GPS, tiltmeters, strainmeters) the model represents the short-term temporal evolution of the averaged energy of seismic radiations (observed as tremors and LFEs).

The rheological model is presented in section 2, together with its numerical scheme. Its implementation in an idealized shearing experiment that is relevant in the context of subduction zones is described in section 3. The main characteristic numbers and times describing this experiment are described in section 4. Section 5 presents a demonstration of its mechanical and numerical behaviour, with a sensitivity analysis on the value of its main parameters. This analysis demonstrates its capability to simulate the wide separation of scales between the brittle and ductile processes and transient deformations at the intermediate time scales.

## 2 The Physical Model

The model builds on the Burgers framework, which combines the Maxwell (an elastic and a viscous component in series) and the Kelvin-Voigt (an elastic and a viscous component in parallel) visco-elastic models (see figure 1). As mentioned in section 1.2, for the sake of the current paper we neglect the effect of the delayed elasticity of the mantle, which is responsible for instance for the reversal of surface velocities following major earthquakes but is probably of second-order in the context of slow earthquakes. In the following description, the model is therefore reduced to the Maxwell component. In particular, we focus on testing the capability of this component to reproduce transient

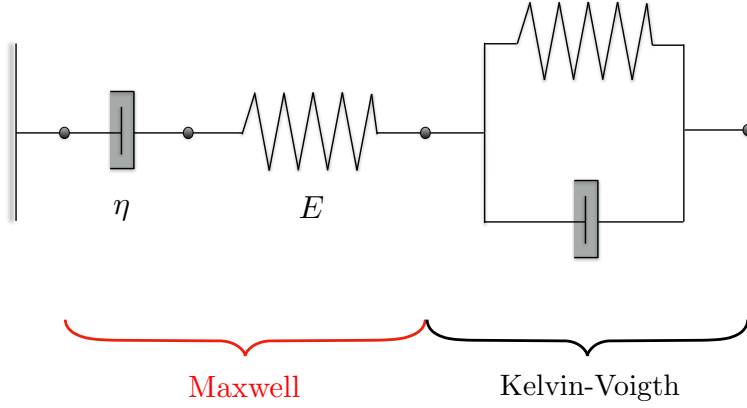


**Figure 1.** Schematic representation of the Burgers model. When loaded with a constant deformation, the Maxwell component undergoes a relaxation (exponential decay) of the stress. When unloaded, the part of the deformation associated to the viscous element is non-recoverable. When loaded with a constant stress, the Kelvin component leads to an exponential decay of the deformation. When unloaded, this deformation is fully recoverable. The implementation of the model described in this paper neglects the Kelvin component.

269 deformations and a deformation cycle akin slow earthquakes when  $E$  and  $\eta$  are not constant  
 270 but allowed to evolve in both space and time, according to the local degree of fracturing  
 271 of the material at the sub-grid scale, the so-called *level of damage*. The development  
 272 of the current visco-elastic framework therefore lies crucially on the formulation  
 273 of a coupling between  $E$  and  $\eta$  and this level of damage. The starting point of this coupling  
 274 follows the simple formulation suggested by (Dansereau et al., 2016a), which was  
 275 shown to successfully reproduce the spatial localization and intermittency of the damage  
 276 and deformation and associated scaling laws in another quasi-brittle material that  
 277 undergoes permanent deformations partially dissipating stresses when fractured; sea ice.

278 Another particularity of our approach is that, contrary to existing visco-elastic layered  
 279 models (e.g., K. Wang et al., 2012; Sun & Wang, 2015), here a unique rheology is  
 280 applied to the entire system (see figure 2). Its component are differentiated solely on the  
 281 basis of the bulk elastic modulus and on the local level of damage.

## 282 2.1 Constitutive Equation

283 The Maxwell model is applied here in the context of an elastic, compressible solid.  
 284 Its constitutive law reads

$$285 \frac{D\sigma}{Dt} + \frac{1}{\lambda}\sigma = E\mathbf{K} : \dot{\epsilon}, \quad (1)$$

286 where  $\mathbf{K}$  is the elastic stiffness tensor, defined in terms of Poisson's ratio,  $0 \leq \nu < 0.5$ ,  
 287 and from which the elastic modulus,  $E$ , is factored out. For any three-dimensional symmetric  
 288 tensor  $\epsilon = \epsilon_{ij} \in i, j; 1 \leq i, j \leq 3$ ,  $(\mathbf{K} : \epsilon)_{ij} = \frac{\nu}{(1+\nu)(1-2\nu)} \text{tr}(\epsilon)\delta_{ij} + 2\frac{1}{2(1+\nu)}\epsilon_{ij}$ .  
 289 The strain rate tensor,  $\dot{\epsilon}$  is taken equivalent to the rate of strain tensor and is given by  
 290  $D(\mathbf{u}) = \frac{\nabla\mathbf{u} + \nabla\mathbf{u}^T}{2}$  where  $\mathbf{u}$  is the velocity. The ratio of the material's apparent viscosity  
 291 and elastic modulus,  $\lambda = \eta/E$ , hereinafter referred to as the relaxation time, sets  
 292 the mesoscopic rate of dissipation of the stresses through permanent deformations.

293 Following Kachanov (1958) and previous isotropic damage models (e.g., Tang, 1997;  
 294 Lyakhovsky, Ben-Zion, & Agnon, 1997; Amitrano et al., 1999) the density of cracks at  
 295 the sub-grid scale is described by a mesoscopic scalar damage variable,  $d$ , the value of  
 296 which evolves between 0 for an undamaged and 1 for a totally damaged material (see

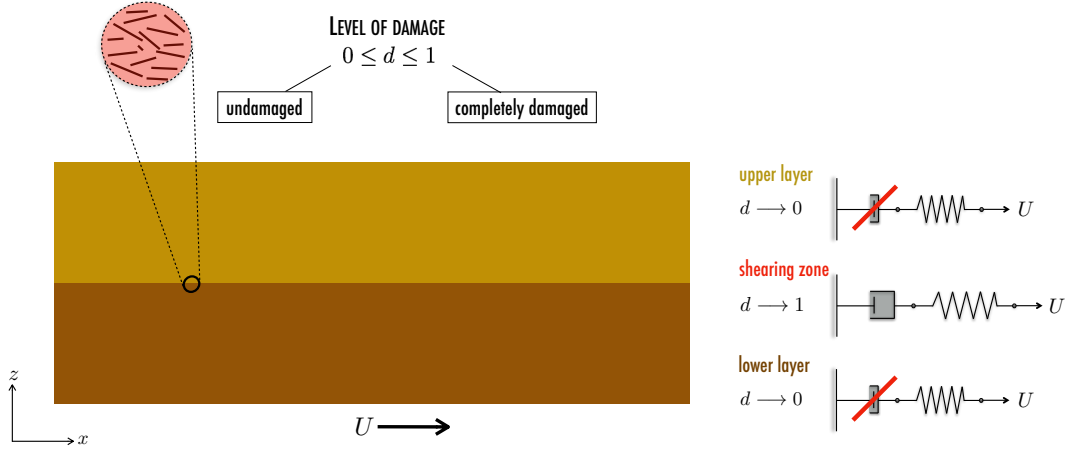


**Figure 2.** Schematic representation of the model and simulations, which represent a vertical ( $x, z$ ) cross-section of two layers of host rock sheared by applying a constant velocity at the bottom of the lower layer, in the  $x$ -direction. A unique visco-elasto-brittle constitutive law is applied to the entire system. The two layers are differentiated only on the basis of the undamaged value of their elastic modulus. The expected mechanical behaviour is one in which the bulk of both layers is quasi-elastic, since damage there is expected to be almost zero and the effective viscosity is high, and visco-elastic at the interface of the two layers, where the deformation and damage are localized and potentially high and the elastic modulus and apparent viscosity much reduced.

297 figure 2). In the case of the elastic modulus, the coupling to  $d$  is based on the principle  
 298 of effective stress (Kachanov, 1958) and reads

299 
$$E = E_0(1 - d), \quad (2)$$

300 where  $E_0$  is the undamaged elastic modulus of the material. In the case of the effective  
 301 viscosity,  $\eta$ , the coupling reads:

302 
$$\eta = \eta_0(1 - d)^\alpha, \quad (3)$$

303 where  $\eta_0$  is the bulk viscosity of the material, i.e., its viscosity in its undamaged state,  
 304 and  $\alpha$  is an exponent  $> 1$  such that the relaxation time,  $\lambda$ , setting the rate of dissipa-  
 305 tion of the stresses, decreases with the degree of fracturing of the material. This ad-hoc  
 306 but simple coupling allows, on the one hand, the dissipation of the stress through per-  
 307 manent deformations where the material is damaged and, on the other hand, the conserva-  
 308 tion of the stress associated to elastic deformations where the material is relatively  
 309 undamaged (Dansereau et al., 2016a; Weiss & Dansereau, 2017).

310 **2.2 Progressive Damage Mechanism**

311 The level of damage in the model evolves due to both fracturing and healing pro-  
 312 cesses. The first of these processes translates into an increase in  $d$  and its occurrence is  
 313 determined at any given model iteration by comparing the local state of stress to a criti-  
 314 cal stress value, set by a chosen damage criterion. The present implementation uses the  
 315 Mohr–Coulomb criterion

316 
$$\sigma_1 = q\sigma_2 + \sigma_c, \quad (4)$$

317 where  $\sigma_1$  and  $\sigma_2$  are the principal stresses,  $q = [(\mu^2 + 1)^{1/2} + \mu]^2$ ,  $\mu$  is the internal fric-  
 318 tion coefficient and  $\sigma_c = \frac{2C}{[(\mu^2 + 1)^{1/2} - \mu]}$ , where  $C$  is a non-zero cohesion (resistance of  
 319 the material to pure shear). No truncation is applied here to this criterion in the case

320 of  $\sigma_1, \sigma_2 < 0$  : hence it includes tensile stresses. In a manner similar to other damage  
 321 modelling frameworks, some noise is introduced in this criterion, by drawing the value  
 322 of  $C$  over each element of the discretized domain from a uniform distribution, to repre-  
 323 sent the heterogeneity of natural materials and insure progressive failure even under per-  
 324 fectly homogeneous forcing conditions.

325 As in the elasto-brittle model of (Amitrano et al., 1999),  $d$  evolves due to damag-  
 326 ing following

$$327 \quad 1 - d' = \delta d(1 - d), \quad (5)$$

328 where  $d'$  is the post-damaging value of damage,  $d$ , the pre-damaging value and  $\delta d$ , a con-  
 329 stant multiplication factor such that  $\delta d = 0$  when and where the state of stress is sub-  
 330 critical and  $0 < \delta d \leq 1$  when and where it is over-critical with respect to the damage  
 331 criterion. According to equations (2) and (3), each damage event implies that the local  
 332 elastic modulus and apparent viscosity decrease respectively as

$$333 \quad E' = \delta d E \quad (6)$$

$$334 \quad \eta' = \delta d^\alpha \eta \quad (7)$$

335 where the superscript  $'$  is hereinafter used to denote the post-damage strength, stress  
 336 and deformation. This local decrease in mechanical strength leads to an elastic redis-  
 337 tribution of the stresses from the over- to the sub-critical areas of the material, which  
 338 allows for the triggering of avalanches of damaging events, representing the propagation  
 339 of cracks at the mesoscale, as long as the elastic modulus (or relaxation time) or the ma-  
 340 terial remains significant. It is important to note that, as other damage frameworks, the  
 341 current model is not *dynamic* and as such, is not meant to capture the propagation of  
 342 the rupture that generates seismic waves. Instead, it aims at representing the effect of  
 343 such rupture processes on the deformation of the material.

344 In developing the model, we take advantage of the very large separation of scales  
 345 between the brittle and ductile deformations in faults to make the assumption that the  
 346 first type of deformation is quasi-instantaneous relative to the second type. As such, we  
 347 treat the evolution of the level of damage as independent of time. The same approxima-  
 348 tion is implicitly made in the time-independent (linear) elasto-brittle brittle model of (e.g.,  
 349 Amitrano et al., 1999). Here, we therefore follow a similar approach and formulate a steady-  
 350 state, iterative scheme for the stress redistribution associated with micro-fracturing and  
 351 fracture coalescence at the sub-grid scale. This formulation relies on two hypotheses:

- 352 1. the *immediate* effect of damage is to redistribute the local stresses, not strains.  
 353 In the following, this immediate post-damage state is referred to using the "\*" su-  
 354 perscript,
- 355 2. as the propagation of damage is quasi-instantaneous compared to viscous relax-  
 356 ation processes in the material considered, the viscous stress dissipation term in  
 357 equation (1) can be neglected when solving for the damage propagation. The con-  
 358 stitutive equation therefore reduces to that of a linear-elastic material:

$$359 \quad \sigma = E\mathbf{K} : \varepsilon,$$

360 where  $\varepsilon$  is the deformation (as opposed to the deformation rate) tensor.

361 The following constitutive equations thereby define respectively the pre- and immedi-  
 362 ate post-damage states:

$$363 \quad \sigma = E\mathbf{K} : \varepsilon,$$

$$364 \quad \sigma^* = E^*\mathbf{K} : \varepsilon^*,$$

365 Using the first hypothesis laid above, the following equality relating the pre-damage and  
 366 the immediate post-damage elastic modulus (respectively  $E$  and  $E^*$ ) and stresses ( $\sigma$  and

367  $\sigma^*$ ) can be written

$$368 \quad \frac{\sigma^*}{E^*} = \frac{\sigma}{E}.$$

369 Using equation (6), the immediate post-damage stress adjustment is therefore given by

$$370 \quad \sigma^* = \sigma \delta d.$$

371 Considering further that this local stress adjustment induced by the damage event will  
 372 lead, in a second time, to an adjustment in the neighbouring deformation and so, stress,  
 373 the new state of equilibrium between the post-damage stress,  $\sigma'$ , and the post-damage  
 374 deformation,  $\varepsilon'$ , is given by

$$375 \quad \sigma' - \sigma \delta d = E_0(1 - d')\mathbf{K} : \varepsilon'. \quad (8)$$

### 376 **2.3 Healing Mechanism**

377 Healing is another essential ingredient for the reproduction of the deformation of  
 378 fault zones (e.g., Bos & Spiers, 2002; Renard et al., 2000, and many others). In the case  
 379 of damaged rocks and rock gouges, it can include various processes, like sintering (e.g.,  
 380 Hirono et al., 2020), cementing and sealing from dissolution-precipitation processes (e.g.,  
 381 Sibson, 1992; R. T. Williams, Mozley, et al., 2019), motion/diffusion of asperities and  
 382 dislocations (e.g., Dieterich, 1979a, 1979b, and many others) and compaction (e.g., Hun-  
 383 feld et al., 2020). In the current model, the respective effects of all of these processes are  
 384 not differentiated but rather encapsulated into a single healing law that prescribes a de-  
 385 crease in the level of damage at a constant rate such that:

$$386 \quad \frac{Dd}{Dt} = -\frac{1}{t_h}d, \quad 0 \leq d < 1, \quad (9)$$

387 where  $t_h$  the healing time. Through their respective coupling to  $d$ , both the elastic mod-  
 388 ulus and apparent viscosity are therefore allowed to re-increase towards their bulk value  
 389 after damage events : a behaviour that is consistent with observations of the evolution  
 390 of seismic velocities (Li & Vidale, 2001; Brenguier et al., 2008). This very simple law,  
 391 used here for the purpose of demonstrating the general impact of healing on the mod-  
 392 elled mechanical behaviour, could be refined in more realistic implementations of the model  
 393 (see section 11).

### 394 **2.4 The Coupled Visco-Elasto-Brittle Model**

395 The proposed model couples the time-independent treatment of the damage prop-  
 396 agation with the time-dependant, visco-elastic Maxwell constitutive equation and the  
 397 time-dependant evolution equation for healing. To do so, the complete system of equa-  
 398 tions is solved in three steps or subproblems ( $P$ ):

- 399 ( $P1$ ) The full constitutive equation (1) is first solved together with the full momentum  
 400 equation, boundary and forcing conditions (see section 3) and using the field of  
 401 damage at the previous time step for a first estimate of the field of velocity and  
 402 stress at the current time step. The field of stress is then compared to the local  
 403 damage criterion.
- 404 ( $P2$ ) *If and only if* the stress locally exceeds the damage criterion, the forcing is paused  
 405 and the macroscopic deformation of the simulated material is held constant. The  
 406 model enters a steady-state subiteration in which (i) the level of damage,  $d$ , is ad-  
 407 justed to its post-damage value,  $d'$ , (ii) equation (8) is solved for the adjusted state  
 408 of stress,  $\sigma'$ . These two steps are carried iteratively until all states of stresses be-  
 409 come sub-critical, at which point the stress state at the current time is set to the  
 410 adjusted stress at the final subiteration.

411 (P3) The healing equation (9) is solved for the field of damage at the current time step,  
 412 using the post-damaging level of damage,  $d'$ .

413 This scheme is illustrated schematically in figure 3 and presented in full details in Ap-  
 414 pendix B.

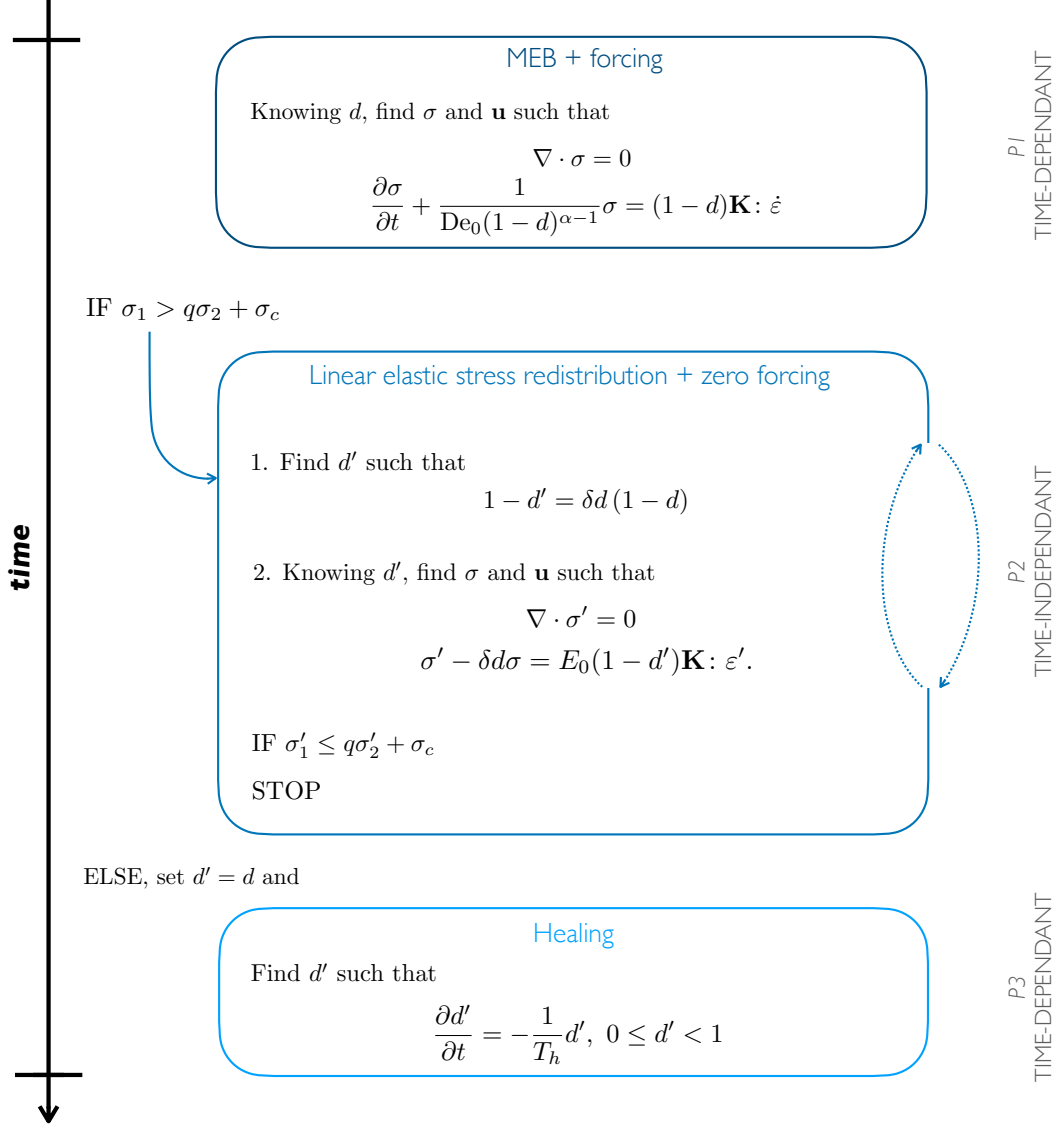


**Figure 3.** Schematic representation of the numerical scheme, composed of the three sub-problems, and its resolution over one model time step. For simplicity, the superscript ' $\sim$ ' for adimensional variables is dropped. The full numerical scheme and time discretization is described in Appendix B.

### 415 3 Implementation

416 The model is implemented here in a 2-dimensional shearing experiment (see fig-  
 417 ure 4), meant as a very idealized representation of a vertical cut ( $x, z$ ) through a sub-  
 418 duction zone. Two layers of host rock are sheared by applying a constant  $x$ - velocity

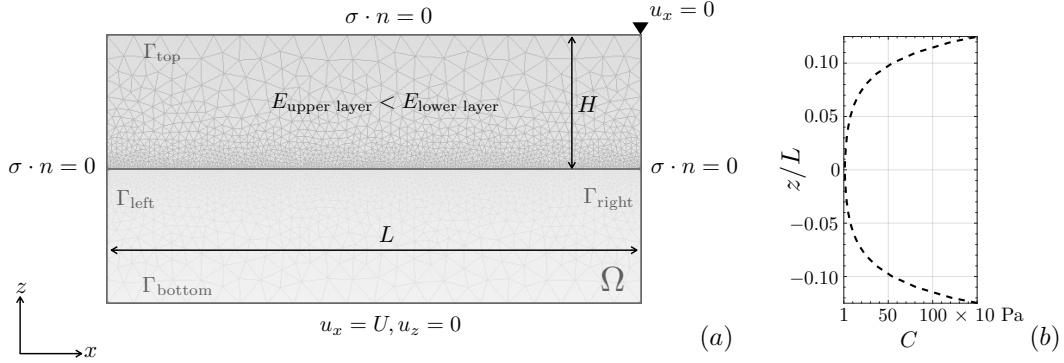


**Figure 4.** (a) Simulation setup. The domain, boundaries and boundary conditions are detailed in Appendix B. (b) Functional dependence of the cohesion,  $C$ , (i.e., of the damage criteria) on  $z$ , prescribed to avoid concentrating most of the deformation at the top and bottom boundaries, where the  $x$ -velocity is either locally or entirely prescribed.

419 at the bottom of the lower layer. No confinement is applied on the lateral sides and the  
 420 surface is free, except for the top, right corner of the domain (the furthest surface point  
 421 downstream and in the direction of the forcing), for which  $u_x = 0$ . The horizontal ext-  
 422 tent of the system perpendicular to the shearing direction is considered much greater than  
 423 the horizontal extent in the shearing direction. Plane strains are therefore assumed. No  
 424 discontinuity is introduced over the domain other than in the value of the undamaged  
 425 elastic modulus,  $E_0$ , which is lower by a factor of 3 in the upper layer, representing the  
 426 continental crust, than in the lower layer, representing the oceanic crust (see table 1).  
 427 Also, in order to avoid that all of the deformation be trivially accommodated near the  
 428 bottom boundary of the domain, where a non-zero  $x$ -velocity is prescribed, or near the  
 429 top, right corner of the domain, where the  $x$ -velocity is fixed to 0, a functional depen-  
 430 dence of  $C$  on  $z$  is prescribed, of the form  $C = C_0 \times \exp(|5.0 * z/H|)$ , where  $H$  is the  
 431 thickness of both layers (see figure 4b) and  $C_0$  is the minimum cohesion. This function  
 432 allows the magnitude of  $C$  to vary little over a wide enough range of values of  $z$  centred  
 433 on  $z = 0$  (e.g.,  $C(z = 0.01) = 1.5 \times C(z = 0)$ ) and therefore does not affect the degree  
 434 of localization of the deformation in the shearing zone that forms between the two simu-  
 435 lated layers. Over each grid cell element, this function is locally multiplied by a value  
 436 that is picked randomly over a uniform distribution of values over the range  $[0.75 \ 1]$ , thereby  
 437 introducing some noise in the local damage criteria that represents the natural hetero-  
 438 geneity of the material (see section 2.2).

439 The balance of forces in the experiment neglects inertia and advection. In order  
 440 to avoid introducing artifacts in the solution related to our finite-size domain and bound-  
 441 ary conditions, we also neglect gravity. The momentum equation therefore reads:

$$442 \quad \nabla \cdot \sigma = 0. \quad (10)$$

443 As slow earthquakes entail deformations (i.e., slip) that are relatively small relative to  
 444 the horizontal and vertical extent of subduction zones, the advection, rotation and de-  
 445 formation terms which are included in material derivatives in the constitutive equation  
 446 (1) and healing equation (9), are all neglected, such that  $\frac{D\sigma}{Dt} = \frac{\partial\sigma}{\partial t}$  and  $\frac{Dd}{Dt} = \frac{\partial d}{\partial t}$ . In  
 447 all simulations performed here, the total, cumulative deformation of the system remains  
 448 below 10% of the the size of the smallest mesh element, ensuring that this approxima-  
 449 tion is indeed valid. The effect of the elastic deformations on the material's density are  
 450 neglected as well, such that mass conservation does not need to be imposed.

Model/setup parameters		Value
Length of the domain	$L$	$10^6, 10^4, 10^2$ m
Thickness of both layers	$H$	$\frac{1}{8}L$
Tectonic forcing velocity	$U$	$10^{-9}$ m s $^{-1}$
Undamaged relaxation time	$\lambda_0 = \frac{\eta_0}{E_0}$	$10^{12}$ s
Poisson's ratio	$\nu$	0.3
Internal friction coefficient	$\mu$	0.7
Maximal cohesion	$C_0$	$10^4$ Pa

**Table 1.** Model and simulation parameter values.

451 The model equations are discretized in time using a backward Euler scheme of order  
452 1 (see section B01 of the Appendix for the details) and discretized in space using fi-  
453 nite elements. In the following,  $\Delta t$  designate the model time step and  $\Delta x$ , the spatial  
454 resolution of the mesh grid. The triangular elements grid used is built using the Gmsh  
455 generator (Geuzaine & Remacle, 2009). As the model is isotropic by construction, and  
456 in order to avoid preferential orientations in the localization of the deformation, it is cho-  
457 sen unstructured. The spatial resolution,  $\Delta x$ , is set to be 1/20 of the horizontal extent,  
458  $L$ , of the domain at the top and bottom boundaries. It is refined by a factor of 10, so  
459 that to be 1/200 of  $L$ , at the junction of the two layers (see Figure 4) where deforma-  
460 tion is expected to be maximal. As cumulative deformations are small in all simulations,  
461 the deformation of the mesh is not calculated and the position of grid nodes, not updated  
462 in time. The resolution of the variational formulation of the equations make use of the  
463 C++ library RHEOLEF (Saramito, 2020). The polynomial approximations for  $\mathbf{u}$  are of  
464 order 1 and continuous at inter-element boundaries. As the stress tensor is a function  
465 of the velocity gradient and the damage, a function of the stress tensor, the approxima-  
466 tions for  $\sigma$ ,  $\sigma'$ ,  $d$  and  $d'$  are of degree 0 and discontinuous at inter-element boundaries.

#### 467 4 Adimensional System of Equations and Adimensional Parameters

468 In all of the simulations performed here, the system of equations is solved and re-  
469 sults are expressed in adimensional form. This allows describing and exploring the sen-  
470 sitivity of the rheological framework in terms of a reduced set of parameters and using  
471 the same idealized setup to represent systems with different physical dimensions and/or  
472 deformation time scales.

473 The model is made adimensional with respect to the horizontal extent,  $L$ , of the  
474 domain, the constant velocity prescribed at the bottom of the lower layer,  $U$ , and the  
475 average of the undamaged elastic modulus of the two layers,  $E_0$ . The time,  $T$ , charac-  
476 terizing the deformation process is therefore given by  $\frac{L}{U}$ . The superscript ‘~’ is used for  
477 all dimension-less variables and operators, which are listed in table A1. For a full descrip-  
478 tion of the adimensional formulation of the variables and equations, the reader can re-  
479 fer to Appendix A.

480 The complete adimensional system of equations reads

481 
$$\tilde{\nabla} \cdot \tilde{\sigma} = 0 \quad (11)$$

482 
$$\frac{\partial \tilde{\sigma}}{\partial \tilde{t}} + \frac{1}{\text{De}_0(1-d)^{\alpha-1}} \tilde{\sigma} = (1-d)\mathbf{K} : \tilde{\varepsilon}, \quad (12)$$

483 
$$1-d' = \delta d(1-d) \quad (13)$$

484 
$$\tilde{\nabla} \cdot \tilde{\sigma}' = 0 \quad (14)$$

485 
$$\tilde{\sigma}' - \delta d \tilde{\sigma} = (1-d')\mathbf{K} : \tilde{\varepsilon}' \quad (15)$$

486 
$$\frac{\partial d'}{\partial \tilde{t}} = -\frac{1}{T_h} d', \quad 0 \leq d' < 1, \quad (16)$$

487 with the damage criterion

488 
$$\tilde{\sigma}_1 = [(\mu^2 + 1)^{1/2} + \mu]^2 \tilde{\sigma}_2 + \frac{2C/E_0}{[(\mu^2 + 1)^{1/2} - \mu]}. \quad (17)$$

489 The value of Poisson's ratio,  $\nu$ , and of the internal friction coefficient,  $\mu$ , are fixed in the  
 490 following simulations to values common for geomaterials (Byerlee, 1978; Jaeger & Cook,  
 491 1979). The brittleness of the material, given by the ratio of the cohesion to the undam-  
 492 aged elastic modulus,  $C_0/E_0$ , is also kept constant. Besides these parameters, the four  
 493 adimensional parameters that characterize the model are:

- 494 1.  $\text{De}_0 = \frac{\eta_0}{E_0} \frac{U}{L}$ , the (undamaged) Deborah number,  
 495 2.  $\alpha$ , the damage parameter, setting the rate at which the viscosity (or relaxation  
 496 time) decreases with the level of damage,  
 497 3.  $\delta d$ , the damage increment,  
 498 4.  $T_h = \frac{t_h}{T}$ , the time for healing,

499 The limits and range of values over which these parameters are varied in the sensitiv-  
 500 ity experiments performed here are summarized in Table 2 and discussed in the follow-  
 501 ing sub-sections.

Adimensional parameter		Range of values
Characteristic healing time	$T_h$	$10^{-1} - 10^{-7}$
Undamaged Deborah number	$\text{De}_0$	0.01, 0.1, 10
Damage increment	$\delta d$	0.1, 0.3, 0.5, 0.7, 0.9
Damage parameter	$\alpha$	2, 3, 4, 6, 8

**Table 2.** Adimensional model parameters and the range of values over which they are varied in the model sensitivity experiments.

502 **4.1 The Deborah Number, De**

503 The Deborah number can be defined as the dimensionless ratio of the viscous re-  
 504 laxation time for the stress,  $\lambda$ , and of the time for the deformation process,  $T = \frac{L}{\dot{\gamma}}$ , (i.e.,  
 505 the inverse of the macroscopic shearing rate). It characterizes the fluid-like versus elas-  
 506 tic solid-like behaviour in unsteady flows, and as such is a relevant quantity to charac-  
 507 terize the deformation of faults and the slow earthquake phenomenon. Materials char-  
 508 acterized by a low Deborah number, either because they dissipate stresses rapidly or be-  
 509 cause they are deformed very slowly, have a behaviour that approaches that of a (New-

510 tonian) fluid and therefore flow steadily. Materials characterized by a high Deborah num-  
 511 ber, either because they dissipate stresses very slowly or because they are deformed rapidly,  
 512 behave like elastic solids and flow unsteadily.

513 Compared to classical earthquakes, slow earthquakes appear to be a less intermit-  
 514 tent, or equivalently a more steady, and therefore a more predictable form of deforma-  
 515 tion. Indeed, in some subduction zones like Cascadia (Dragert et al., 2001) and Guer-  
 516 rero, Mexico (Cotte et al., 2009; Radiguet et al., 2012) major slow earthquake episodes  
 517 show approximately stable recurrence times. However, the recurrence interval of slow  
 518 slip events varies greatly from one subduction zone to another. For instance, it is of a  
 519 few months in some segments of the Nankai subduction in Japan (e.g., Poiata et al., 2021),  
 520 on the order of one year in Cascadia, and of nearly four years in Guerrero. Recurrence  
 521 interval are also known to differ for different segments of the same subduction zone (e.g.,  
 522 Brudzinski & Allen, 2007) and are observed to decrease with depth (e.g., Wech & Crea-  
 523 ger, 2011; Frank, Radiguet, et al., 2015).

524 To take into account this variability in our simulations, as well as the variability  
 525 and uncertainty related to the mechanical properties of the crust (elastic modulus and  
 526 viscosity), we explore three values of the *undamaged* Deborah number (0.001, 0.1 and  
 527 0.1, see table 3) each separated by two orders of magnitude. Practically, in the simula-  
 528 tions, these different values are obtained by varying the time associated with the defor-  
 529 mation process,  $T = \frac{L}{\dot{\epsilon}}$ , and maintaining the undamaged relaxation time,  $\lambda_0 = \frac{\eta_0}{E_0}$ ,  
 530 constant ( $\lambda_0 = 10^{12}$  s). This relaxation time is consistent with an undamaged elastic  
 531 modulus,  $E_0$ , on the order of  $10^{11}$  Pa (in agreement with e.g., Dziewonski & Anderson,  
 532 1981) and a bulk, undamaged viscosity,  $\eta_0$ , of  $10^{23}$  Pa s (Siravo et al., 2019) for both the  
 533 continental and oceanic crust. The deformation process time,  $T$ , is set by considering  
 534 a typical tectonic velocity of  $10^{-9}$  m/s (on the order of a few cm/year) and considering  
 535 different horizontal extent,  $L$ , over which the fault is activated and slip occurs. The low-  
 536 est value of  $De_0$  explored considers  $L = 10^6$  m (1000 km), representative of a large sub-  
 537 duction zone. Following the definition of the Deborah number, this lower bound can be  
 538 interpreted alternatively as representing a smaller but deeper, hence lower viscosity seg-  
 539 ment of a fault. The highest value is representative of a small activated segment (1000  
 540 m) or alternatively, as a larger but shallower and hence more brittle part of a fault.

541 It is very important to note, however, that while  $De_0$  sets the bulk fluid-like ver-  
 542 sus elastic solid-like behaviour of the system and therefore is a relevant quantity to char-  
 543 acterize the macroscopic deformation cycle, for instance in terms of its duration, in the  
 544 visco-elasto-brittle model presented here, the *effective* Deborah number,  $De$ , is not ho-  
 545 mogeneous throughout the system but varies in space and time. Indeed, according to equa-  
 546 tions (2) and (3),  $De$  evolves locally as a function of the level of damage, as  $De = De_0 d^{\alpha-1}$ .  
 547 In all three systems, this decrease will leads to a more fluid-like behaviour where and when  
 548 the host rock becomes damaged.

## 549 4.2 The Healing Time, $T_h$

550 In the present model, the healing time represents the time it takes for a completely  
 551 damaged element ( $d = 1$ ) to evolve back to its undamaged state ( $d = 0$ ) and recover  
 552 entirely its mechanical strength. Since several different healing processes are thought to  
 553 be at play in faults (see section 2.3) and the rates at which these different processes very  
 554 likely depend on various local factors, like pressure, temperature, the availability of flu-  
 555 ids and the type of rock (see for instance McLaskey et al., 2012), estimating  $T_h$  is highly  
 556 non-trivial. Therefore, we define our estimation here based on lower and upper bounds  
 557 values. On the one hand, observations of post-seismic velocity changes, which estimates  
 558 the time required for the velocity of  $P$  and  $S$  waves (or, by extension, the elastic mod-  
 559 ulus of the crust in the vicinity of the fault) to re-increase to their pre-seismic value, place  
 560 the lower bound to a few (2-5) years (e.g., Li et al., 1998; Brenguier et al., 2008). Indeed,

561 while cracks that open during the mainshock probably close partially with time, one still  
 562 expects the vicinity of the shearing zone to remain highly damaged relative to the sur-  
 563 rounding host rock and that, at all times. On the other hand, assuming that the fault  
 564 heals completely between large earthquakes, the upper bound can be estimated from pseudo-  
 565 recurrence times, which reach a few thousand years in some faults (e.g., Li et al., 1998;  
 566 R. T. Williams, Davis, & Goodwin, 2019).

567 Four orders of magnitude of healing time are explored here, which vary between  
 568 these lower and upper bounds. In dimensional form, these values are:  $t_h = 10^8$  s, which  
 569 is equivalent to about  $\sim 3$  years,  $10^9$  s ( $\sim 30$  years),  $10^{10}$  s ( $\sim 300$  years) and  $10^{11}$  s  
 570 ( $\sim 3000$  years). Since different  $De_0$  numbers are explored by varying the process time  
 571  $T$ , and as time in our system of equations is made adimensional with respect to  $T$  (see  
 572 section 4), the different  $De_0$  lead to different adimensional values of the time of healing,  
 573  $T_h$ . The dimensional and corresponding adimensional values of  $t_h$  and  $T_h$  correspond-  
 574 ing to each  $De_0$  are listed in table 3.

### 575 4.3 The Damage Parameter, $\alpha$

576 As mentioned in section 2.2, the purpose of the rather "ad-hoc" damage param-  
 577 eter,  $\alpha$ , is that the model accounts for a more rapid dissipation of the stresses where the  
 578 material is highly damaged than where it is relatively undamaged. The only physical con-  
 579 straint on its value is therefore  $\alpha > 1$ . There is no theoretical upper bound for  $\alpha$ . How-  
 580 ever, for  $\alpha$  large, the relaxation time becomes very small at the onset of damage, what-  
 581 ever the damage level. Dansereau (2016b) and Weiss and Dansereau (2017) have demon-  
 582 strated that in this case, stresses are readily dissipated after each damage event and the  
 583 mechanical behaviour becomes essentially elasto-plastic. Here, the sensitivity of the model  
 584 is investigated for values of  $\alpha$  between 2 and 8, which proves to be a wide enough range  
 585 of values for the model to exhibit different mechanical behaviours relevant in the con-  
 586 text of faults and slow earthquakes.

### 587 4.4 The Damage Increment, $\delta d$

588 Similar to the damage parameter, the value of the damage increment is not con-  
 589 strained other than within the range of values intrinsic to its definition : between 0 and  
 590 1. It is however expected to be determinant on the mechanical response of the model.  
 591 For large values of  $\delta d$ , the decrease in  $E$  at each damage event, given by equations (6)  
 592 and (7) respectively, as well as the associated increase in the level of damage, given by  
 593 equation (5), are small. Conversely, for small values of  $\delta d$ , the decrease in  $E$  and  $\eta$  and  
 594 associated increase in  $d$  at each damage event is large. In the first limit, the dissipation  
 595 of the stress in permanent deformations is small. One can expect the emergence of a brit-  
 596 tle creep regime, in which the system remains always near criticality. In the second limit,  
 597 the dissipation of the stress into permanent deformations is large, which can impede elas-  
 598 tic interactions in the system and, by the same fact, the spatial and temporal localiza-  
 599 tion of the deformation (Dansereau, 2016b; Weiss & Dansereau, 2017). In the following,  
 600 the model behaviour is analyzed for damage increment values of 0.1, 0.3, 0.5, 0.7 and 0.9.

## 601 5 Results

### 602 5.1 Mechanical Model Response

603 Here we first describe the overall macroscopic behaviour of the model. This descrip-  
 604 tion is based on simulation results obtained for a specific set of model parameters ( $De_0 =$   
 605  $0.001$ ,  $T_h = 10^{-5}$ ,  $\tilde{\Delta}t = 10^{-10}$ ,  $\alpha = 4$ ,  $\delta d = 0.1$ ), but the conclusions broadly apply  
 606 to a wider range of values. Figure 5a shows the temporal evolution of the model response  
 607 in terms of the macroscopic shear stress, calculated by integrating the shear stress on  
 608 the entire top boundary of the domain, and of the *macroscopic damage increment*, de-

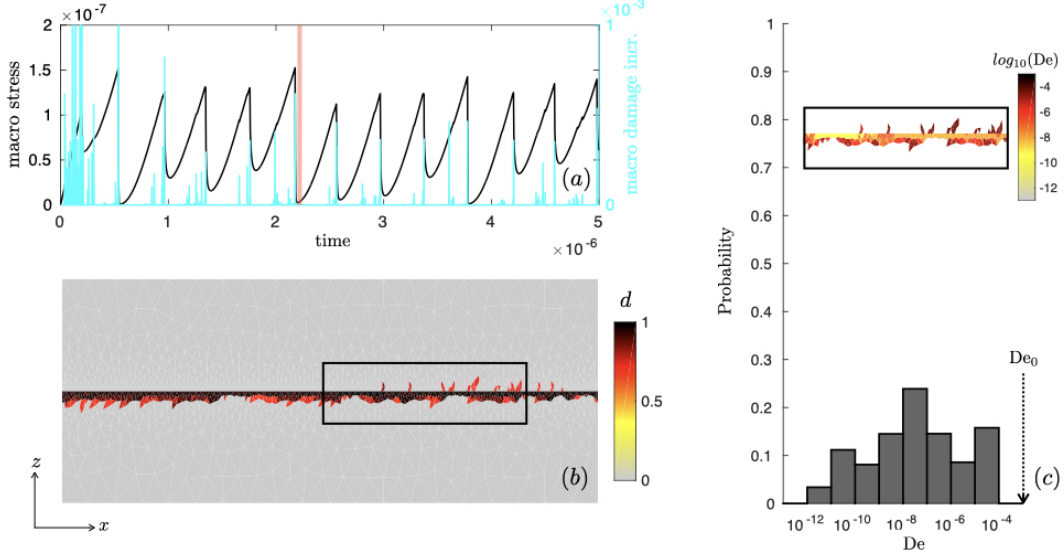


**Figure 5.** (a) Temporal evolution of the macroscopic shear stress (black line) and of the macroscopic damage increment (as defined by eq. 18, cyan line) for a simulation using  $De_0 = 0.001$ ,  $\tilde{\Delta}t = 10^{-10}$ ,  $\alpha = 4$ ,  $\delta d = 0.1$  and  $T_h = 10^{-5}$ . (b) Instantaneous field of the level of damage after the large avalanche of damage events and associated unloading phase indicated by the vertical red line on panel (a). (c) Zoom-in on the instantaneous field of  $De$  (in logarithmic scale) corresponding to the black box indicated on panel (b) and normalized distribution of the instantaneous values of  $De$  for all damaged elements of the domain corresponding to the unloading phase indicated by the vertical red line on panel (a).

609 fined as the local damage increment integrated over all elements  $I$  that are damaged during a stress redistribution subiteration  $k$  and over the  $K$  subiterations realized over the current model time step,  $n + 1$ :

$$612 \quad \sum_{k=1}^K \sum_{i=1}^I (1 - \delta d)(1 - d_i^{n,k}). \quad (18)$$

613 An animation of this simulation, showing the temporal evolution of the field of damage (in logarithmic scale) and of both the macroscopic shear stress and damage increment is available as Supporting Information to this paper (see S1). After the initial and almost linear-elastic loading phase, this response is characterized by asymmetric cycles comprised of an either partial or total stress drop (hereinafter called unloading phase) and a subsequent healing and stress increase phase (hereinafter called loading phase). Damage can occur at any moment of the cycle, but unloading phases are generally characterized by the largest avalanches of damaging events, which can span either a large part of or the entire domain (see S1). When the stress drop is partial, it is generally comprised of an initial brutal drop associated to a large damage avalanche, followed by a slower relaxation phase, not necessarily associated to significant further damage. This post-rupture, or "post-seismic", relaxation results from viscous-like permanent deformations along a fault made of highly damaged, hence low viscosity, material. Such behaviour is made possible by the rheology proposed above. The occurrence of pre-rupture (akin to foreshocks) or post-rupture (akin to aftershocks) damage events varies with the choice of model parameters (see section 11 below). However, for all simulations and parameter values covered here, the damaging activity localizes at the interface of the two layers (mostly within the lower plate, see figure 5b), a behaviour that is not prescribed but that arises naturally due to the forcing condition applied at the bottom of the lower layer and to the small

632 difference in elastic modulus assigned to each layer. Consequently, the deformation of  
 633 the system is also highly localized at this interface. Figure 5b also indicates that dam-  
 634 age is heterogeneously distributed along the interface. As a consequence of the prescribed  
 635 coupling between  $d$  and both the  $E$  and  $\eta$  (see eq. 2 and 3), this heterogeneity in dam-  
 636 age leads to a large heterogeneity in the value of the relaxation time, or equivalently of  
 637 the effective De number, along the interface. As indicated by the distribution shown in  
 638 Figure 5c, the values of De associated with damaged grid elements indeed span several  
 639 orders of magnitude. The lowest values of De are obtained at the end of unloading phases  
 640 and re-increase as the system heals towards the end of loading phases.

641 However, it is worth noting that, over the range of parameter values explored here,  
 642 the vicinity of the interface remains relatively highly damaged at all times (see S1) and  
 643 never completely heals: a behaviour that is expected in the context of active faults. By  
 644 the same fact, and because the simulations are initialized from a uniformly undamaged  
 645 state ( $d = 0$  everywhere), the behaviour during the first loading-unloading cycle is very  
 646 different from the subsequent ones : the damaging activity is relatively much higher be-  
 647 cause the damaged zone is created from scratch while over all subsequent cycles, the in-  
 648 terface is already damaged to a relatively large degree. In all further analyses of the model  
 649 behaviour, this first loading-unloading cycle is therefore discarded.

## 650 5.2 Convergence and Numerical Efficiency

651 Here we verify that the macroscopic behaviour of the model converges with increas-  
 652 ing temporal resolution. To do so, for the three identified values of  $De_0$  (see section 4.1),  
 653 simulations are run with five different values of the (adimensional) time step,  $\tilde{\Delta}t$ . All of  
 654 these simulations use the same value of the damage increment ( $\delta d = 0.1$ ) and of the  
 655 damage parameter ( $\alpha = 4$ ) and are initiated with the same field of noise on the cohe-  
 656 sion. We explored a range of values of the healing time for these simulations, and retained  
 657 the one value that produced the most physically sound results for each set of simulations  
 658 with a given  $De_0$  value (see section 5.3.1).

659 Figure 6 shows the temporal evolution of the model response in terms of the macro-  
 660 scopic stress (a) and of the macroscopic damage increment (b), defined as in eq. (18).  
 661 It indicates that the largest value of the time step explored here leads to a pathologi-  
 662 cal model response. This is expected, as this  $\tilde{\Delta}t$  value approaches the order of magni-  
 663 tude of the main period of the loading-unloading cycles : this temporal resolution there-  
 664 fore does not allow resolving the progressive propagation of the damage in the system,  
 665 nor the sharp stress drop associated with each macroscopic rupture. For smaller values  
 666 of the time step, the model response converges well in terms of the main frequency and  
 667 amplitude of the macroscopic stress variations when increasing the temporal resolution.  
 668 It is also the case for the macroscopic variations in the deformation of the system (not  
 669 shown) and in the damage increment.

670 To robustly test the convergence of the model response, we use a single metric that  
 671 combines these three different pieces of information : the local damage increments and  
 672 the resulting redistribution of the stress and of strains over the entire system. This is  
 673 the elastic energy released within the system due to the propagation of damage,  $E_{brit}$ ,  
 674 the temporal evolution of which is shown in figure 6c. The distribution of this energy  
 675 can be directly related to that of acoustic emissions associated to the micro-fracturing  
 676 of rocks (e.g., Amitrano, 2003) and can therefore serve as a proxy for the seismic signal  
 677 recorded at the geophysical scale. At each current ( $n+1$ ) model time step,  $E_{brit}$  is es-  
 678 timated as

$$679 E_{brit}^{(n+1)} = \sum_{i=1}^I \frac{A_i}{A_{tot}} \left( \sigma_i^{(n+1,0)} : \varepsilon_i^{(n+1,0)} - \sigma_i^{(n+1,K)} : \varepsilon_i^{(n+1,K)} \right), \quad (19)$$

680 where  $i$  designate each element,  $I$ , the total number of elements over the domain,  $A_i$  the  
 681 area of each element and  $A_{tot}$ , the area of the entire domain. The superscripts  $n + 1, 0$

682 and  $n + 1, K$  refer respectively to the stress and strain values before and at the end of  
 683 the avalanche of damaging events, which takes a total of  $K$  stress redistribution sub-  
 684 iterations. To compare simulations using different time steps,  $E_{brit}$  is normalized by  $\tilde{\Delta}t$ .  
 685 In agreement with the observed convergence in the variations of the macroscopic stress,  
 686 deformation and damage increment, figure 6d clearly shows that the shape of the prob-  
 687 ability density function (PDF) of the normalized  $E_{brit}$  stabilizes over the three small-  
 est values of time step explored here.

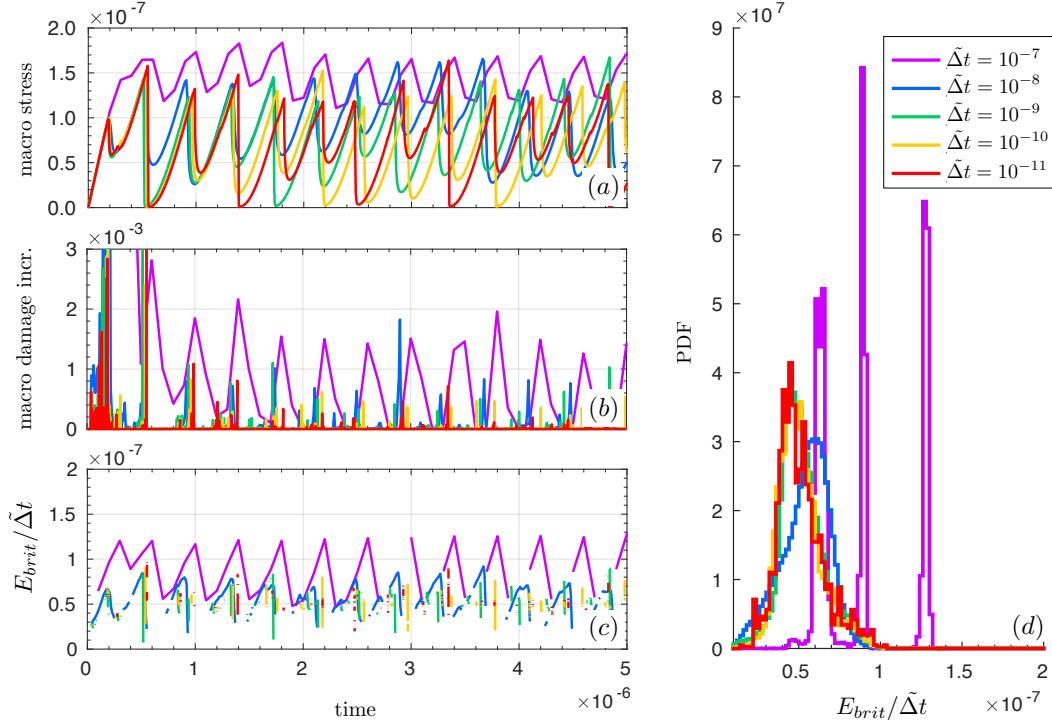


**Figure 6.** Temporal evolution of (a) the macroscopic stress, (b) the macroscopic damage increment and (c) the macroscopic elastic energy released due to the propagation of damage within the system, normalized by the time step  $\tilde{\Delta}t$ , for simulations using  $De_0 = 0.001$ ,  $\alpha = 4$ ,  $\delta d = 0.1$ ,  $T_h = 10^{-5}$  and  $\tilde{\Delta}t = 10^{-11}, 10^{-10}, 10^{-9}, 10^{-8}, 10^{-7}$  (corresponding to  $\Delta t = 10^4$  s,  $10^5$  s,  $10^6$  s,  $10^7$  s,  $10^8$  s) (d) Probability density function of  $E_{brit}/\tilde{\Delta}t$ .

688

689 Simulations ran with  $De_0 = 0.1$  and  $De_0 = 10$ , the same values of  $\delta d$  (0.1) and  
 690 of the damage parameter,  $\alpha$ , (4) and values of healing time of  $T_h = 10^{-4}$  and  $T_h =$   
 691  $10^{-3}$  respectively show that a similar convergence is retrieved in both cases over a range  
 692 of values of  $\tilde{\Delta}t$  (see figure C1 of Appendix C). These values are summarized in table 3:  
 693 the red ones indicating a non-converged model response. The comparison of these val-  
 694 ues across the three  $De_0$  explored here suggests that the time step should be chosen such  
 695 that  $\frac{\Delta t}{T} \lesssim 10^{-8}$  to ensure a fully converged and therefore physically meaningful model  
 696 behaviour. The time step values corresponding to each  $De_0$  value and retained for the  
 697 sensitivity analyses on the other model parameters are indicated in green in table 3.

698 We further compare the simulations presented in figure 6 in terms of CPU and real  
 699 simulation time. Each simulation was ran for a fixed (adimensional) total time of  $5.0 \cdot$   
 700  $10^{-6}$ , which represents, in dimensional equivalent, 160 years of evolution of the system.  
 701 With the specific choice of model parameters employed in this particular simulation, each  
 702 loading-unloading cycle covers about 12 years. The model response converges for time

$T$ (s)	$De_0$	$\Delta t$ (s)	$\tilde{\Delta}t$	$t_h$ (s)	$T_h$
$10^{15}$	0.001	$10^4$	$10^{-11}$	$10^8$	$10^{-7}$
		$10^5$	$10^{-10}$	$10^9$	$10^{-6}$
		$10^6$	$10^{-9}$	$10^{10}$	$10^{-5}$
		$10^7$	$10^{-8}$	$10^{11}$	$10^{-4}$
		$10^8$	$10^{-7}$		
$10^{13}$	0.1	$10^3$	$10^{-10}$	$10^8$	$10^{-5}$
		$10^4$	$10^{-9}$	$10^9$	$10^{-4}$
		$10^5$	$10^{-8}$	$10^{10}$	$10^{-3}$
		$10^6$	$10^{-7}$	$10^{11}$	$10^{-2}$
		$10^7$	$10^{-6}$		
$10^{11}$	10	$10^2$	$10^{-9}$	$10^8$	$10^{-3}$
		$10^3$	$10^{-8}$	$10^9$	$10^{-2}$
		$10^4$	$10^{-7}$	$10^{10}$	$10^{-1}$
		$10^5$	$10^{-6}$	$10^{11}$	$10^0$
		$10^6$	$10^{-5}$		

**Table 3.** Values of the deformation timescale,  $T$ , the model time step,  $\Delta t$ , and healing time,  $t_h$ , explored in the present sensitivity experiments, with their adimensional counterpart : respectively,  $De_0$ ,  $\tilde{\Delta}t$  and  $T_h$ . For each value of  $De_0$ , the values of  $\Delta t$  (or  $\tilde{\Delta}t$ ) for which the model response is not fully converged are indicated in red. The value of  $\Delta t$  (or  $\tilde{\Delta}t$ ) retained for the sensitivity analyses on  $T_h$ ,  $\delta d$  and  $\alpha$  is indicated in green. For each  $De_0$  value also, the optimal value of  $t_h$  (or  $T_h$ ) retained for the sensitivity analyses on  $\alpha$  and  $\delta d$  are indicated in green.

703 step values of  $\tilde{\Delta}t = 10^{-11}, 10^{-10}$  and  $10^{-9}$  (or  $\Delta t = 10^4, 10^5$  and  $10^6$  s), which are  
704 equivalent to about 1/10, 1 and 10 days respectively. For these three time steps, and for  
705 the spatial resolution described in section 3, the calculated CPU time is of about 25, 3  
706 and 0.4 hours respectively (see figure 7). Considering that each simulation ran sequen-  
707 tially on a personal DELL computer equipped with 2.40 GHz Intel Xeon processors, these  
708 computational times demonstrate that the present numerical scheme makes it possible  
709 to run long-term simulations in the context of faults that cover several loading-unloading  
710 cycles in very reasonable simulation times. It is also interesting to note that, for the same  
711 three time steps for which convergence of the macroscopic model response is obtained,  
712 the calculated CPU time scales linearly with  $\frac{1}{\tilde{\Delta}t}$ , while it does not scale linearly for larger  
713 time steps ( $\tilde{\Delta}t > 10^{-9}$ ). This indicates that for the smallest three  $\tilde{\Delta}t$  values, the num-  
714 ber of steady-state stress redistribution subiterations performed at each time step is nearly  
715 constant and hence does not depend on the model time step. Conversely, for larger  $\tilde{\Delta}t$ 's,  
716 the system is driven further out of equilibrium at each time (i.e., deformation) increment.  
717 The number of subiterations required for the stresses to be redistributed over the domain  
718 and to become sub-critical again then increases significantly with  $\tilde{\Delta}t$ , thereby reducing  
719 the gain in computational time.

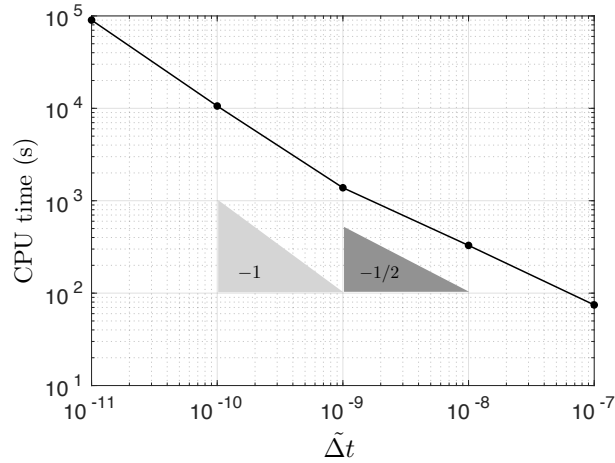


**Figure 7.** CPU time as a function of the (adimensional) model time step, for simulations using  $De_0 = 0.001$ ,  $\alpha = 4$ ,  $\delta d = 0.1$ , and  $T_h = 10^{-5}$  (see figure 6). Each simulation ran on a single (2.40 GHz Intel Xeon) processor on a personal DELL computer.

720

### 5.3 Sensitivity Analyses

721

#### 5.3.1 Healing Time, $T_h$

722

723

724

725

726

727

728

729

730

731

To investigate the effect of healing in the model, we compare the macroscopic stress-strain time series and the power spectral density (PSD) of the elastic energy released within the system during the propagation of damage,  $E_{brit}$  (see figure 8), for simulations using  $De_0 = 0.001, 0.1$  and  $10$  and four different values of the time for healing, corresponding to dimensional times of  $t_h = 10^8$  s,  $10^9$  s,  $10^{10}$  s and  $10^{11}$  s. All simulations use  $\alpha = 4$  and  $\delta d = 0.1$  and a value of the time step that ensures the convergence of the model response for each  $De_0$  value (see table 3). To account for the adjustment of the system following the first rupture, the first loading-unloading cycle is discarded when computing the PSD. Each curve shown on figure 8 is the average of 5 PSDs, on which a running mean centred over a window of 5 frequency values is applied.

732

733

734

735

736

737

738

739

740

741

742

The results clearly indicate that the prescribed time of healing controls the frequency of the loading-unloading cycles in the model: the larger the healing time, the lower the frequency. However in all of the simulations analyzed, the frequency associated to the prescribed healing time, indicated by the vertical lines on figure 8, does not correspond to the frequency of the loading-unloading cycles, but is systematically one or several orders or magnitude lower. This discrepancy is consistent that the interface always remains relatively highly damaged (see animation in Supporting Informations): less time is therefore required to re-initiate an avalanche of damaging events than it would be necessary if the system had completely heal. The discrepancy increases with the value of  $De_0$ , in agreement with a more elastic behaviour at high  $De_0$  number, i.e. a lower contribution from viscous dissipation that delays the reloading of the system.

743

744

745

746

747

748

749

Another tendency in the model behaviour emerges. For all values of  $De$  explored here, large values of the healing time (slow healing) lead to a  $E_{brit}$  release, or equivalently a damaging activity, that concentrates around a narrow range of low frequencies: the PSD is therefore flat for high frequencies. The corresponding stress-strain curves indicates that the stress is very rapidly and completely dissipated at each unloading (damaging) event. This behaviour can be explained by the fact that these large values of healing time approach the value of the bulk relaxation time (i.e, the relaxation time of undamaged el-

750 ements, or  $De_0$ ). Healing is therefore too slow relative to the dissipation of the stress to  
 751 play a significant role in the dynamics of the system.

752 Conversely, for low values of the healing time (fast healing), the PSD is flat for low  
 753 frequencies, with the activity concentrated around a narrow range of high frequencies,  
 754 and the stress is very rapidly but only partially dissipated at each damaging event: heal-  
 755 ing dominates the dynamics as  $T_h$  approaches the value of the relaxation time for the  
 756 stresses over the most damaged elements in the system (i.e.,  $De_{min}$ ). This value tends  
 757 to decrease inversely to  $T_h$ , as indicated by the coloured dotted lines on figure 8b.

758 For intermediate values of  $T_h$  and the two lowest values of  $De$  explored here (see  
 759 figure 8a to d), the slope of the PSDs indicates the presence of correlations in the tem-  
 760 poral evolution of  $E_{brit}$  (or, by extension, of the damaging activity). Such temporal cor-  
 761 relation or clustering is systematically observed for seismic tremors in subduction zones  
 762 and covers large spectrum of time scales, from hours to years (e.g., Idehara et al., 2014;  
 763 Frank et al., 2016; Poiata et al., 2021). Therefore, for each investigated  $De$  value, we iden-  
 764 tify an "optimal" healing time as the value of  $T_h$  for which these correlations span the  
 765 largest range of frequencies. It is important to note however, that the frequency at which  
 766 spatial correlations emerge in the system is upper bounded in all simulations due to the  
 767 finite dimension of the domain and the spatial resolution of the mesh. An intrinsic min-  
 768 imum time required to load the system can indeed be estimated, that depends only on  
 769 the mechanical strength (the ratio  $C_0/E_0$ ) and the spatial discretization of the model.  
 770 It corresponds to the time it takes to load an initially undamaged system until the first  
 771 damage event occurs, if all of the deformation is accommodated over a single single grid  
 772 element. Figure 8b shows that the frequency associated to this time, indicated as  $\frac{1}{t_{loading}}$   
 773 indeed marks the transition to a flat PSD at higher frequencies (for the other two sys-  
 774 tems, the time step employed is too large and does not allow exploring the model be-  
 775 haviour up to this frequency). For the "optimal"  $T_h$  values, corresponding to  $t_h = 10^{10}$   
 776 s for  $De = 0.001$  (figure 8a, b blue curve) and  $t_h = 10^9$  s for  $De = 0.1$  (figure 8c, d  
 777 green curve), the times associated with the loading, the relaxation of the stresses over  
 778 damaged elements and the healing of these elements are such that the three processes  
 779 interact and give rise to temporal correlations in the system that span a wide range of  
 780 time scales. Interestingly, the stress-strain behaviour of the model in these cases is char-  
 781 acterized by loading-unloading cycles in which the stress is sometimes partially and more  
 782 gradually dissipated and sometimes completely and drastically dissipated.

783 The optimal value of  $T_h$  decreases as the value of  $De_0$  increases, indicating that sys-  
 784 tems that are more elastic-solid like (large relaxation time,  $\lambda$ ) or characterized by a faster  
 785 dynamics (small deformation time,  $\frac{L}{U}$ , either due to a small horizontal extent,  $L$  or a fast  
 786 loading velocity,  $U$ ) must encompass faster healing mechanisms for these interactions to  
 787 take place.

788 However, for the largest  $De$  value used here (see figure 8e, f), temporal correlations  
 789 in the damaging activity are restricted to a small range of time scale and that, for all  
 790 of the  $T_h$  values explored, which we consider as lying in a realistic range in the context  
 791 of faults. The associated macroscopic stress-strain behaviour is characterized by regularly-  
 792 spaced, almost instantaneous (as opposed to transient) and complete unloading phases,  
 793 akin to the stick-slip behaviour observed in block-slider experiments. In the context of  
 794 slow earthquakes, this suggests that fault systems that are either very brittle (as near  
 795 the surface), small in extent, or loaded too rapidly cannot host the complex spatio-temporal  
 796 interactions that give rise to the observed transient deformations.

797 In the remaining sensitivity experiments (next section), we therefore leave the case  
 798 of  $De = 10$  aside and concentrate on simulations using  $De = 0.001$  and  $De = 0.1$ .  
 799 The optimal values of  $T_h$  identified for these two cases are indicated in green in table 3  
 800 and used by default in all simulations.

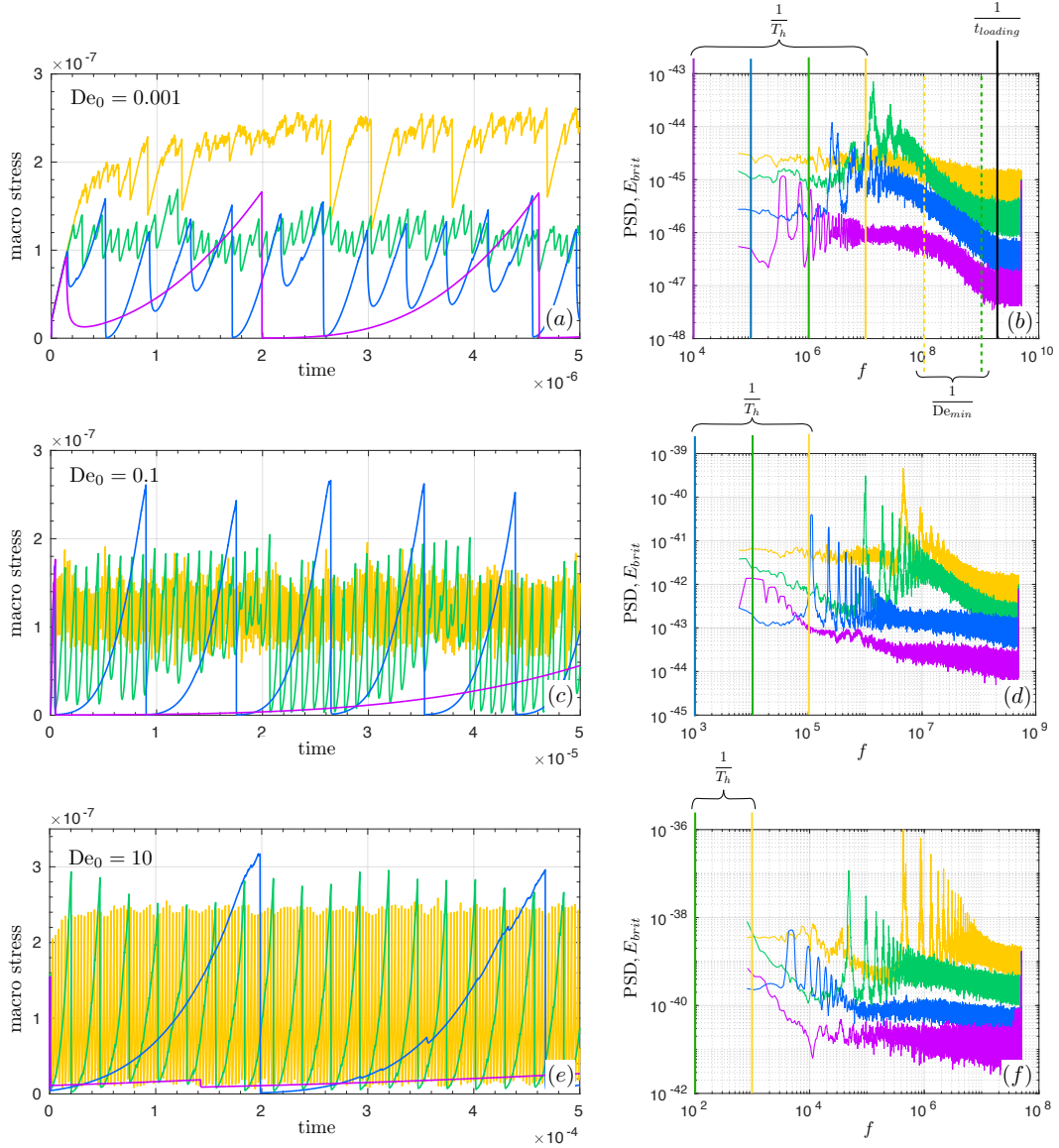


**Figure 8.** (a, c, d) Time series of the macroscopic stress and (b, d, f) power spectral density of the  $E_{brit}$  time series for simulations using (a, b)  $De_0 = 0.001$  ( $\tilde{\Delta}t = 10^{-10}$ ), (c, d)  $De_0 = 0.1$  ( $\tilde{\Delta}t = 10^{-9}$ ) and (e, f)  $De_0 = 10$  ( $\tilde{\Delta}t = 10^{-8}$ ) and four adimensional values of the prescribed time of healing, corresponding to dimensional values of  $t_h = 10^8$  s (yellow),  $10^9$  s (green),  $10^{10}$  s (blue) and  $10^{11}$  s (purple curve). All simulations use  $\alpha = 4$  and  $\delta d = 0.1$ . Each PSD curve is an average of 5 PSD calculated for 5 simulations initiated with different realizations of the noise on  $C$  and on which a running mean centred over a window of 5 frequency values is applied. The vertical lines on the PSDs indicate, when these frequencies fall within the range of frequencies covered in the simulations, the frequencies associated with the four adimensional values of the prescribed time of healing,  $1/T_h$  (plain coloured lines), the minimum time required to load the system,  $1/t_{loading}$  (plain black line), and the relaxation time associated with the most highly damaged elements in the system,  $1/De_{min}$  (dashed coloured lines).

### 5.3.2 Damage Parameter, $\alpha$ , and Damage Increment, $\delta d$

The last set of sensitivity experiment focuses on the brittle versus ductile character of the model behaviour. As the parameters  $\alpha$  and  $\delta d$  both regulate the rate at which the mechanical strength decreases locally and the behaviour changes from elastic solid-like and viscous fluid-like as a function of the level of damage, we expect their effect in this regard to be closely related. We therefore run a set of sensitivity experiments in which both parameters are varied simultaneously. The results of these experiments for the case of  $De_0 = 0.001$  ( $\tilde{\Delta}t = 10^{-10}$  s and  $T_h = 10^{-5}$  s) and  $De_0 = 0.1$  ( $\tilde{\Delta}t = 10^{-9}$  s and  $T_h = 10^{-4}$  s) are presented here.

We recall that for large values of  $\delta d$ , the local decrease in the elastic modulus,  $E$ , and apparent viscosity,  $\eta$ , at each damaging event is small. Conversely, for small values of  $\delta d$ , the local decrease in both  $E$  and  $\eta$  is large. Small values of  $\alpha$  lead to a small decrease in the relaxation time,  $\frac{\eta}{E}$ , at each damaged element (the damaged material retains stresses longer), while large values of  $\alpha$  lead to a large decrease in  $\frac{\eta}{E}$  (stresses are dissipated more readily).

#### Damage Increment, $\delta d$

Time series of the macroscopic stress (see figure 9 and 10, left panels) show that for all values of  $\alpha$ , increasing  $\delta d$  decreases the amplitude of the macroscopic stress drop associated with each unloading phase. As the stress is then never completely released at each loading-unloading cycle but stabilizes around a non-zero value, the loading time required for critical values of stress to be reached is reduced and the frequency of each cycle is thereby increased. For large values of  $\delta d$ , the PDF of the macroscopic damage increment, defined as in equation (18), is a truncated power law that is confined to small values of damage increment (see figure 9, right panels, which indicates that damage and deformation take place through isolated events, with small spatial extents).

Conversely, as  $\delta d$  is decreased, the amplitude in the variations of the macroscopic stress and the length of the loading-unloading cycles is increased. The unloading phases are characterized by sharper stress drops, indicating a more brittle behaviour. The distributions of the macroscopic damage increment are shifted towards larger values of damage increments.

#### Damage Parameter, $\alpha$

For a given value of  $\delta d$ , increasing the value of  $\alpha$  also induces larger macroscopic stress drops, lower frequency loading-unloading cycles and larger values of the macroscopic damage increment. Another effect of increasing  $\alpha$  is that the stress relaxation and re-increase in the vicinity of each stress minimum is more progressive in time, consistent with a more rapid decrease in the viscosity of the material at the onset of damaging and a more viscous fluid-like, i.e, dissipative, behaviour. The inverse is true when decreasing  $\alpha$ : the macroscopic behaviour is more brittle-like, with smaller but quasi-instantaneous stress relaxation phases and rapid, quasi-elastic stress loading phases.

#### Limit Cases

For virtually all values of  $\alpha$ , large values of  $\delta d$  give rise to a macroscopic stress-strain behaviour in which, after the initial elastic loading phase, where is no stress relaxation but rather a slow stress increase akin to the behaviour of a strain hardening creeping material. In this case, the PDFs of the macroscopic damage increment are upper-truncated power laws.

For small values of  $\alpha$  and small values of  $\delta d$  (e.g., see figure 9a or 10a for  $\alpha = 2$  and  $\delta d = 0.1$ ), the macroscopic behaviour, showing very sharp but small amplitude stress drops at each loading-unloading cycle, is reminiscent of a quasi-brittle material in which the stress relaxation through viscous-like deformation is insignificant. Each stress un-

loading phase is associated with a large avalanche of damage events that spans the entire domain. This explains the sharp mode in the PDF of the macroscopic damage increments at large increment values, which indicates that a characteristic avalanche size emerges, associated to a finite-size effect.

For large values of  $\alpha$  and small values of  $\delta d$  (e.g., see figure 9 or 10, d and e, for  $\alpha = 6$  or 8), the dissipation of stresses at the onset of damaging is the largest and the material becomes readily fluid-like. The stress is regularly and completely dissipated at each loading-unloading cycle. Local damage events are suppressed, which is expressed by the translation of the PDF of macroscopic damage increments towards larger increment values. The elastic redistribution of stresses are inherited and, therefore, the spatio-temporal correlations in the damaging activity are limited, which reduces the horizontal extent of avalanches and explains the appearance of broad modes in the PDFs of damage increments as well as their departure from a power law.

For intermediate values of  $\alpha$  (e.g.,  $\alpha = 3, 4$ , see figure 9 or 10, b and c) and small values of  $\delta d$  (0.1, 0.3, 0.5), the distribution of damage increments can be well-fitted with a power-law, that extends at large damage increment values. This suggests that the model simulates a mechanical behaviour that is, at least to some extent, scale-invariant. Unloading phases are characterized by stress drops of variable amplitudes, which are initially almost-instantaneous and then followed by a transient period.

## 6 Discussions

In this section, we further discuss what the model in its current state is able and not able to simulate in the context of fault deformation and slow earthquakes. To do so, we investigate the simulated dynamical behaviour for one specific case in which only  $\delta d$  is varied and all other mechanical parameters are identical. This simulation is identified by the black box on figure 10c and uses  $De_0 = 0.1$ ,  $\alpha = 4$ , with the corresponding default values of  $\tilde{\Delta}t$  and  $T_h$  (see table 3). In particular, we analyze the temporal evolution of pointwise displacements and velocities at the top boundary of the domain, which constitute proxies for the surface displacements and velocities as measured by Global Positioning Systems (GPS). In the following, we focus on the horizontal displacement and velocity at one point, the top left corner of the domain, which is furthest from the top right corner and therefore less influenced by the prescribed boundary condition there ( $u_x = 0$ ). It is important to note that on figures 11a, b and e, f, the prescribed velocity forcing,  $U$ , is subtracted from the recorded horizontal surface velocity. Also, the first few loading-unloading cycles are omitted from the analysis, as they are susceptible to carry the signature the first (outlier) rupture event.

The comparison of two simulations in which only the damage increment is varied between 0.1 and 0.5, summarized in figure 11, suggests that over a certain range of mechanical parameters the model can reproduce two different types of mechanical behaviour, which are more analogous to classical earthquakes and slow slip events, respectively. In the first case ( $\delta d = 0.1$ , left panels), the macroscopic shear stress on the top boundary indeed shows very rapid and large-amplitude release phases followed by short post-seismic stress relaxation phases and much longer reloading phases (see figure 11a). Each brutal stress release event is associated with a sharp reversal of the surface horizontal ( $x$ -) velocity and an equally sharp drop in the surface horizontal displacement (see figure 11c), which suggests a strong decoupling of the upper and lower plates following large damage events, reminiscent of classical earthquakes. In the second case ( $\delta d = 0.5$ , right panels), the asymmetry in the loading-unloading cycles is much less pronounced (see figures 11b and d): the stress is much more progressively dissipated at each loading-unloading cycle, which is accompanied by lower amplitude variations of the surface velocity and a progressive decrease in the surface displacement, reminiscent of slow slip events (e.g., Rogers & Dragert, 2003; Radiguet et al., 2016).

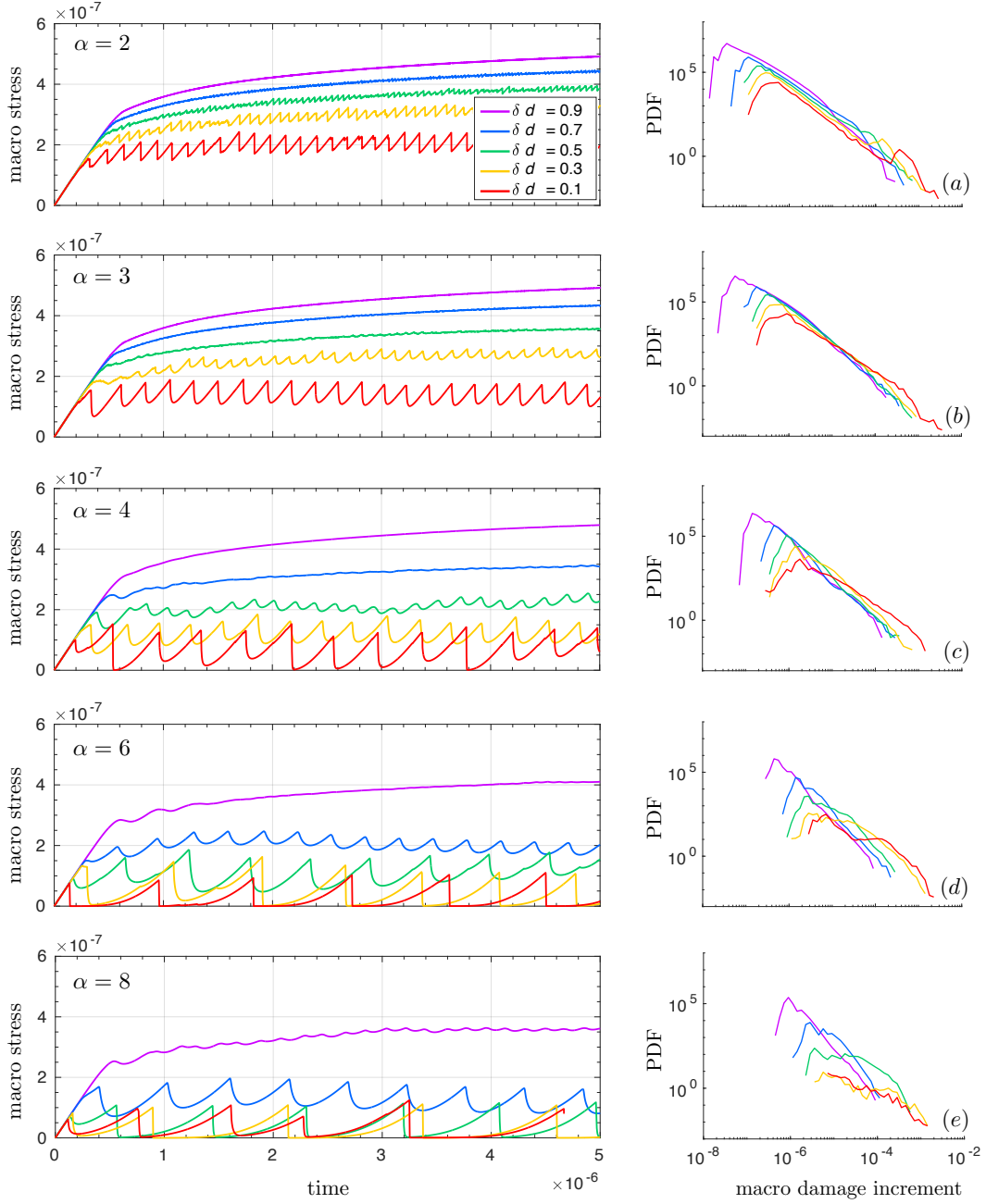


**Figure 9.** Time series of the macroscopic stress (left panels) and probability density function of the macroscopic damage increment (right panels) for  $De_0 = 0.001$  ( $\tilde{\Delta}t = 10^{-10}$ ,  $T_h = 10^{-5}$ ) and  $\delta d = 0.1, 0.3, 0.5, 0.7, 0.9$  and (a)  $\alpha = 2$ , (b)  $\alpha = 3$ , (c)  $\alpha = 4$ , (d)  $\alpha = 6$ , (e)  $\alpha = 8$ .

901 The damaging activity also differs between the two cases (see figures 11c, d). In  
 902 the first, fewer damage events are recorded over the same simulation time. The damag-  
 903 ing activity concentrates over large events that either precede (as in foreshocks) or co-  
 904 incide with stress release phases. In the second case, the damaging activity is more sym-  
 905 metric with respect to unloading phases, with damaging event both preceding (as in fore-  
 906 shocks) and following (as in aftershocks) stress release events.

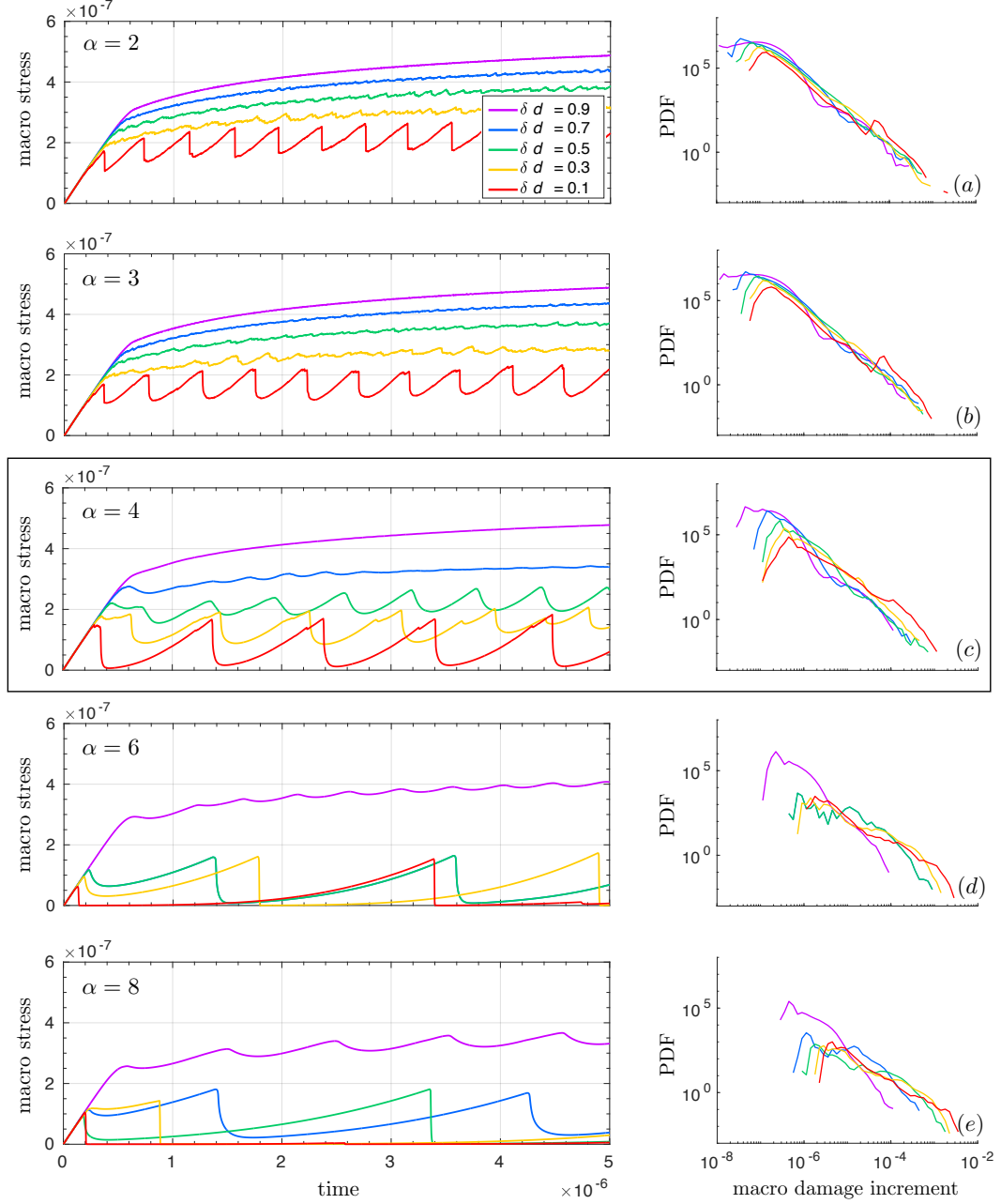


**Figure 10.** Time series of the macroscopic stress (left panels) and probability density function of the macroscopic damage increment (right panels) for  $De_0 = 0.1$  ( $\tilde{\Delta}t = 10^{-10}$ ,  $T_h = 10^{-5}$ ) and  $\delta d = 0.1, 0.3, 0.5, 0.7, 0.9$  and (a)  $\alpha = 2$ , (b)  $\alpha = 3$ , (c)  $\alpha = 4$ , (d)  $\alpha = 6$ , (e)  $\alpha = 8$ .

907 We further analyze the temporal evolution of the surface horizontal velocity during  
 908 each loading-unloading cycle, that is, over a period of time that starts at the onset  
 909 of each stress release phase and extends until the next phase, as delimited by the dashed  
 910 lines and arrows on figures 11a, b and c, d. In the first case, using  $\delta d = 0.1$ , the model  
 911 reproduces a power law decay of the velocity of the form

$$912 \quad V(t) \sim \frac{1}{t^p}, \quad (20)$$

913 where  $t$  is the time after the onset of stress release, and the exponent  $p$  is slightly smaller  
 914 than 1 (see figure 11e). This behaviour is akin to the observed Omori-like decay of post-  
 915 earthquake surface velocities (Perfettini & Avouac, 2004; Savage et al., 2005; Ingleby &  
 916 Wright, 2017; Periollat et al., 2022), which suggests that long-term temporal correlations  
 917 in the system control the evolution of post-earthquake surface velocities in the case of  
 918 classical earthquakes. It is important to note however that in the present case, this trend  
 919 spans a little more than two orders of magnitude, which is much less than what the ob-  
 920 servations cover. This is due to the fact that, for the purpose of this paper, we have cho-  
 921 sen our mechanical parameters (in particular the ratio  $C_0/E_0$ , which controls the sys-  
 922 tem loading time, see section 5.3.1) to be consistent with the typical recurrence time of  
 923 slow earthquakes, not with the larger time scales associated with classical earthquakes.

924 In the second case, using  $\delta d = 0.5$ , the post-rupture surface velocities are signif-  
 925 icantly smaller than in the previous case, and remain relatively stable for some time, be-  
 926 fore slowly decaying at larger timescales (see figure 11f). Such behaviour is similar to  
 927 what is observed during some largest SSEs for which the details of the displacement time  
 928 series can be resolved (Cotte et al., 2009; Radiguet et al., 2012).

929 These results suggest that the proposed modeling framework could be able to re-  
 930 produce both slow earthquakes and classical earthquakes. Numerically at least, it can  
 931 do it because it is efficient enough.

932 One important point however is that, not over the entire range of model param-  
 933 eter values but over the range that generates a mechanical behaviour most analogous to  
 934 slow and classical earthquakes, the model definitely exhibits a pseudo-periodic behaviour.  
 935 While it might be consistent with slow earthquakes (e.g., Dragert et al., 2001; Cotte et  
 936 al., 2009; Radiguet et al., 2016), such behaviour is less consistent with classical earth-  
 937 quakes. While recent studies have found that large (classical) earthquakes occur more  
 938 regularly than a purely random process (e.g., T. Williams et al., 2019; Griffin et al., 2020),  
 939 the temporal evolution of classical earthquakes in general is indeed more intermittent  
 940 and their recurrence time, hardly predictable (e.g., Gardner & Knopoff, 1974; Michael,  
 941 2011). We however believe that more variability in recurrence times and stress drop mag-  
 942 nitudes and an intermittent behaviour covering a wider range of time scales could be ob-  
 943 tained by incorporating additional physical components to the model. Leaving aside the  
 944 more complex dynamics of fluids aspects, we list some simple and logical options below.

945 The first consists in moving to a healing law that does not prescribe a unique, con-  
 946 stant healing time. Such a law would be in better agreement with available observations.  
 947 Measurements of relative seismic velocity changes after majors earthquakes indeed in-  
 948 dicate a healing rate that is not constant but decrease in time after the main shock, sug-  
 949 gesting that the damaged region within the fault regains strength rapidly in the early  
 950 stage of the interseismic period and progressively more slowly in the later stages (e.g.,  
 951 Li & Vidale, 2001; Brenguier et al., 2008). In the present model, this behaviour could  
 952 be parameterized through a logarithmic healing law that does not include any charac-  
 953 teristic time for healing but that instead depends locally on the time elapsed since the  
 954 last damage event. Such a law would agree with the aging version of the rate-and-state  
 955 interface model of (Ruina, 1983), which imply that the surfaces that are in contact and  
 956 at rest strengthen logarithmically and would allow the system to evolve in a less deter-  
 957 ministic manner.

958 The second consists in accounting for a representation of the rheological stratifi-  
 959 cation of subduction zones, which is known to depend strongly on temperature (e.g. Pea-  
 960 cock, 2009) and therefore on depth. In the present 2-dimensional, idealized numerical  
 961 experiments, this stratification could be coarsely accounted for by allowing the bulk, un-  
 962 damaged viscosity of the host rock in the two plates to vary as a simple function (for in-  
 963 stance, linear) of the horizontal distance ( $x$ ) parallel to the interface, so that to repre-

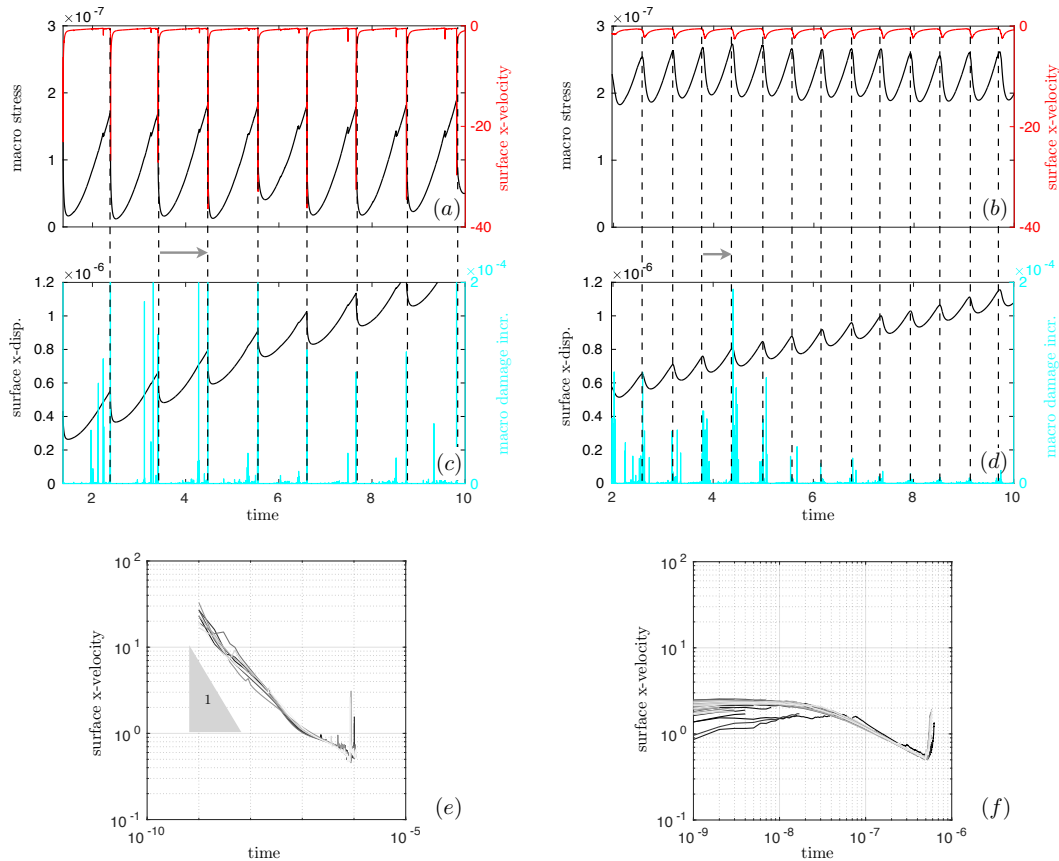


**Figure 11.** (a, b) Temporal evolution of the macroscopic stress (black curve) and of the surface  $x$ -velocity at the upper left corner of the domain (red curve) for a simulation in which  $De_0 = 0.1$  ( $\tilde{\Delta}t = 10^{-9}$ ,  $T_h = 10^{-4}$ ),  $\alpha = 4$  and (a)  $\delta d = 0.1$  and (b)  $\delta d = 0.5$ . (c, d) Corresponding temporal evolution of the cumulated surface  $x$ -displacement at the upper left corner of the domain (black curve) and of macroscopic damage increment (cyan curve). (e, f) Corresponding surface  $x$ -velocity at the upper left corner of the domain as a function of the time elapsed between each unloading event, as indicated by the dashed lines and arrows on figures (a) to (d). In figures a, b, e and f, the prescribed forcing velocity,  $U$ , is subtracted from the  $x$ -velocity.

964 sent a more brittle (high viscosity) behaviour towards the surface and a more ductile (low  
 965 viscosity) behaviour at depth. Such a dependence of the viscosity with depth would al-  
 966 low mitigating the impact of finite size effects and at the same time, exploring spatial  
 967 and temporal interactions between the different types of mechanical behaviours simul-  
 968 ated by the model, that is, an essentially brittle behaviour akin to low-depth, classical  
 969 earthquakes, a mixed brittle-ductile behaviour akin to slow-slip events and diffuse, duc-  
 970 tile deformations akin to the deeper parts of subduction zones. In the same line of ideas,  
 971 the use of the full Burger model, that is, incorporating the Kelvin component that was  
 972 left aside in the present experiments but which is meant to accounts for the deforma-  
 973 tion of the mantle (e.g., Nur & Mavko, 1974; Pollitz et al., 2001), would act as an ad-  
 974 ditional source of post-seismic transient deformation and as such would bring some ex-  
 975 tra complexity in the temporal behaviour of the model.

976 The third addition would account for friction, which most likely plays a first-order  
 977 role in the brittle part of the shear zone (e.g., Byerlee, 1967; Scholz, 1998, and many oth-  
 978 ers), where asperities can become locked, thereby allowing for stresses to locally build-

979 up and local quakes to be triggered. To simulate the effect of static friction in a simple  
 980 manner, an additional threshold on the the minimum stress required for the occurrence  
 981 of viscous deformation (as opposed to damage) could be coupled to the viscous stress  
 982 dissipation term of equation 1. This criterion, of the cohesion-less Mohr-Coulomb type,  
 983 would ensure that for low states of stress, slip would be hindered and elastic stresses would  
 984 build-up locally towards critically.

## 985 7 Conclusions

986 In this paper, we have presented a continuum, volumetric mechanical model suited  
 987 for modelling slow earthquakes. We have also presented a numerical framework for this  
 988 model that is efficient enough to cover several deformation cycles in very reasonable sim-  
 989 ulation times in a 2-dimensional setup, while allowing to resolve both the very short-term  
 990 and localized damage initiation and propagation processes associated with the co-seismic  
 991 rupture and the diffuse deformations within the bulk of the host rock that relaxes stresses  
 992 over very long time scales. In between these very short and very long time scales and  
 993 over a certain range of parameters, the model can simulate a correlated seismic (i.e., dam-  
 994 age) activity as well as different transient, seismic and aseismic processes akin to clas-  
 995 sical and slow earthquakes, such as the post-seismic stress relaxation phase.

996 In particular, the fact that the model can reproduce the observed Omori-like de-  
 997 cay in surface post-seismic velocities over a certain range of mechanical parameter val-  
 998 ues, even in the presently highly idealized simulation setup, is an important result, as  
 999 it supports the hypothesis of (Ingleby & Wright, 2017) that visco-elastic models, either  
 1000 of the Maxwell or the Burgers type, require a continuously varying viscosity or, equiv-  
 1001 alently, a continuously varying relaxation time, to reproduce this observed trend. Here,  
 1002 this continuous variation in the relaxation time is achieved by applying a unique rheo-  
 1003 logical law over the entire system, hence avoiding the need to prescribe the mechanical  
 1004 behaviour in different parts of the system or the location of the shearing zone, but let-  
 1005 ting both the elastic modulus and viscosity evolve in time and in space as simple func-  
 1006 tions of the level of damage.

1007 Leaving aside for the moment the inclusion of the dynamics of fluids, we have sug-  
 1008 gested several simple additions to the current rheological framework that aim at extend-  
 1009 ing its application to the representation of the entire seismic "cycle": that is a deforma-  
 1010 tion that comprises both classical and slow earthquakes. The one-by-one inclusion of these  
 1011 additions - a logarithmic, time-since-damage-dependant healing law, a variation of the  
 1012 viscosity with depth and a deformation threshold for static friction -, the evaluation of  
 1013 their respective impact on the simulated mechanical behaviour and the assessment of their  
 1014 relative contribution towards a more realistic reproduction of the deformation cycle of  
 1015 faults is the aim of our next paper.

## 1016 Appendix A Adimensional system of equations

1017 The model is made adimensional with respect to

- 1018 1. the horizontal extent,  $L$ , of the domain in the direction of the forcing,
- 1019 2. the prescribed forcing velocity,  $U$ ,
- 1020 3. the undamaged elastic modulus,  $E_0$ .

1021 The time characterizing the deformation process is therefore  $T = \frac{L}{U}$ . In the following,  
 1022 the superscript '˜' is used for all dimension-less variables and operators, which are listed  
 1023 in table A1.

Variables, dimensions and operators		Non-dimensional equivalent
Spatial (2D) dimension	$\mathbf{x}$	$\tilde{\mathbf{x}} = \frac{\mathbf{x}}{L}$
Time	$t$	$\tilde{t} = \frac{t}{T}$
Velocity	$\mathbf{u}$	$\tilde{\mathbf{u}} = \frac{\mathbf{u}}{U}$
Internal stress	$\sigma$	$\tilde{\sigma} = \frac{\sigma}{E_0}$
Level of damage	$d, d'$	$d, d'$
Del Operator	$\nabla$	$\tilde{\nabla} = L\nabla$

**Table A1.** Dimensional model variables and operators and their adimensional counterpart.

1024 In terms of these adimensional variables and operators, the momentum equation  
1025 reads:

$$1026 \tilde{\nabla} \cdot \tilde{\sigma} = 0 \quad (\text{A1})$$

1027 for either the pre- or post-damage stress,  $\sigma$  or  $\sigma'$ .

1028 The full constitutive equation becomes

$$1029 \frac{U}{L} E_0 \frac{\partial \tilde{\sigma}}{\partial \tilde{t}} + \frac{E_0}{\lambda_0(1-d^{\alpha-1})} \tilde{\sigma} = \frac{U}{L} E_0 (1-d) \mathbf{K} : \tilde{\varepsilon},$$

1030 or

$$1031 \frac{\partial \tilde{\sigma}}{\partial \tilde{t}} + \frac{1}{\text{De}_0(1-d)^{\alpha-1}} \tilde{\sigma} = (1-d) \mathbf{K} : \tilde{\varepsilon}, \quad (\text{A2})$$

1032 where  $\text{De}_0 = \frac{\eta_0 U}{E_0 L}$  is the (undamaged) Deborah number. The constitutive equation for  
1033 the post-damage stress redistribution is:

$$1034 \tilde{\sigma}' - \delta d \tilde{\sigma} = (1-d') \mathbf{K} : \tilde{\varepsilon}. \quad (\text{A3})$$

1035 Damage being a non-dimensional variable, the damage equation (5) is itself adimensional:

$$1036 1 - d' = \delta d (1 - d). \quad (\text{A4})$$

1037 The adimensional healing equation reads

$$1038 \frac{1}{T} \frac{\partial d'}{\partial \tilde{t}} = -\frac{1}{t_h} d', \quad 0 \leq d' < 1,$$

1039 or

$$1040 \frac{\partial d'}{\partial \tilde{t}} = -\frac{1}{T_h} d', \quad 0 \leq d' < 1. \quad (\text{A5})$$

1041 where  $T_h = \frac{t_h}{T}$ .

## 1042 Appendix B Numerical Scheme

1043 Here we present the time discretization and the numerical algorithm employed to  
1044 solve the system of equations in the shearing experiments. For simplicity, the superscript  
1045 '~~' for adimensional variables is drop in the following notations.

1046 This system of equations (A1 for  $\sigma$  and for  $\sigma'$ , A2, A3, A4, A5) forms a problem  
1047 that is solved for the following unknowns :  $\dot{\varepsilon}$  and  $\varepsilon'$  (3 components each),  $\sigma$  and  $\sigma'$  (3  
1048 components each) and  $d'$ , starting from an initial state of rest and zero damage. It is solved

1049 over a closed 2-dimensional domain  $\Omega \in \mathbb{R}$  (see figure 4), with an external boundary  
 1050 partitioned as  $\partial\Omega = \Gamma_{\text{top}}, \Gamma_{\text{bottom}}, \Gamma_{\text{left}}, \Gamma_{\text{right}}$ . A constant  $x$ -velocity is applied on  $\Gamma_{\text{bottom}}$ .  
 1051 It is fixed to 0 during the steady-state, stress redistribution process. The  $z$ -velocity is  
 1052 fixed to 0 on  $\Gamma_{\text{bottom}}$  and  $u_x = 0$  on the right upper corner of the domain. The top and  
 1053 lateral boundaries are free, hence  $\sigma \cdot \mathbf{n} = 0$  on  $\Gamma_{\text{top}}, \Gamma_{\text{left}}$  and  $\Gamma_{\text{right}}$ .

### 1054 ***B01 Time discretization***

1055 We discretize the time,  $t$ , such that  $t_n = n\Delta t$ , with  $\Delta t > 0$  and  $n = 0, 1, 2, \dots$   
 1056 and use a backward Euler (implicit) scheme of order 1. Expressing the strain rate tensor  
 1057 as  $\dot{\epsilon} = D(\mathbf{u}) = \frac{1}{2}(\nabla\mathbf{u} + \nabla\mathbf{u}^T)$  and the strain tensor as  $D(\mathbf{u})\Delta t$ , the time-discretized  
 1058 system of equations reads:

$$\begin{aligned}
 1059 \quad & \nabla \cdot \sigma^{n+1} = 0, \\
 1060 \quad & \frac{\sigma^{n+1} - \sigma^n}{\Delta t} + \frac{1}{\text{De}_0 (1 - d^n)^{\alpha-1}} \sigma^{n+1} = (1 - d^n) \mathbf{K} : D(\mathbf{u}^{n+1}), \\
 1061 \quad & 1 - d'^n = \delta d (1 - d^n) \\
 1062 \quad & \nabla \cdot \sigma'^{n+1} = 0, \\
 1063 \quad & \sigma'^{n+1} - \delta d \sigma^{n+1} = (1 - d'^n) \mathbf{K} : D(\mathbf{u}'^{n+1} \Delta t), \\
 1064 \quad & \frac{d'^{n+1} - d'^n}{\Delta t} = -\frac{1}{T_h} d'^n, \quad 0 < d'^{n+1} \leq 1.
 \end{aligned}$$

1065 The numerical scheme divides this time-discretized problem,  $P_d$ , into three subprob-  
 1066 lems. Using the superscript  $k = 0, 1, 2, \dots$  for the steady-state stress-redistribution sub-  
 1067 iteration in subproblem 2, these problems reads:

- 1068  $(P1_d)$  The momentum and constitutive equations are first solved simultaneously for the  
 1069 fields of velocity and stress,  $\sigma^{n+1}$  and  $\mathbf{u}^{n+1}$  at the current time step, by apply-  
 1070 ing the constant  $x$ -velocity forcing on  $\Gamma_{\text{bottom}}$  and the other boundary conditions  
 1071 and using the level of damage at the previous time step,  $d^n$ .
- 1072  $(P2_d)$  The steady-state stress redistribution equations are solved iteratively, with the  $x$ -velocity  
 1073 on  $\Gamma_{\text{bottom}}$  now set to zero. In this subproblem, the damage equation is first solved  
 1074 for  $d'^{n,k+1}$  by comparing the field of stress at the current subiteration,  $\sigma^{n+1,k}$ , to  
 1075 the local damage criteria,  $\sigma_c$ . The updated level of damage is then substituted into  
 1076 the post-damage constitutive equation. Together with the momentum equation,  
 1077 it is solved for the adjusted fields of velocity,  $\mathbf{u}'^{n+1,k+1}$ , and stress,  $\sigma'^{n+1,k+1}$ . These  
 1078 steps are iterated until all of the adjusted stresses become sub-critical. Then the  
 1079 post-damage level of damage,  $d'^n$ , is set to  $d'^{n,k+1}$ .
- 1080  $(P3_d)$  The healing equation is finally solved for the level of damage at the current time  
 1081 step,  $d'^{n+1}$  and  $d^{n+1}$  is set to  $d'^{n+1}$ .

1082 The complete algorithm reads:

1083 *Initialization* ( $n = 0$ )

$$\begin{aligned}
 1084 \quad & \mathbf{u}^n = 0 \text{ in } \Omega, \\
 1085 \quad & \sigma^n = 0 \text{ in } \Omega, \\
 1086 \quad & d^n = d'^n = 0 \text{ in } \Omega.
 \end{aligned}$$

1087 For  $n \geq 0$ , set  $k = 0$

1088 (P1<sub>d</sub>) With  $\sigma^n$  and  $d^n$  known, find  $\sigma^{n+1}$  and  $\mathbf{u}^{n+1}$  such that

$$1089 \quad \nabla \cdot \sigma^{n+1} = 0,$$

$$1090 \quad \frac{\sigma^{n+1} - \sigma^n}{\Delta t} + \frac{1}{\text{De}_0(1-d^n)^{\alpha-1}} \sigma^{n+1} = (1-d^n) \mathbf{K} : D(\mathbf{u}^{n+1}),$$

1091

1092 and with

$$1093 \quad u_z^{n+1} = 0 \text{ on } \Gamma_{\text{bottom}},$$

$$1094 \quad u_x^{n+1} = 1 \text{ on } \Gamma_{\text{bottom}},$$

$$1095 \quad u_x^{n+1} = 0 \text{ on } \Gamma_{\text{top}} \cap \Gamma_{\text{right}},$$

$$1096 \quad \sigma^{n+1} \cdot \mathbf{n} = 0 \text{ on } \Gamma_{\text{top}}, \Gamma_{\text{left}} \text{ and } \Gamma_{\text{right}}, .$$

1097 IF anywhere in  $\Omega$   $\sigma_1^{n+1} > q\sigma_2^{n+1} + \sigma_c$ , set  $\sigma'^{n+1,k} = \sigma^{n+1}$  and  $d'^{n,k} = d^n$ .

1098 (P2<sub>d</sub>) For  $k \geq 0$ ,

1099 1. Find  $d'^{n,k+1}$  such that

$$1100 \quad 1 - d'^{n,k+1} = \delta d (1 - d'^{n,k}),$$

1101 2. Find  $\sigma^{n+1,k+1}$  and  $\mathbf{u}^{n+1,k+1}$  such that

$$1102 \quad \nabla \cdot \sigma^{n+1,k+1} = 0,$$

$$1103 \quad \sigma'^{n+1,k+1} - \delta d \sigma'^{n+1,k} = E_0(1 - d'^{n,k+1}) \mathbf{K} : (D(\mathbf{u}'^{n+1,k+1}) \Delta t)$$

1104 and with

$$1105 \quad u_z'^{n+1,k+1} = 0 \text{ on } \Gamma_{\text{bottom}},$$

$$1106 \quad u_x'^{n+1,k+1} = 0 \text{ on } \Gamma_{\text{bottom}},$$

$$1107 \quad u_x'^{n+1,k+1} = 0 \text{ on } \Gamma_{\text{top}} \cap \Gamma_{\text{right}},$$

$$1108 \quad \sigma'^{n+1,k+1} \cdot \mathbf{n} = 0 \text{ on } \Gamma_{\text{top}}, \Gamma_{\text{left}} \text{ and } \Gamma_{\text{right}}, .$$

1109 IF  $\sigma_1'^{n+1,k+1} \leq q\sigma_2'^{n+1,k+1} + \sigma_c$ ,  
 1110 STOP and set  $\sigma^{n+1} = \sigma'^{n+1,k+1}$  and  $d'^n = d'^{n,k+1}$  (P3<sub>d</sub>) Find  $d'^{n+1}$  such that

$$1111 \quad \frac{d'^{n+1} - d'^n}{\Delta t} = -\frac{1}{T_h} d'^n, \quad 0 < d'^{n+1} \leq 1.$$

1112 Set  $d^{n+1} = d'^{n+1}$ .

## 1113 Appendix C Convergence

1114 Figure C1 shows the probability density function of  $E_{\text{brit}}/\tilde{\Delta}t$  obtained in the case  
 1115 of  $\text{De}_0 = 0.1$  and  $\text{De}_0 = 10$ , using  $\alpha = 4$ ,  $\delta d = 0.1$  and  $T_h = 10^{-4}$  and  $T_h = 10^{-3}$  re-  
 1116 spectively. The PDFs indicate that the macroscopic model response converges as  $\tilde{\Delta}t$  is  
 1117 decreased, as for the case of  $\text{De}_0 = 0.001$  described in section 5.2. The values of  $\tilde{\Delta}t$  for  
 1118 which the response is not converged are indicated in red in table 3. The value of  $\tilde{\Delta}t$  cor-  
 1119 responding to each  $\text{De}_0$  value and used in the sensitivity analyses on  $T_h$ ,  $\alpha$  and  $\delta d$  are  
 1120 indicated in green in the same table.

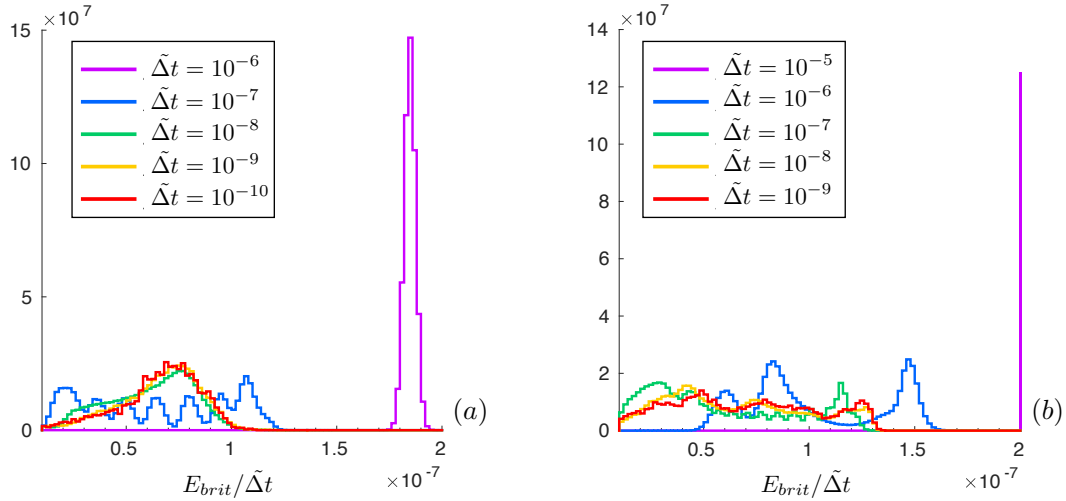


**Figure C1.** Probability density function of  $E_{brit}/\tilde{\Delta}t$  for simulations using  $\alpha = 4$ ,  $\delta d = 0.1$  and (a)  $De_0 = 0.1$ ,  $T_h = 10^{-4}$  and  $\tilde{\Delta}t = 10^{-10}, 10^{-9}, 10^{-8}, 10^{-7}, 10^{-6}$  and (b)  $De_0 = 10$ ,  $T_h = 10^{-3}$  and  $\tilde{\Delta}t = 10^{-9}, 10^{-8}, 10^{-7}, 10^{-6}, 10^{-5}$  (corresponding to  $\Delta t = 10^4$  s,  $10^5$  s,  $10^6$  s,  $10^7$  s,  $10^8$  s respectively).

## 1121 Acknowledgments

1122 The authors thank David Amitrano and Jean-Luc Got for insightful discussions about  
 1123 this paper and related topics. V. D., N. S. and M. C. acknowledge support from the Eu-  
 1124 ropean Research Council (ERC) under the European Union's Horizon 2020 research and  
 1125 innovation program (Grant agreements no 787399, SEISMAZE for N. S. and V. D. and  
 1126 742335, F-IMAGE for M. C.).

1127 The outputs of numerical simulations can be found at: XXXZenodo. The post-processing  
 1128 MATLAB codes used to produce the figures and movie presented in this paper and SI  
 1129 are available at: <https://github.com/vdansereau/Multi-Scale-Deformation-Cycle-AGU-Solid-Earth-paper.git>. The model equations and the numerical scheme (time  
 1130 and space discretizations) are fully described in sections 2.4 and 3 of the main text and  
 1131 in the Appendix A and Appendix B, to allow reproducibility. The C++ library RHE-  
 1132 OLEF used to set the domain and boundary conditions and to solve the set of equations  
 1133 is documented and available for download at <https://membres-ljk.imag.fr/Pierre.Saramito/rheolef/html/index.html>.  
 1134  
 1135

## 1136 References

- 1137 Amitrano, D. (2003). Brittle-ductile transition and associated seismicity: Exper-  
 1138 imental and numerical studies and relationship with the  $b$  value. *Journal of*  
 1139 *Geophysical Research*, *108*(B1). doi: 10.1029/2001JB000680  
 1140 Amitrano, D., Grasso, J.-R., & Hantz, D. (1999). From diffuse to localised damage  
 1141 through elastic interaction. *Geophysical Research Letters*, *26*(14), 2109-2112.  
 1142 Angiboust, S., Kirsch, J., Oncken, O., G., J., Monié, P., & Rybacki, E. (2015).  
 1143 Probing the transition between seismically coupled and decoupled segments  
 1144 along an ancient subduction interface. *Geochemistry, Geophysics, Geosys-*  
 1145 *tems*, *16*(6), 1905-1922. Retrieved from [https://agupubs.onlinelibrary](https://agupubs.onlinelibrary.wiley.com/doi/abs/10.1002/2015GC005776)  
 1146 [.wiley.com/doi/abs/10.1002/2015GC005776](https://agupubs.onlinelibrary.wiley.com/doi/abs/10.1002/2015GC005776) doi: [https://doi.org/10.1002/](https://doi.org/10.1002/2015GC005776)  
 1147 [2015GC005776](https://doi.org/10.1002/2015GC005776)  
 1148 Ashby, M. F., & Sammis, C. G. (1990). The damage mechanics of brittle solids in

- 1149 compression. *pure and applied geophysics*, 133(3), 489–521. Retrieved from  
 1150 <https://doi.org/10.1007/BF00878002> doi: 10.1007/BF00878002
- 1151 Audet, P., Bostock, M., Christensen, N., & Peacock, S. M. (2009). Seismic evidence  
 1152 for overpressured subducted oceanic crust and megathrust fault sealing. *Nature*,  
 1153 457(7225), 76–78. doi: 10.1038/nature07650
- 1154 Ben-Zion, Y., & Lyakhovskiy, V. (2002). Accelerated seismic release and related  
 1155 aspects of seismicity patterns on earthquake faults. In M. Matsu'ura,  
 1156 P. Mora, A. Donnellan, & X.-c. Yin (Eds.), *Earthquake processes: Physical modelling, numerical simulation and data analysis part ii* (pp. 2385–  
 1157 2412). Basel: Birkhäuser Basel. Retrieved from [https://doi.org/10.1007/](https://doi.org/10.1007/978-3-0348-8197-5_12)  
 1158 [978-3-0348-8197-5\\_12](https://doi.org/10.1007/978-3-0348-8197-5_12) doi: 10.1007/978-3-0348-8197-5\_12
- 1160 Ben-Zion, Y., & Lyakhovskiy, V. (2006, 04). Analysis of aftershocks in a lithospheric  
 1161 model with seismogenic zone governed by damage rheology. *Geophysical Journal International*,  
 1162 165(1), 197–210. Retrieved from [https://doi.org/10](https://doi.org/10.1111/j.1365-246X.2006.02878.x)  
 1163 [.1111/j.1365-246X.2006.02878.x](https://doi.org/10.1111/j.1365-246X.2006.02878.x) doi: 10.1111/j.1365-246X.2006.02878.x
- 1164 Bhat, H. S., Rosakis, A. J., & Sammis, C. G. (2012, 04). A Micromechanics Based  
 1165 Constitutive Model for Brittle Failure at High Strain Rates. *Journal of Applied Mechanics*,  
 1166 79(3). Retrieved from <https://doi.org/10.1115/1.4005897>  
 1167 (031016) doi: 10.1115/1.4005897
- 1168 Bos, B., & Spiers, C. J. (2002). Fluid-assisted healing processes in gouge-bearing  
 1169 faults: Insights from experiments on a rock analogue system. *pure and applied geophysics*,  
 1170 159(11), 2537–2566. Retrieved from [https://doi.org/10.1007/](https://doi.org/10.1007/s00024-002-8747-2)  
 1171 [s00024-002-8747-2](https://doi.org/10.1007/s00024-002-8747-2) doi: 10.1007/s00024-002-8747-2
- 1172 Bostock, M. G., Royer, A. A., Hearn, E. H., & Peacock, S. M. (2012). Low  
 1173 frequency earthquakes below southern vancouver island. *Geochemistry, Geophysics, Geosystems*,  
 1174 13(11), Q11007. doi: [https://doi.org/10.1029/](https://doi.org/10.1029/2012GC004391)  
 1175 [2012GC004391](https://doi.org/10.1029/2012GC004391)
- 1176 Brenguier, F., Campillo, M., Hadziioannou, C., Shapiro, N. M., Nadeau, R. M.,  
 1177 & Larose, E. (2008). Postseismic relaxation along the san andreas fault at  
 1178 parkfield from continuous seismological observations. *Science*, 321(5895),  
 1179 1478–1481. Retrieved from [https://science.sciencemag.org/content/321/](https://science.sciencemag.org/content/321/5895/1478)  
 1180 [5895/1478](https://science.sciencemag.org/content/321/5895/1478) doi: 10.1126/science.1160943
- 1181 Brown, K. M., Tryon, M. D., DeShon, H. R., Dorman, L. M., & Schwartz, S. Y.  
 1182 (2005). Correlated transient fluid pulsing and seismic tremor in the costa rica  
 1183 subduction zone. *Earth and Planetary Science Letters*, 238(1), 189–203. doi:  
 1184 <https://doi.org/10.1016/j.epsl.2005.06.055>
- 1185 Brudzinski, M. R., & Allen, R. M. (2007, 10). Segmentation in episodic tremor and  
 1186 slip all along Cascadia. *Geology*, 35(10), 907–910. doi: 10.1130/G23740A.1
- 1187 Burov, E. B. (2011). Rheology and strength of the lithosphere. *Marine and Petroleum Geology*,  
 1188 28(8), 1402 - 1443. Retrieved from [http://](http://www.sciencedirect.com/science/article/pii/S0264817211001425)  
 1189 [www.sciencedirect.com/science/article/pii/S0264817211001425](http://www.sciencedirect.com/science/article/pii/S0264817211001425) doi:  
 1190 <https://doi.org/10.1016/j.marpetgeo.2011.05.008>
- 1191 Burridge, R., & Knopoff, L. (1967). Model and theoretical seismicity. *Bulletin of the Seismological Society of America*,  
 1192 57(3), 341–371.
- 1193 Byerlee, J. D. (1967). Frictional characteristics of granite under high con-  
 1194 fining pressure. *Journal of Geophysical Research*, 72(14), 3639–3648.  
 1195 Retrieved from <http://dx.doi.org/10.1029/JZ072i014p03639> doi:  
 1196 [10.1029/JZ072i014p03639](https://doi.org/10.1029/JZ072i014p03639)
- 1197 Byerlee, J. D. (1978). Friction of rocks. *Pure and Applied Geophysics*, 116, 615–626.  
 1198 doi: <https://doi.org/10.1007/BF00876528>
- 1199 Caine, J. S., Evans, J. P., & Forster, C. B. (1996, 11). Fault zone architecture  
 1200 and permeability structure. *Geology*, 24(11), 1025–1028. Retrieved from  
 1201 [https://doi.org/10.1130/0091-7613\(1996\)024<1025:FZAAPS>2.3.CO;2](https://doi.org/10.1130/0091-7613(1996)024<1025:FZAAPS>2.3.CO;2)  
 1202 doi: 10.1130/0091-7613(1996)024(1025:FZAAPS)2.3.CO;2
- 1203 Carlson, J. M., & Langer, J. S. (1989). Properties of earthquakes generated by fault

- 1204 dynamics. *Phys. Rev. Lett.*, *62*, 2632–2635. Retrieved from <https://link>  
 1205 [.aps.org/doi/10.1103/PhysRevLett.62.2632](https://link.aps.org/doi/10.1103/PhysRevLett.62.2632) doi: 10.1103/PhysRevLett.62  
 1206 [.2632](https://link.aps.org/doi/10.1103/PhysRevLett.62.2632)
- 1207 Carrier, A., Got, J.-L., Peltier, A., Ferrazzini, V., Staudacher, T., Kowalski, P.,  
 1208 & Boissier, P. (2015, January). A damage model for volcanic edifices:  
 1209 Implications for edifice strength, magma pressure, and eruptive processes.  
 1210 *Journal of Geophysical Research (Solid Earth)*, *120*(1), 567–583. doi:  
 1211 [10.1002/2014JB011485](https://doi.org/10.1002/2014JB011485)
- 1212 Chen, J., Niemeijer, A. R., & Spiers, C. J. (2017). Microphysically derived expres-  
 1213 sions for rate-and-state friction parameters,  $a$ ,  $b$ , and  $dc$ . *Journal of Geophys-*  
 1214 *ical Research: Solid Earth*, *122*(12), 9627–9657. Retrieved from [https://](https://agupubs.onlinelibrary.wiley.com/doi/abs/10.1002/2017JB014226)  
 1215 [agupubs.onlinelibrary.wiley.com/doi/abs/10.1002/2017JB014226](https://agupubs.onlinelibrary.wiley.com/doi/abs/10.1002/2017JB014226) doi:  
 1216 <https://doi.org/10.1002/2017JB014226>
- 1217 Cotte, N., Walpersdorf, A., Kostoglodov, V., Vergnolle, M., Santiago, J.-A., &  
 1218 Campillo, M. (2009). Anticipating the next large silent earthquake in mex-  
 1219 ico. *Eos, Transactions American Geophysical Union*, *90*(21), 181–182. doi:  
 1220 <https://doi.org/10.1029/2009EO210002>
- 1221 Cruz-Atienza, V. M., Villafuerte, C., & Bhat, H. S. (2018). Rapid tremor migration  
 1222 and pore-pressure waves in subduction zones. *Nature Communications*, *9*(1),  
 1223 2900. doi: 10.1038/s41467-018-05150-3
- 1224 Dansereau, V. (2016b). *A Maxwell-Elasto-Brittle model for the drift and deforma-*  
 1225 *tion of sea ice* (Theses, Université Grenoble Alpes). Retrieved from [https://](https://tel.archives-ouvertes.fr/tel-01316987)  
 1226 [tel.archives-ouvertes.fr/tel-01316987](https://tel.archives-ouvertes.fr/tel-01316987)
- 1227 Dansereau, V., Weiss, J., Saramito, P., & Lattes, P. (2016a). A Maxwell-elasto-  
 1228 brittle rheology for sea ice modelling. *The Cryosphere*, *10*, 1339–1359.
- 1229 Dieterich, J. H. (1978). Time-dependent friction and the mechanics of stick-  
 1230 slip. *pure and applied geophysics*, *116*(4), 790–806. Retrieved from  
 1231 <https://doi.org/10.1007/BF00876539> doi: 10.1007/BF00876539
- 1232 Dieterich, J. H. (1979a). Modeling of rock friction: 1. experimental results and  
 1233 constitutive equations. *Journal of Geophysical Research: Solid Earth*, *84*(B5),  
 1234 2161–2168. Retrieved from [https://agupubs.onlinelibrary.wiley.com/](https://agupubs.onlinelibrary.wiley.com/doi/abs/10.1029/JB084iB05p02161)  
 1235 [doi/abs/10.1029/JB084iB05p02161](https://doi.org/10.1029/JB084iB05p02161) doi: [https://doi.org/10.1029/](https://doi.org/10.1029/JB084iB05p02161)  
 1236 [JB084iB05p02161](https://doi.org/10.1029/JB084iB05p02161)
- 1237 Dieterich, J. H. (1979b). Modeling of rock friction: 2. simulation of preseismic  
 1238 slip. *Journal of Geophysical Research: Solid Earth*, *84*(B5), 2169–2175.  
 1239 Retrieved from [https://agupubs.onlinelibrary.wiley.com/doi/abs/](https://agupubs.onlinelibrary.wiley.com/doi/abs/10.1029/JB084iB05p02169)  
 1240 [10.1029/JB084iB05p02169](https://doi.org/10.1029/JB084iB05p02169) doi: <https://doi.org/10.1029/JB084iB05p02169>
- 1241 Dragert, H., Wang, K., & James, T. (2001). A silent slip event on the deeper casca-  
 1242 dia subduction interface. *Science*, *292*, 1525–1528.
- 1243 Dragert, H., Wang, K., & Rogers, G. (2004). Geodetic and seismic signatures of  
 1244 episodic tremor and slip in the northern Cascadia subduction zone. *Earth,*  
 1245 *Planets and Space*, *56*, 1143–1150.
- 1246 Dublanchet, P. (2019). Fluid driven shear cracks on a strengthening rate-and-state  
 1247 frictional fault. *Journal of the Mechanics and Physics of Solids*, *132*, 103672.  
 1248 doi: <https://doi.org/10.1016/j.jmps.2019.07.015>
- 1249 Dziewonski, A. M., & Anderson, D. L. (1981). Preliminary reference earth model.  
 1250 *Physics of the Earth and Planetary Interiors*, *25*(4), 297 - 356. Retrieved from  
 1251 <http://www.sciencedirect.com/science/article/pii/0031920181900467>  
 1252 doi: [https://doi.org/10.1016/0031-9201\(81\)90046-7](https://doi.org/10.1016/0031-9201(81)90046-7)
- 1253 Farge, G., Jaupart, C., & Shapiro, N. M. (2021). Episodicity and migration of low  
 1254 frequency earthquakes modeled with fast fluid pressure transients in the per-  
 1255 meable subduction interface. *Journal of Geophysical Research: Solid Earth*,  
 1256 *126*(9), e2021JB021894. doi: <https://doi.org/10.1029/2021JB021894>
- 1257 Frank, W. B., Radiguet, M., Rousset, B., Shapiro, N. M., Husker, A. L., Kos-  
 1258 toglodov, V., ... Campillo, M. (2015). Uncovering the geodetic signature

- 1259 of silent slip through repeating earthquakes. *Geophysical Research Letters*, *42*,  
1260 2774–2779. doi: 10.1002/2015GL063685
- 1261 Frank, W. B., Shapiro, N. M., Husker, A., Kostoglodov, V., Bhat, H. S., &  
1262 Campillo, M. (2015). Along-fault pore-pressure evolution during a slow-slip  
1263 event in guerrero, mexico. *Earth and Planetary Science Letters*, *413*, 135–143.  
1264 doi: <https://doi.org/10.1016/j.epsl.2014.12.051>
- 1265 Frank, W. B., Shapiro, N. M., Husker, A. L., Kostoglodov, V., Gusev, A. A., &  
1266 Campillo, M. (2016). The evolving interaction of low-frequency earth-  
1267 quakes during transient slip. *Science Advances*, *2*(4). Retrieved from  
1268 <https://advances.sciencemag.org/content/2/4/e1501616> doi:  
1269 10.1126/sciadv.1501616
- 1270 Frank, W. B., Shapiro, N. M., Husker, A. L., Kostoglodov, V., Romanenko, A.,  
1271 & Campillo, M. (2014). Using systematically characterized low-frequency  
1272 earthquakes as a fault probe in guerrero, mexico. *Journal of Geophysi-  
1273 cal Research: Solid Earth*, *119*(10), 7686–7700. Retrieved from [https://  
1274 agupubs.onlinelibrary.wiley.com/doi/abs/10.1002/2014JB011457](https://agupubs.onlinelibrary.wiley.com/doi/abs/10.1002/2014JB011457) doi:  
1275 <https://doi.org/10.1002/2014JB011457>
- 1276 Frederiksen, S., & Braun, J. (2001). Numerical modelling of strain localisation dur-  
1277 ing extension of the continental lithosphere. *Earth and Planetary Science Let-  
1278 ters*, *188*, 241–251.
- 1279 Gao, X., & Wang, K. (2017). Rheological separation of the megathrust seismogenic  
1280 zone and episodic tremor and slip. *Nature*, *543*, 416–419. doi: [https://doi.org/  
1281 10.1038/nature21389](https://doi.org/10.1038/nature21389)
- 1282 Gardner, J. K., & Knopoff, L. (1974, 10). Is the sequence of earthquakes in Southern  
1283 California, with aftershocks removed, Poissonian? *Bulletin of the Seismologi-  
1284 cal Society of America*, *64*(5), 1363–1367. Retrieved from [https://doi.org/10  
1285 .1785/BSSA0640051363](https://doi.org/10.1785/BSSA0640051363) doi: 10.1785/BSSA0640051363
- 1286 Geuzaine, C., & Remacle, J.-F. (2009). Gmsh: A 3-d finite element mesh gener-  
1287 ator with built-in pre- and post-processing facilities. *International Journal  
1288 for Numerical Methods in Engineering*, *79*(11), 1309–1331. Retrieved from  
1289 <https://onlinelibrary.wiley.com/doi/abs/10.1002/nme.2579> doi:  
1290 <https://doi.org/10.1002/nme.2579>
- 1291 Got, J.-L., Carrier, A., Marsan, D., Jouanne, F., Vogfjörd, K., & Vилlement, T.  
1292 (2017). An analysis of the non-linear magma-edifice coupling at grimsvötn  
1293 volcano (iceland). *Journal of Geophysical Research Solid Earth*, *122*. doi:  
1294 10.1002/2016JB012905
- 1295 Griffin, J. D., Stirling, M. W., & Wang, T. (2020). Periodicity and clustering  
1296 in the long-term earthquake record. *Geophysical Research Letters*, *47*(22),  
1297 e2020GL089272. Retrieved from [https://agupubs.onlinelibrary.wiley  
1298 .com/doi/abs/10.1029/2020GL089272](https://agupubs.onlinelibrary.wiley.com/doi/abs/10.1029/2020GL089272) (e2020GL089272 2020GL089272) doi:  
1299 <https://doi.org/10.1029/2020GL089272>
- 1300 Gutenberg, B., & Richter, C. F. (1949). *Seismicity of the earth and associated phe-  
1301 nomena*. Princeton NJ USA: Princeton University Press.
- 1302 Hamiel, Y., Liu, Y., Lyakhovskiy, V., Ben-Zion, Y., & Lockner, D. (2004). A  
1303 viscoelastic damage model with applications to stable and unstable frac-  
1304 turing. *Geophysical Journal International*, *159*, 1155–1165. doi: 10.1111/  
1305 j.1365-246X.2004.02452.x
- 1306 Handwerker, A. L., Rempel, A. W., Skarbek, R. M., Roering, J. J., & Hilley, G. E.  
1307 (2016). Rate-weakening friction characterizes both slow sliding and catas-  
1308 trophic failure of landslides. *Proceedings of the National Academy of Sciences*,  
1309 *113*(37), 10281–10286. Retrieved from [https://www.pnas.org/content/113/  
1310 37/10281](https://www.pnas.org/content/113/37/10281) doi: 10.1073/pnas.1607009113
- 1311 Hayman, N. W., & Lavier, L. L. (2014). The geologic record of deep episodic tremor  
1312 and slip. *Geology*, *42*(3), 195–198. Retrieved from [https://doi.org/10.1130/  
1313 G34990.1](https://doi.org/10.1130/G34990.1) doi: 10.1130/G34990.1

- 1314 Hetland, E. A., & Hager, B. H. (2005). Postseismic and interseismic displacements near a strike-slip fault: A two-dimensional theory for general linear viscoelastic rheologies. *Journal of Geophysical Research: Solid Earth*, *110*(B10). Retrieved from <https://agupubs.onlinelibrary.wiley.com/doi/abs/10.1029/2005JB003689> doi: <https://doi.org/10.1029/2005JB003689>
- 1315  
1316  
1317  
1318
- 1319 Hetland, E. A., & Hager, B. H. (2006, 07). The effects of rheological layering on post-seismic deformation. *Geophysical Journal International*, *166*(1), 277-292. Retrieved from <https://doi.org/10.1111/j.1365-246X.2006.02974.x> doi: [10.1111/j.1365-246X.2006.02974.x](https://doi.org/10.1111/j.1365-246X.2006.02974.x)
- 1320  
1321  
1322
- 1323 Hirono, T., Kaneki, S., Ishikawa, T., Kameda, J., Tonoike, N., Ito, A., & Miyazaki, Y. (2020). Generation of sintered fault rock and its implications for earthquake energetics and fault healing. *Communications Earth & Environment*, *1*(1), 3. Retrieved from <https://doi.org/10.1038/s43247-020-0004-z> doi: [10.1038/s43247-020-0004-z](https://doi.org/10.1038/s43247-020-0004-z)
- 1324  
1325  
1326  
1327
- 1328 Hunfeld, L. B., Chen, J., Hol, S., Niemeijer, A. R., & Spiers, C. J. (2020). Healing behavior of simulated fault gouges from the groningen gas field and implications for induced fault reactivation. *Journal of Geophysical Research: Solid Earth*, *125*(7), e2019JB018790. Retrieved from <https://agupubs.onlinelibrary.wiley.com/doi/abs/10.1029/2019JB018790> (e2019JB018790 2019JB018790) doi: <https://doi.org/10.1029/2019JB018790>
- 1329  
1330  
1331  
1332  
1333
- 1334 Idehara, K., Yabe, S., & Ide, S. (2014, December). Regional and global variations in the temporal clustering of tectonic tremor activity. *Earth, Planets and Space*, *66*(1), 66. doi: [10.1186/1880-5981-66-66](https://doi.org/10.1186/1880-5981-66-66)
- 1335  
1336
- 1337 Ingleby, T., & Wright, T. J. (2017). Omori-like decay of postseismic velocities following continental earthquakes. *Geophysical Research Letters*, *44*(7), 3119-3130. Retrieved from <https://agupubs.onlinelibrary.wiley.com/doi/abs/10.1002/2017GL072865> doi: <https://doi.org/10.1002/2017GL072865>
- 1338  
1339  
1340
- 1341 Jaeger, J. C., & Cook, N. G. W. (1979). *Fundamentals of rock mechanics*. Cambridge UK: Chapman and Hall.
- 1342
- 1343 Kachanov, L. M. (1958). On rupture time under condition of creep. *Izvestia Akademi Nauk SSSR, Otd. Tekhn. Nauk*, *8*, 26-31. ((in Russian))
- 1344
- 1345 Kostoglodov, V., Singh, S. K., Santiago, J. A., Franco, S. I., Larson, K. M., Lowry, A. R., & Bilham, R. (2003). A large silent earthquake in the guerrero seismic gap, mexico. *Geophysical Research Letters*, *30*(15), 1807. doi: [10.1029/2003GL017219](https://doi.org/10.1029/2003GL017219)
- 1346  
1347  
1348
- 1349 Lacroix, P., Perfettini, H., Taïpe, E., & Guillier, B. (2014). Coseismic and post-seismic motion of a landslide: Observations, modeling, and analogy with tectonic faults. *Geophysical Research Letters*, *41*(19), 6676-6680. Retrieved from <https://agupubs.onlinelibrary.wiley.com/doi/abs/10.1002/2014GL061170> doi: <https://doi.org/10.1002/2014GL061170>
- 1350  
1351  
1352  
1353
- 1354 Li, Y.-G., & Vidale, J. E. (2001). Healing of the shallow fault zone from 1994-1998 after the 1992 m7.5 landers, california, earthquake. *Geophysical Research Letters*, *28*(15), 2999-3002. Retrieved from <https://agupubs.onlinelibrary.wiley.com/doi/abs/10.1029/2001GL012922> doi: <https://doi.org/10.1029/2001GL012922>
- 1355  
1356  
1357  
1358
- 1359 Li, Y.-G., Vidale, J. E., Aki, K., Xu, F., & Burdette, T. (1998). Evidence of shallow fault zone strengthening after the 1992 m7.5 landers, california, earthquake. *Science*, *279*(5348), 217-219. Retrieved from <https://www.science.org/doi/abs/10.1126/science.279.5348.217> doi: [10.1126/science.279.5348.217](https://doi.org/10.1126/science.279.5348.217)
- 1360  
1361  
1362  
1363
- 1364 Liu, Y., & Rice, J. R. (2005). Aseismic slip transients emerge spontaneously in three-dimensional rate and state modeling of subduction earthquake sequences. *Journal of Geophysical Research: Solid Earth*, *110*(B8). Retrieved from <https://agupubs.onlinelibrary.wiley.com/doi/abs/10.1029/2004JB003424> doi: <https://doi.org/10.1029/2004JB003424>
- 1365  
1366  
1367  
1368

- 1369 Liu, Y., & Rice, J. R. (2007). Spontaneous and triggered aseismic deformation  
1370 transients in a subduction fault model. *Journal of Geophysical Research:*  
1371 *Solid Earth*, *112*(B9). Retrieved from <https://agupubs.onlinelibrary>  
1372 [.wiley.com/doi/abs/10.1029/2007JB004930](https://agupubs.onlinelibrary.wiley.com/doi/abs/10.1029/2007JB004930) doi: <https://doi.org/10.1029/>  
1373 [2007JB004930](https://doi.org/10.1029/2007JB004930)
- 1374 Luo, Y., & Liu, Z. (2019). Rate-and-state model casts new insight into episodic  
1375 tremor and slow-slip variability in cascadia. *Geophysical Research Letters*,  
1376 *46*(12), 6352-6362. doi: <https://doi.org/10.1029/2019GL082694>
- 1377 Luo, Y., & Liu, Z. (2021). Fault zone heterogeneities explain depth-dependent pat-  
1378 tern and evolution of slow earthquakes in cascadia. *Nature Communications*,  
1379 *12*(1), 1959. doi: [10.1038/s41467-021-22232-x](https://doi.org/10.1038/s41467-021-22232-x)
- 1380 Lyakhovskiy, V., Ben-Zion, Y., & Agnon, A. (1997). Distributed damage, faulting  
1381 and friction. *Journal of Geophysical Research*, *102*(B12), 27635-27649.
- 1382 Lyakhovskiy, V., Ben-Zion, Y., & Agnon, A. (2001). Earthquake cycle, fault zones,  
1383 and seismicity patterns in a rheologically layered lithosphere. *Journal of Geo-*  
1384 *physical Research: Solid Earth*, *106*(B3), 4103-4120. Retrieved from [https://](https://agupubs.onlinelibrary.wiley.com/doi/abs/10.1029/2000JB900218)  
1385 [agupubs.onlinelibrary.wiley.com/doi/abs/10.1029/2000JB900218](https://agupubs.onlinelibrary.wiley.com/doi/abs/10.1029/2000JB900218) doi:  
1386 <https://doi.org/10.1029/2000JB900218>
- 1387 Lyakhovskiy, V., Reches, Z., Weinberger, R., & Scott, T. E. (1997). Non-linear elas-  
1388 tic behaviour of damaged rocks. *Geophysical Journal International*, *130*(1),  
1389 157-166. Retrieved from [https://onlinelibrary.wiley.com/doi/abs/](https://onlinelibrary.wiley.com/doi/abs/10.1111/j.1365-246X.1997.tb00995.x)  
1390 [10.1111/j.1365-246X.1997.tb00995.x](https://onlinelibrary.wiley.com/doi/abs/10.1111/j.1365-246X.1997.tb00995.x) doi: <https://doi.org/10.1111/>  
1391 [j.1365-246X.1997.tb00995.x](https://doi.org/10.1111/j.1365-246X.1997.tb00995.x)
- 1392 McLaskey, G. C., Thomas, A. M., Glaser, S. D., & Nadeau, R. M. (2012).  
1393 Fault healing promotes high-frequency earthquakes in laboratory experi-  
1394 ments and on natural faults. *Nature*, *491*(7422), 101-104. Retrieved from  
1395 <https://doi.org/10.1038/nature11512> doi: [10.1038/nature11512](https://doi.org/10.1038/nature11512)
- 1396 Michael, A. J. (2011). Random variability explains apparent global clustering  
1397 of large earthquakes. *Geophysical Research Letters*, *38*(21). Retrieved  
1398 from [https://agupubs.onlinelibrary.wiley.com/doi/abs/10.1029/](https://agupubs.onlinelibrary.wiley.com/doi/abs/10.1029/2011GL049443)  
1399 [2011GL049443](https://agupubs.onlinelibrary.wiley.com/doi/abs/10.1029/2011GL049443) doi: <https://doi.org/10.1029/2011GL049443>
- 1400 Nur, A., & Mavko, G. (1974). Postseismic viscoelastic rebound. *Science*, *183*(4121),  
1401 204-206. Retrieved from [https://www.science.org/doi/abs/10.1126/](https://www.science.org/doi/abs/10.1126/science.183.4121.204)  
1402 [science.183.4121.204](https://www.science.org/doi/abs/10.1126/science.183.4121.204) doi: [10.1126/science.183.4121.204](https://doi.org/10.1126/science.183.4121.204)
- 1403 Obara, K. (2002). Nonvolcanic deep tremor associated with subduction in south-  
1404 west japan. *Science*, *296*(5573), 1679-1681. Retrieved from [https://science](https://science.sciencemag.org/content/296/5573/1679)  
1405 [.sciencemag.org/content/296/5573/1679](https://science.sciencemag.org/content/296/5573/1679) doi: [10.1126/science.1070378](https://doi.org/10.1126/science.1070378)
- 1406 Obara, K., & Kato, A. (2016). Connecting slow earthquakes to huge earthquakes.  
1407 *Science*, *353*(6296), 253-257. Retrieved from [https://science.sciencemag](https://science.sciencemag.org/content/353/6296/253)  
1408 [.org/content/353/6296/253](https://science.sciencemag.org/content/353/6296/253) doi: [10.1126/science.aaf1512](https://doi.org/10.1126/science.aaf1512)
- 1409 Ólason, E., Rampal, P., & Dansereau, V. (2021). On the statistical properties of sea-  
1410 ice lead fraction and heat fluxes in the arctic. *The Cryosphere*, *15*(2), 1053-  
1411 1064. Retrieved from <https://tc.copernicus.org/articles/15/1053/2021/>  
1412 doi: [10.5194/tc-15-1053-2021](https://doi.org/10.5194/tc-15-1053-2021)
- 1413 Omori, F. (1894). On the aftershocks of earthquakes. *Journal of the College of Sci-*  
1414 *ence, Imperial University of Tokyo*, *7*, 111-120.
- 1415 Parisio, F., Vinciguerra, S., Kolditz, O., & Nagel, T. (2019). The brittle-  
1416 ductile transition in active volcanoes. *Scientific Reports*, *9*(1), 143. Re-  
1417 trieved from <https://doi.org/10.1038/s41598-018-36505-x> doi:  
1418 [10.1038/s41598-018-36505-x](https://doi.org/10.1038/s41598-018-36505-x)
- 1419 Payero, J. S., Kostoglodov, V., Shapiro, N., Mikumo, T., Iglesias, A., Pérez-Campos,  
1420 X., & Clayton, R. W. (2008). Nonvolcanic tremor observed in the mexi-  
1421 can subduction zone. *Geophysical Research Letters*, *35*(7), L07305. doi:  
1422 [10.1029/2007GL032877](https://doi.org/10.1029/2007GL032877)
- 1423 Peacock, S. M. (2009). Thermal and metamorphic environment of subduction

- 1424 zone episodic tremor and slip. *Journal of Geophysical Research: Solid Earth*,  
 1425 114(B8). Retrieved from [https://agupubs.onlinelibrary.wiley.com/doi/](https://agupubs.onlinelibrary.wiley.com/doi/abs/10.1029/2008JB005978)  
 1426 [abs/10.1029/2008JB005978](https://agupubs.onlinelibrary.wiley.com/doi/abs/10.1029/2008JB005978) doi: <https://doi.org/10.1029/2008JB005978>
- 1427 Peng, Z., & Gomberg, J. (2010). An integrated perspective of the continuum be-  
 1428 tween earthquakes and slow-slip phenomena. *Nature Geoscience*, 3, 599–607.  
 1429 doi: <https://doi.org/10.1038/ngeo940>
- 1430 Perfettini, H., & Avouac, J.-P. (2004). Postseismic relaxation driven by brittle  
 1431 creep: A possible mechanism to reconcile geodetic measurements and  
 1432 the decay rate of aftershocks, application to the chi-chi earthquake, tai-  
 1433 wan. *Journal of Geophysical Research: Solid Earth*, 109(B2). doi:  
 1434 <https://doi.org/10.1029/2003JB002488>
- 1435 Periollat, A., Radiguet, M., Weiss, J., Twardzik, C., Amitrano, D., Cotte, N., ...  
 1436 Socquet, A. (2022). Transient brittle creep mechanism explains early post-  
 1437 seismic phase of the 2011 tohoku-oki megathrust earthquake: Observations by  
 1438 high-rate gps solutions. *Journal of Geophysical Research: Solid Earth*, 127(8),  
 1439 e2022JB024005. doi: <https://doi.org/10.1029/2022JB024005>
- 1440 Poiata, N., Vilotte, J.-P., Shapiro, N. M., Supino, M., & Obara, K. (2021). Com-  
 1441 plexity of deep low-frequency earthquake activity in shikoku (japan) imaged  
 1442 from the analysis of continuous seismic data. *Journal of Geophysical Re-*  
 1443 *search: Solid Earth*, 126(11), e2021JB022138. doi: [https://doi.org/10.1029/](https://doi.org/10.1029/2021JB022138)  
 1444 [2021JB022138](https://doi.org/10.1029/2021JB022138)
- 1445 Poli, P. (2017). Creep and slip: Seismic precursors to the nuugaatsiaq landslide  
 1446 (greenland). *Geophysical Research Letters*, 44(17), 8832–8836. Retrieved  
 1447 from [https://agupubs.onlinelibrary.wiley.com/doi/abs/10.1002/](https://agupubs.onlinelibrary.wiley.com/doi/abs/10.1002/2017GL075039)  
 1448 [2017GL075039](https://agupubs.onlinelibrary.wiley.com/doi/abs/10.1002/2017GL075039) doi: <https://doi.org/10.1002/2017GL075039>
- 1449 Pollitz, F. F. (2003). Transient rheology of the uppermost mantle beneath the  
 1450 mojave desert, california. *Earth and Planetary Science Letters*, 215(1), 89 -  
 1451 104. Retrieved from [http://www.sciencedirect.com/science/article/pii/](http://www.sciencedirect.com/science/article/pii/S0012821X03004321)  
 1452 [S0012821X03004321](http://www.sciencedirect.com/science/article/pii/S0012821X03004321) doi: [https://doi.org/10.1016/S0012-821X\(03\)00432-1](https://doi.org/10.1016/S0012-821X(03)00432-1)
- 1453 Pollitz, F. F. (2005). Transient rheology of the upper mantle beneath central  
 1454 alaska inferred from the crustal velocity field following the 2002 denali earth-  
 1455 quake. *Journal of Geophysical Research: Solid Earth*, 110(B8). Retrieved  
 1456 from [https://agupubs.onlinelibrary.wiley.com/doi/abs/10.1029/](https://agupubs.onlinelibrary.wiley.com/doi/abs/10.1029/2005JB003672)  
 1457 [2005JB003672](https://agupubs.onlinelibrary.wiley.com/doi/abs/10.1029/2005JB003672) doi: <https://doi.org/10.1029/2005JB003672>
- 1458 Pollitz, F. F., Wicks, C., & Thatcher, W. (2001). Mantle flow beneath a  
 1459 continental strike-slip fault: Postseismic deformation after the 1999 hec-  
 1460 tor mine earthquake. *Science*, 293(5536), 1814–1818. Retrieved from  
 1461 <https://www.science.org/doi/abs/10.1126/science.1061361> doi:  
 1462 [10.1126/science.1061361](https://www.science.org/doi/abs/10.1126/science.1061361)
- 1463 Popov, A., & Sobolev, S. V. (2008). Slim3d: A tool for three-dimensional ther-  
 1464 momechanical modeling of lithospheric deformation with elasto-visco-plastic  
 1465 rheology. *Physics of the Earth and Planetary Interiors*, 171(1), 55–75. Re-  
 1466 trieved from [https://www.sciencedirect.com/science/article/pii/](https://www.sciencedirect.com/science/article/pii/S003192010800054X)  
 1467 [S003192010800054X](https://www.sciencedirect.com/science/article/pii/S003192010800054X) (Recent Advances in Computational Geodynam-  
 1468 ics: Theory, Numerics and Applications) doi: [https://doi.org/10.1016/](https://doi.org/10.1016/j.pepi.2008.03.007)  
 1469 [j.pepi.2008.03.007](https://doi.org/10.1016/j.pepi.2008.03.007)
- 1470 Radiguet, M., Cotton, F., Vergnolle, M., Campillo, M., Walpersdorf, A., Cotte, N.,  
 1471 & Kostoglodov, V. (2012). Slow slip events and strain accumulation in the  
 1472 guerrero gap, mexico. *Journal of Geophysical Research: Solid Earth*, 117(B4).  
 1473 Retrieved from [https://agupubs.onlinelibrary.wiley.com/doi/abs/](https://agupubs.onlinelibrary.wiley.com/doi/abs/10.1029/2011JB008801)  
 1474 [10.1029/2011JB008801](https://agupubs.onlinelibrary.wiley.com/doi/abs/10.1029/2011JB008801) doi: <https://doi.org/10.1029/2011JB008801>
- 1475 Radiguet, M., Perfettini, H., Cotte, N., & et al. (2016). Triggering of the 2014 Mw  
 1476 7.3 Papanoa earthquake by a slow slip event in guerrero, mexico. *Nature Geo-*  
 1477 *science*, 9, 829–833. doi: <https://doi.org/10.1038/ngeo2817>
- 1478 Rampal, P., Dansereau, V., Olason, E., Bouillon, S., Williams, T., Korosov, A.,

- 1479 & Samaké, A. (2019). On the multi-fractal scaling properties of sea  
 1480 ice deformation. *The Cryosphere*, *13*(9), 2457–2474. Retrieved from  
 1481 <https://tc.copernicus.org/articles/13/2457/2019/> doi: 10.5194/  
 1482 tc-13-2457-2019
- 1483 Renard, F., Gratier, J.-P., & Jamtveit, B. (2000). Kinetics of crack-sealing, in-  
 1484 tergranular pressure solution, and compaction around active faults. *Jour-  
 1485 nal of Structural Geology*, *22*(10), 1395–1407. Retrieved from [https://  
 1486 www.sciencedirect.com/science/article/pii/S019181410000064X](https://www.sciencedirect.com/science/article/pii/S019181410000064X) doi:  
 1487 [https://doi.org/10.1016/S0191-8141\(00\)00064-X](https://doi.org/10.1016/S0191-8141(00)00064-X)
- 1488 Rivet, D., Campillo, M., Shapiro, N. M., Cruz-Atienza, V., Radiguet, M., Cotte, N.,  
 1489 & Kostoglodov, V. (2011). Seismic evidence of nonlinear crustal deforma-  
 1490 tion during a large slow slip event in Mexico. *Geophysical Research Letters*,  
 1491 *38*(8). Retrieved from [https://agupubs.onlinelibrary.wiley.com/doi/  
 1492 abs/10.1029/2011GL047151](https://agupubs.onlinelibrary.wiley.com/doi/abs/10.1029/2011GL047151) doi: <https://doi.org/10.1029/2011GL047151>
- 1493 Rogers, G., & Dragert, H. (2003). Episodic tremor and slip on the Cascadia subduc-  
 1494 tion zone: The chatter of silent slip. *Science*, *300*(5627), 1942–1943. Retrieved  
 1495 from <http://www.jstor.org/stable/3834528>
- 1496 Royden, L. H., Burchfiel, B. C., King, R. W., Wang, E., Chen, Z., Shen, F., & Liu,  
 1497 Y. (1997). Surface Deformation and Lower Crustal Flow in Eastern Tibet.  
 1498 *Science*, *276*(5313), 788–790. doi: 10.1126/science.276.5313.788
- 1499 Ruina, A. (1983). Slip instability and state variable friction laws. *Journal  
 1500 of Geophysical Research: Solid Earth*, *88*(B12), 10359–10370. Retrieved  
 1501 from [https://agupubs.onlinelibrary.wiley.com/doi/abs/10.1029/  
 1502 JB088iB12p10359](https://agupubs.onlinelibrary.wiley.com/doi/abs/10.1029/JB088iB12p10359) doi: <https://doi.org/10.1029/JB088iB12p10359>
- 1503 Saramito, P. (2020). *Efficient c++ finite element computing with rheolef*. CNRS-  
 1504 CCSD ed. (<http://hal.archives-ouvertes.fr/cel-00573970>)
- 1505 Savage, J., Svarc, J., & Yu, S.-B. (2005). Postseismic relaxation and transient creep.  
 1506 *Journal of Geophysical Research: Solid Earth*, *110*(B11).
- 1507 Scholz, C. H. (1998). Earthquakes and friction laws. *Nature*, *391*, 37–42.
- 1508 Segall, P., & Bradley, A. M. (2012). The Role of Thermal Pressurization and Di-  
 1509 latancy in Controlling the Rate of Fault Slip. *Journal of Applied Mechanics*,  
 1510 *79*(3). Retrieved from <https://doi.org/10.1115/1.4005896> (031013) doi:  
 1511 10.1115/1.4005896
- 1512 Segall, P., & Rice, J. R. (1995). Dilatancy, compaction, and slip instability of a  
 1513 fluid-infiltrated fault. *Journal of Geophysical Research: Solid Earth*, *100*(B11),  
 1514 22155–22171. Retrieved from [https://agupubs.onlinelibrary.wiley.com/  
 1515 doi/abs/10.1029/95JB02403](https://agupubs.onlinelibrary.wiley.com/doi/abs/10.1029/95JB02403) doi: <https://doi.org/10.1029/95JB02403>
- 1516 Seydoux, L., Balestrieri, R., Poli, P., de Hoop, M., Campillo, M., & Baraniuk, R.  
 1517 (2020). Clustering earthquake signals and background noises in continuous  
 1518 seismic data with unsupervised deep learning. *Nature Communications*, *11*(1),  
 1519 3972. Retrieved from <https://doi.org/10.1038/s41467-020-17841-x> doi:  
 1520 10.1038/s41467-020-17841-x
- 1521 Shapiro, N. M., Campillo, M., Kaminski, E., Vilotte, J.-P., & Jaupart, C. (2018).  
 1522 Low-frequency earthquakes and pore pressure transients in subduction zones.  
 1523 *Geophysical Research Letters*, *45*(20), 11,083–11,094. doi: [https://doi.org/  
 1524 10.1029/2018GL079893](https://doi.org/10.1029/2018GL079893)
- 1525 Shcherbakov, R., Turcotte, D. L., & Rundle, J. B. (2005). Aftershock statistics. *Pure  
 1526 and applied geophysics*, *162*(6), 1051–1076.
- 1527 Shelly, D. R., Beroza, G. C., Ide, S., & Nakamura, S. (2006). Low-frequency earth-  
 1528 quakes in Shikoku, Japan, and their relationship to episodic tremor and slip.  
 1529 *Nature*, *442*(7099), 188–191. doi: 10.1038/nature04931
- 1530 Sibson, R. H. (1992). Implications of fault-valve behaviour for rupture nucle-  
 1531 ation and recurrence. *Tectonophysics*, *211*(1), 283–293. Retrieved from  
 1532 <http://www.sciencedirect.com/science/article/pii/004019519290065E>  
 1533 doi: [https://doi.org/10.1016/0040-1951\(92\)90065-E](https://doi.org/10.1016/0040-1951(92)90065-E)

- 1534 Siravo, G., Faccenna, C., G erault, M., Becker, T. W., Fellin, M. G., Herman, F., &  
1535 Molin, P. (2019). Slab flattening and the rise of the eastern cordillera, colombia.  
1536 *Earth and Planetary Science Letters*, *512*, 100 - 110. Retrieved from  
1537 <http://www.sciencedirect.com/science/article/pii/S0012821X19300925>  
1538 doi: <https://doi.org/10.1016/j.epsl.2019.02.002>
- 1539 Sun, T., & Wang, K. (2015). Viscoelastic relaxation following subduction earth-  
1540 quakes and its effects on afterslip determination. *Journal of Geophysi-  
1541 cal Research: Solid Earth*, *120*(2), 1329-1344. Retrieved from [https://  
1542 agupubs.onlinelibrary.wiley.com/doi/abs/10.1002/2014JB011707](https://agupubs.onlinelibrary.wiley.com/doi/abs/10.1002/2014JB011707) doi:  
1543 <https://doi.org/10.1002/2014JB011707>
- 1544 Tang, C. (1997). Numerical simulation of progressive rock failure and associated  
1545 seismicity. *International Journal of Rock Mechanics and Mining Sciences*,  
1546 *34*(2), 249-261.
- 1547 Turcotte, D. L. (1992). *Fractals and chaos in geology and geophysics*. New York, NY,  
1548 USA: Cambridge University Press.
- 1549 Turcotte, D. L., Newman, W. I., & Shcherbakov, R. (2003). Micro and macroscopic  
1550 models of rock fracture. *Geophysical Journal International*, *152*, 718-728.
- 1551 van den Ende, M., Chen, J., Ampuero, J.-P., & Niemeijer, A. (2018). A comparison  
1552 between rate-and-state friction and microphysical models, based on numeri-  
1553 cal simulations of fault slip. *Tectonophysics*, *733*, 273 - 295. Retrieved from  
1554 <http://www.sciencedirect.com/science/article/pii/S0040195117305024>  
1555 (Physics of Earthquake Rupture Propagation) doi: [https://doi.org/10.1016/  
1556 j.tecto.2017.11.040](https://doi.org/10.1016/j.tecto.2017.11.040)
- 1557 Wang, K., Hu, Y., & He, J. (2012). Deformation cycles of subduction earthquakes  
1558 in a viscoelastic Earth. *Nature*, *484*, 327-332. doi: [https://doi.org/10.1038/  
1559 nature11032](https://doi.org/10.1038/nature11032)
- 1560 Wang, Q.-Y., Campillo, M., Brenguier, F., Lecointre, A., Takeda, T., & Hashima, A.  
1561 (2019). Evidence of changes of seismic properties in the entire crust beneath  
1562 japan after the mw 9.0, 2011 tohoku-oki earthquake. *Journal of Geophys-  
1563 ical Research: Solid Earth*, *124*(8), 8924-8941. Retrieved from [https://  
1564 agupubs.onlinelibrary.wiley.com/doi/abs/10.1029/2019JB017803](https://agupubs.onlinelibrary.wiley.com/doi/abs/10.1029/2019JB017803) doi:  
1565 <https://doi.org/10.1029/2019JB017803>
- 1566 Wech, A. G., & Creager, K. C. (2011). A continuum of stress, strength and slip in  
1567 the cascadia subduction zone. *Nature Geoscience*, *4*(9), 624-628. doi: 10.1038/  
1568 ngeo1215
- 1569 Weiss, J., & Dansereau, V. (2017). Linking scales in sea ice mechanics.  
1570 *Philosophical Transaction Royal Society A: Mathematical, Physical and  
1571 Engineering Sciences*, *375*(2086), 20150352. Retrieved from [http://  
1572 rsta.royalsocietypublishing.org/content/375/2086/20150352](http://rsta.royalsocietypublishing.org/content/375/2086/20150352) doi:  
1573 10.1098/rsta.2015.0352
- 1574 Williams, R. T., Davis, J. R., & Goodwin, L. B. (2019). Do large earthquakes oc-  
1575 cur at regular intervals through time? a perspective from the geologic record.  
1576 *Geophysical Research Letters*, *46*(14), 8074-8081. Retrieved from [https://  
1577 agupubs.onlinelibrary.wiley.com/doi/abs/10.1029/2019GL083291](https://agupubs.onlinelibrary.wiley.com/doi/abs/10.1029/2019GL083291) doi:  
1578 <https://doi.org/10.1029/2019GL083291>
- 1579 Williams, R. T., Mozley, P. S., Sharp, W. D., & Goodwin, L. B. (2019). U-th dating  
1580 of syntectonic calcite veins reveals the dynamic nature of fracture cementa-  
1581 tion and healing in faults. *Geophysical Research Letters*, *46*(22), 12900-12908.  
1582 Retrieved from [https://agupubs.onlinelibrary.wiley.com/doi/abs/  
1583 10.1029/2019GL085403](https://agupubs.onlinelibrary.wiley.com/doi/abs/10.1029/2019GL085403) doi: <https://doi.org/10.1029/2019GL085403>
- 1584 Williams, T., Korosov, A., Rampal, P., & Olason, E. (2019). Presentation and eval-  
1585 uation of the Arctic sea ice forecasting system neXtSIM-F. *The Cryosphere  
1586 Discussions*, *2019*, 1-31. Retrieved from [https://tc.copernicus.org/  
1587 preprints/tc-2019-154/](https://tc.copernicus.org/preprints/tc-2019-154/) doi: 10.5194/tc-2019-154

1                   **Modeling Multi-Scale Deformation Cycles in**  
2                   **Subduction Zones with a Continuum**  
3                   **Visco-Elastic-Brittle Framework**

4                   **Véronique Dansereau<sup>1</sup>, Nikolai Shapiro<sup>1</sup>, Michel Campillo<sup>1</sup>, Jérôme Weiss<sup>1</sup>**

5                   <sup>1</sup>Institut des Sciences de la Terre, Université Grenoble Alpes, CNRS (5275), Grenoble, France

6                   **Key Points:**

- 7                   • We present a continuum model for the deformation of faults in which the mechan-  
8                   ical strength vary continuously as a function of the damage.  
9                   • The model's numerical scheme allows covering the very short and very long time  
10                  scale processes involved in the slow earthquake phenomenon.  
11                  • The model reproduces different types of transient deformations, akin to slow and  
12                  classical earthquakes in subduction zones.

---

Corresponding author: Véronique Dansereau, [veronique.dansereau@univ-grenoble-alpes.fr](mailto:veronique.dansereau@univ-grenoble-alpes.fr)

## Abstract

The overwhelming amount of seismic, geodesic and in-situ observations accumulated over the last 30 years clearly indicate that, from a mechanical point of view, faults should be considered as both damageable elastic solids in which highly localized features emerge as a result of very short-term brittle processes and materials experiencing ductile strains distributed in large volumes and over long time scales. The interplay of both deformation mechanisms, brittle and ductile, give rise to transient phenomena associating slow slip and tremors, known as slow earthquakes, which dissipate a significant amount of stress in the fault system. The physically-based numerical models developed to improve our comprehension of the mechanical and dynamical behaviour of faults must therefore have the capacity to treat simultaneously both deformation mechanisms and to cover a wide range of time scales in a numerically efficient manner. This capability is essential, both for simulating accurately their deformation cycles and for improving our interpretation of the available observations.

In this paper, we present a numerically efficient visco-elasto-brittle numerical framework that can simulate transient deformations akin to that observed in the context of subduction zones, over the wide range of time scales relevant for slow earthquakes. We implement the model in idealized simple shear simulations and explore the sensitivity of its behaviour to the value of its main mechanical parameters.

## Plain Language Summary

The outer part of the Earth, called the lithosphere, is a complex object that deforms both in a solid and a fluid manner. Where tectonic plates meet, such as in fault zones, this duality gives rise to a variety of phenomena. The solid behaviour is associated with earthquakes and very sudden slip movements of the fault that we feel at the surface. The fluid behaviour translates into a slow and steady slip at depth. In between, the mixed solid-fluid behaviour results in progressive accelerations and decelerations of the fault slip accompanied with very weak quakes, which are called *slow earthquakes*. These slow earthquakes modulate the deformation cycle of faults and most probably impact the occurrence of "real", or *classical*, earthquakes. It is therefore important to account for them in numerical models that aim to help us understand this cycle better. In this paper we present a model of the deformation of fault zones that we have developed with the particular goal of representing slow earthquakes and that allows the lithosphere to behave sometimes like a solid, sometimes like a fluid.

## 1 Introduction

Earth's materials are known to exhibit a variety of deformation mechanisms depending on temperature, pressure and loading conditions as well as on the time and spatial scales at which they are observed (e.g., Burov, 2011). In the most dynamic parts of the Earth's lithosphere, such as plate boundaries and fault zones, volcanic systems and landslides, the interplay between different mechanisms can result in a strong strain localization and a complex temporal behaviour. The slow deformation occurring over geological time scales can indeed be suddenly accelerated and give rise to catastrophic events (earthquakes, eruptions, landslides) that release huge amounts of energy in a very short time.

Historically, the deformation of the lithosphere has been studied either at the short time scales (seconds to minutes) of these catastrophic events or at the very large time scales (years to millions of years) of plate tectonic motion. However, the technological progresses in observational systems over the last 30 years has brought about a revolution in the comprehension of its dynamical behaviour, by allowing to explore the time scales in between. Global Positioning System (GPS), radar interferometry (Synthetic Aper-

62 ture Radar, InSAR) and satellite gravimetry data have indeed driven a huge leap for-  
63 ward in terms of measuring the deformation of the Earth surface continuously in time  
64 and space and at high resolution. These new geodetic observations have been accompa-  
65 nished by rapid deployments of dense seismic networks and by the emergence of novel meth-  
66 ods of analysis of continuous seismic data that allow exploring deformation mechanisms  
67 over a significantly wider range of time scales.

68 In the case of earthquakes, the occurrence of co-seismic rupture processes that re-  
69 distribute Coulomb stresses over short time scales (on the order of seconds) and the as-  
70 sociated scaling properties have been established for a long time (Omori, 1894; Guten-  
71 berg & Richter, 1949; Turcotte, 1992). However, the recent advances in the observational  
72 systems and data analysis methods have profoundly modified our vision of how plate tec-  
73 tonic motions are accommodated and how stresses are dissipated along faults. In par-  
74 ticular, the combination of high resolution geodetic and seismic data has resulted in im-  
75 proved tracking of co-, post- and inter-seismic deformation patterns (e.g., K. Wang et  
76 al., 2012) and in the discovery of new types of transient phenomena designated as “slow  
77 earthquakes”. These slow earthquakes, associated because of their triggering depth with  
78 the so-called brittle-ductile transition comprised between the brittle, seismic zone near  
79 the surface and the ductile, aseismic zone below (e.g., Dragert et al., 2004; Peng & Gomberg,  
80 2010; Obara & Kato, 2016, and many others), combine periodic accelerations of the fault  
81 slip with weak seismic radiations known as tectonic tremors (e.g., Dragert et al., 2001;  
82 Obara, 2002; Peng & Gomberg, 2010). Analyses based on the cross-correlations of am-  
83 bient seismic noise have demonstrated that the transient deformations accompanying both  
84 slow and major earthquakes are associated with changes in elastic properties of the ma-  
85 terial in the vicinity of the fault, reminiscent of damaging processes and of a non-elastic,  
86 or at least nonlinear elastic behaviour (e.g., Brenguier et al., 2008; Rivet et al., 2011; Q.-  
87 Y. Wang et al., 2019). Seismic data (e.g., Audet et al., 2009), along with other sources  
88 such as tomographic imagery (Shelly et al., 2006) and the observation of exhumed sub-  
89 duction zones (Angiboust et al., 2015), have also allowed identifying fluids as another  
90 major player in the transient deformation of faults. In the context of slow earthquakes  
91 in particular, the increased pore-pressure from fluids trapped in the fault zone and as-  
92 sociated pore-pressure variations and diffusion are indeed believed to partially control  
93 the seismic and slow slip activity via the weakening and fracturing of the host rock, the  
94 local reduction of the effective stress and friction along the shearing plane and the trig-  
95 gering and migration of tremors (e.g., Brown et al., 2005; Frank, Shapiro, et al., 2015;  
96 Shapiro et al., 2018; Cruz-Atienza et al., 2018; Dublanchet, 2019; Luo & Liu, 2019, 2021,  
97 and many others).

## 98 1.1 Existing Modelling Approaches

99 The direct modelling approaches that exist to model the deformation of the Earth’s  
100 lithosphere and faults in particular can be divided in several categories.

101 The first includes continuum frameworks based on a fluid mechanics approach, namely  
102 viscous, visco-elastic, visco-plastic or elasto-visco-plastic models. Such models have been  
103 developed to represent the diffuse, ductile and potentially large deformations associated  
104 with plate tectonics motion, for instance the formation of mountain ranges and conti-  
105 nental rifts (e.g., Royden et al., 1997; Frederiksen & Braun, 2001; Popov & Sobolev, 2008).  
106 They can reproduce strain localization by including strain-weakening mechanisms, such  
107 as a non-linear dependence of the viscous strain rate on the stress and thermo-mechanical  
108 feedbacks. However, their applications are restricted to ductile deformations on geolog-  
109 ical time scales. In the context of faults, visco-elastic models of the Maxwell or Burg-  
110 ers type (see figure 1) have also been often used to represent the mechanical behaviour  
111 of the combined Earth’s crust and mantle system (e.g. Nur & Mavko, 1974; Pollitz et  
112 al., 2001; Pollitz, 2003, 2005; Hetland & Hager, 2005, 2006; K. Wang et al., 2012; Sun  
113 & Wang, 2015). In such frameworks, the Maxwell component represents the lithosphere,

114 which can elastically transmit stresses over short time scales, while relaxing stresses in  
 115 an exponential manner over very long time scales. The Kelvin component is added to  
 116 represents the more ductile asthenosphere, which hosts mantle convection and is thought  
 117 to cause a delayed elastic response, measurable in the reversal of surface velocities after  
 118 after a major earthquake (e.g., Sun & Wang, 2015). However, with constant mechanical  
 119 parameters (elastic moduli and viscosities), these models cannot by themselves account  
 120 for the rheological stratification of fault zones, nor for the presence of a relatively localized  
 121 shearing zone that concentrates the deformation. They are therefore usually implemented  
 122 in "layered" frameworks (e.g., Hetland & Hager, 2005, 2006; K. Wang et al., 2012;  
 123 Sun & Wang, 2015), in which the structure of the system is prescribed and divided in  
 124 multiple pre-determined layers with different rheologies (e.g., an elastic layer of crust embedded  
 125 in a visco-elastic mantle) and is thus not allowed to evolve in time. With constant  
 126 mechanical parameters also, neither the Maxwell nor the Burgers model can reproduce  
 127 the transient deformations of fault systems over a wide enough range of time  
 128 scales (Ingleby & Wright, 2017; Periollat et al., 2022): deformations which translate for  
 129 instance in an Omori-like decay of post-seismic surface velocity (velocity inversely proportional  
 130 to the time since the earthquake), observed hours to ten of years after moderate to large  
 131 continental earthquakes (Ingleby & Wright, 2017).

132 A second category of models aim to represent the transition between stable and  
 133 unstable deformation regimes within the Earth crust by assimilating brittle and frictional  
 134 processes to the problem of friction on a material interface. This is the case for the well-known  
 135 block-slider framework, a parametric model stemming from experimental studies of the  
 136 frictional behaviour of various materials including rocks, which combines the principle of  
 137 linear elasticity and non-linear stick-slip friction between a sliding block and an underlying  
 138 surface. Purely conceptual models including these basic ingredients have first been used to  
 139 explain the statistical properties associated with major earthquakes, such as the Gutenberg-Richter  
 140 law (e.g., Burridge & Knopoff, 1967; Carlson & Langer, 1989). The rheology of frictional  
 141 interfaces has been later formulated as a constitutive law known as "rate-and-state friction"  
 142 (Dieterich, 1978, 1979a, 1979b) which has been widely used to model fault instabilities and  
 143 earthquakes (e.g., Liu & Rice, 2005; Segall & Bradley, 2012, and many others). This law  
 144 establishes the following relation between the measured friction coefficient,  $\mu$ , the sliding  
 145 velocity,  $V$ , and the state of the slip plane,  $\theta$ :  
 146

$$147 \quad \mu(\theta, V) = \mu^* + a \ln \frac{V}{V^*} + b \ln \frac{V^* \theta}{D_c}$$

148 where  $\mu^*$  is a friction coefficient at a reference sliding velocity,  $V^*$ ,  $a$  and  $b$  are proportionality  
 149 constants for the magnitude of instantaneous and time-dependant displacements respectively  
 150 and  $D_c$  is a characteristic slip distance for the evolution of the system towards a new stable  
 151 state. It is often coupled to an evolution equation for the state parameter,  $\theta$ , which describes  
 152 aging effects (Dieterich, 1979a; Ruina, 1983). For negative values of  $(a-b)$ , the model  
 153 describes a decrease of the friction coefficient with increasing sliding velocity and hence  
 154 an unstable, velocity-weakening state, assimilated to a brittle, seismic behaviour. For  
 155 positive values of  $(a-b)$ , it describes an increase of the friction coefficient with the  
 156 slip velocity, therefore a state of stable, velocity-hardening slip, assimilated to an  
 157 aseismic, ductile behaviour. By including additional levels of complexity relevant to  
 158 faults, which allow a change of sign of  $(a-b)$  along the interface (for instance, a  
 159 dependence of  $a$  and  $b$  on the temperature), this model can also reproduce transitions  
 160 between a brittle and a ductile behaviour and transient slip events (Liu & Rice, 2005,  
 161 2007; Segall & Bradley, 2012). Its main limitation, however, is that it is empirically-  
 162 based. As such, its extrapolation to the temporal and spatial scales of geophysical systems  
 163 such as faults on the basis of the results obtained in the laboratory is not trivial and  
 164 questionable (e.g., Chen et al., 2017; van den Ende et al., 2018). A second important  
 165 limitation is that it is an interface rheology, which implies a prescribed, non-evolving  
 166 location of the sliding plane and which does not take into account its microstructure or  
 167 its volumetric deformation. By this fact, it presents a limit to which it can be enriched

168 to include the highly relevant physico-chemical, mineralogical and hydro-mechanical pro-  
 169 cesses involved in the fault deformation cycle. It is also important to note that a "fault  
 170 plane" approach is in contradiction with seismic data and geological observations of ex-  
 171 humed faults, which suggest that the deformation occurs within a core zone made of gouge,  
 172 sandwiched between a metric to kilometric-scale zone of damaged rocks (Caine et al.,  
 173 1996; Angiboust et al., 2015; Hayman & Lavier, 2014; Gao & Wang, 2017).

174 Another category of models include continuum mechanics damage frameworks (e.g.,  
 175 Ashby & Sammis, 1990; Lyakhovsky, Reches, et al., 1997; Tang, 1997; Amitrano et al.,  
 176 1999; Bhat et al., 2012, and many others). So-called elasto-brittle schemes, which cou-  
 177 ple a damage variable to an elastic constitutive law, has indeed been used to represent  
 178 the fracturing processes and the associated strong localization of the deformation in faults  
 179 (e.g. Lyakhovsky, Ben-Zion, & Agnon, 1997; Lyakhovsky et al., 2001; Ben-Zion & Lyakhovsky,  
 180 2002, and later papers). Without accounting for the *dynamic* propagation of fractures  
 181 nor the generation of seismic waves, these models represent the redistribution of elas-  
 182 tic stresses caused by the generation and coalescence of micro-fractures and the complex  
 183 mechanical interactions in the material that stem from its micro-structural heterogene-  
 184 ity. They thereby present the advantage of simulating the emergence of a damaged shear-  
 185 ing or sliding zone (without the need to prescribe its location or geometry), the stable  
 186 to unstable transition of the system that precedes the macroscopic rupture as well as the  
 187 scaling laws associated with the localization of the deformation and the spatio-temporal  
 188 clustering of the seismic activity (e.g., Ben-Zion & Lyakhovsky, 2002; Turcotte et al.,  
 189 2003; Shcherbakov et al., 2005). An intrinsic limitation of such schemes, however, is that  
 190 they are based on an elastic constitutive law and as such, they cannot simulate any pre-  
 191 or post-rupture permanent deformation in the material. By this fact, it cannot repro-  
 192 duce the entire deformation cycle of faults. Hamiel et al., (Hamiel et al., 2004) and Dansereau  
 193 et al., (Dansereau et al., 2016a) therefore elaborated from elasto-brittle frameworks by  
 194 adding a viscous relaxation term that is coupled to the local level of damage in order to  
 195 represent, respectively, the small irreversible deformation that accumulate towards the  
 196 macro-rupture and the permanent and potentially large post-rupture deformation of the  
 197 fractured material. Their visco-elasto-brittle models have been shown to successfully sim-  
 198 ulate the scaling laws associated with brittle deformations in faults (e.g., Ben-Zion & Lyakhovsky,  
 199 2006) and a mechanically similar system: sea ice (Dansereau et al., 2016a; Rampal et  
 200 al., 2019; Ólason et al., 2021). However, in the context of faults, the numerically-coupled  
 201 treatment of damage propagation and viscous relaxation in these models makes them  
 202 too computationally expensive to cover the very long time scales associated with duc-  
 203 tile deformations and hence reproduce multiple deformation cycles.

204 Finally, other models have been developed to help understanding the dynamics of  
 205 fluids and its role in the deformation of faults (e.g. Segall & Rice, 1995, and many oth-  
 206 ers). In particular, recent idealized models of pressure diffusion in the host rock with rapidly  
 207 varying permeability have been able to explain the observed rapid tremor migrations and  
 208 their reversals (Cruz-Atienza et al., 2018; Farge et al., 2021). However, a very impor-  
 209 tant challenge remains to day: to couple these models with the two- or three-dimensional  
 210 deformation of the solid matrix and other near-fault processes to allow assessing their  
 211 impact on the geodetically observed strains.

## 212 1.2 Focus on the Slow Earthquake Phenomenon

213 Developing a single numerical modeling framework suitable for all of the above men-  
 214 tioned physical processes and that can cover the entire spectrum of associated time scales  
 215 is a very ambitious, perhaps unachievable, goal. Therefore, in this paper, we focus on  
 216 modelling the mechanical behaviour and deformation of fault zones, leaving aside for the  
 217 moment the role of fluids. We also concentrate over time scales intermediate between  
 218 those characterizing the cycle of major, or "classical", earthquakes (from decades to thou-

sands of years) and the one of dynamic rupture (faster than hundreds of seconds). Within this range, the deformation of faults is often controlled by slow earthquakes.

The slowest temporal scale associated with the slow earthquake phenomenon is revealed by geodetic observations of the accompanied slow and diffuse surface deformation, with typical event durations between weeks and months and inter-events gaps of the order of a few years (e.g., Dragert et al., 2001; Kostoglodov et al., 2003; Radiguet et al., 2012). The fastest temporal scale is related to seismic radiations, observed at frequencies above 1 Hz in the form of tectonic tremors (e.g., Obara, 2002; Payero et al., 2008) or low-frequency earthquakes (LFEs) (e.g., Shelly et al., 2006; Bostock et al., 2012; Frank et al., 2014) and which imply localized, brittle deformations and associated elastic strain variations in the source region on the order of fractions of a second. Therefore, even if ignoring the second-order effect of the long-term deformation of the system attributable to mantle relaxation, convection and delayed elastic deformations, as done in this paper, building a model for slow earthquakes entails dealing with localized, brittle deformations and diffuse, ductile deformations that are separated by about 8 orders of magnitudes of time scales. This huge separation requires developing a numerical scheme that allows simulating the relevant processes in reasonable simulation times.

This is the aim of the current work : developing a physically sound and numerically efficient continuum rheological framework for slow earthquakes. It is important to note however that doing so, we also keep in mind a future application to a wider range of time scales relevant to the entire seismic cycle. Another objective is that this framework be simple and versatile, so that to give valuable insights and eventually be transferable in the context of other geophysical systems that are characterized by a similar dynamics, that is, a dynamics comprised of mixed brittle/ductile and transient deformations, such as landslides and volcanic edifices (e.g., Peng & Gomberg, 2010; Lacroix et al., 2014; Carrier et al., 2015; Got et al., 2017; Handwerger et al., 2016; Poli, 2017; Parisio et al., 2019; Seydoux et al., 2020, and many others). A very important feature of the proposed modelling approach is that it accounts for rock fracturing processes via a progressive damage mechanism that is coupled to the mechanical strength of the material, which is described not only by an elastic moduli but also an apparent viscosity. As such, in addition to the long-term evolving strain of the system (observed with GPS, tiltmeters, strainmeters) the model represents the short-term temporal evolution of the averaged energy of seismic radiations (observed as tremors and LFEs).

The rheological model is presented in section 2, together with its numerical scheme. Its implementation in an idealized shearing experiment that is relevant in the context of subduction zones is described in section 3. The main characteristic numbers and times describing this experiment are described in section 4. Section 5 presents a demonstration of its mechanical and numerical behaviour, with a sensitivity analysis on the value of its main parameters. This analysis demonstrates its capability to simulate the wide separation of scales between the brittle and ductile processes and transient deformations at the intermediate time scales.

## 2 The Physical Model

The model builds on the Burgers framework, which combines the Maxwell (an elastic and a viscous component in series) and the Kelvin-Voigt (an elastic and a viscous component in parallel) visco-elastic models (see figure 1). As mentioned in section 1.2, for the sake of the current paper we neglect the effect of the delayed elasticity of the mantle, which is responsible for instance for the reversal of surface velocities following major earthquakes but is probably of second-order in the context of slow earthquakes. In the following description, the model is therefore reduced to the Maxwell component. In particular, we focus on testing the capability of this component to reproduce transient

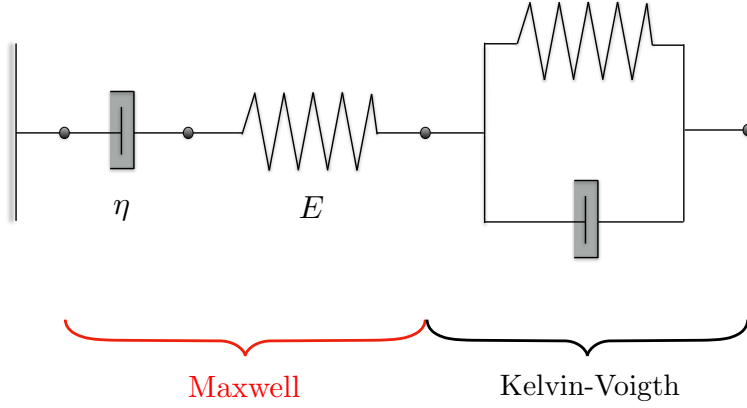


**Figure 1.** Schematic representation of the Burgers model. When loaded with a constant deformation, the Maxwell component undergoes a relaxation (exponential decay) of the stress. When unloaded, the part of the deformation associated to the viscous element is non-recoverable. When loaded with a constant stress, the Kelvin component leads to an exponential decay of the deformation. When unloaded, this deformation is fully recoverable. The implementation of the model described in this paper neglects the Kelvin component.

269 deformations and a deformation cycle akin slow earthquakes when  $E$  and  $\eta$  are not constant  
 270 but allowed to evolve in both space and time, according to the local degree of fracturing  
 271 of the material at the sub-grid scale, the so-called *level of damage*. The development  
 272 of the current visco-elastic framework therefore lies crucially on the formulation  
 273 of a coupling between  $E$  and  $\eta$  and this level of damage. The starting point of this coupling  
 274 follows the simple formulation suggested by (Dansereau et al., 2016a), which was  
 275 shown to successfully reproduce the spatial localization and intermittency of the damage  
 276 and deformation and associated scaling laws in another quasi-brittle material that  
 277 undergoes permanent deformations partially dissipating stresses when fractured; sea ice.

278 Another particularity of our approach is that, contrary to existing visco-elastic layered  
 279 models (e.g., K. Wang et al., 2012; Sun & Wang, 2015), here a unique rheology is  
 280 applied to the entire system (see figure 2). Its component are differentiated solely on the  
 281 basis of the bulk elastic modulus and on the local level of damage.

## 282 2.1 Constitutive Equation

283 The Maxwell model is applied here in the context of an elastic, compressible solid.  
 284 Its constitutive law reads

$$285 \frac{D\sigma}{Dt} + \frac{1}{\lambda}\sigma = E\mathbf{K} : \dot{\epsilon}, \quad (1)$$

286 where  $\mathbf{K}$  is the elastic stiffness tensor, defined in terms of Poisson's ratio,  $0 \leq \nu < 0.5$ ,  
 287 and from which the elastic modulus,  $E$ , is factored out. For any three-dimensional symmetric  
 288 tensor  $\epsilon = \epsilon_{ij} \in i, j; 1 \leq i, j \leq 3$ ,  $(\mathbf{K} : \epsilon)_{ij} = \frac{\nu}{(1+\nu)(1-2\nu)} \text{tr}(\epsilon)\delta_{ij} + 2\frac{1}{2(1+\nu)}\epsilon_{ij}$ .  
 289 The strain rate tensor,  $\dot{\epsilon}$  is taken equivalent to the rate of strain tensor and is given by  
 290  $D(\mathbf{u}) = \frac{\nabla\mathbf{u} + \nabla\mathbf{u}^T}{2}$  where  $\mathbf{u}$  is the velocity. The ratio of the material's apparent viscosity  
 291 and elastic modulus,  $\lambda = \eta/E$ , hereinafter referred to as the relaxation time, sets  
 292 the mesoscopic rate of dissipation of the stresses through permanent deformations.

293 Following Kachanov (1958) and previous isotropic damage models (e.g., Tang, 1997;  
 294 Lyakhovsky, Ben-Zion, & Agnon, 1997; Amitrano et al., 1999) the density of cracks at  
 295 the sub-grid scale is described by a mesoscopic scalar damage variable,  $d$ , the value of  
 296 which evolves between 0 for an undamaged and 1 for a totally damaged material (see

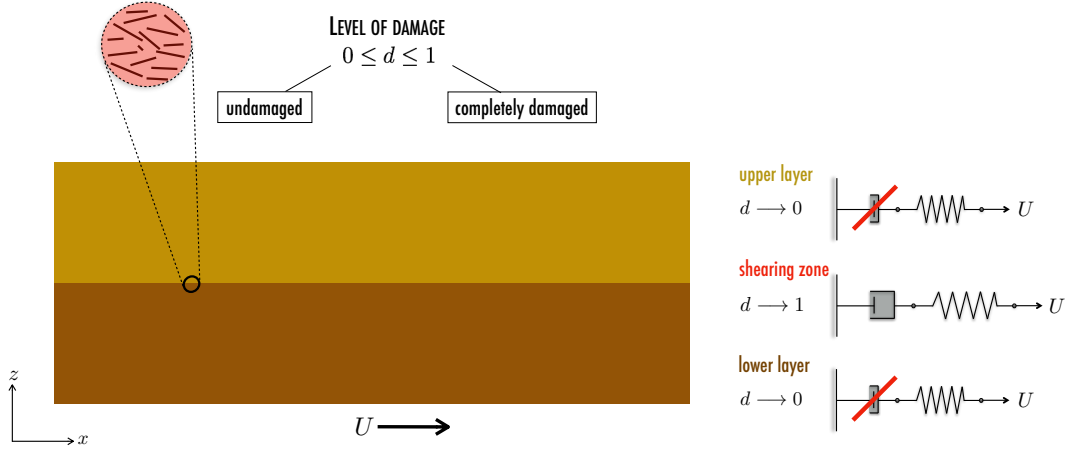


**Figure 2.** Schematic representation of the model and simulations, which represent a vertical ( $x, z$ ) cross-section of two layers of host rock sheared by applying a constant velocity at the bottom of the lower layer, in the  $x$ -direction. A unique visco-elasto-brittle constitutive law is applied to the entire system. The two layers are differentiated only on the basis of the undamaged value of their elastic modulus. The expected mechanical behaviour is one in which the bulk of both layers is quasi-elastic, since damage there is expected to be almost zero and the effective viscosity is high, and visco-elastic at the interface of the two layers, where the deformation and damage are localized and potentially high and the elastic modulus and apparent viscosity much reduced.

297 figure 2). In the case of the elastic modulus, the coupling to  $d$  is based on the principle  
 298 of effective stress (Kachanov, 1958) and reads

$$299 \quad E = E_0(1 - d), \quad (2)$$

300 where  $E_0$  is the undamaged elastic modulus of the material. In the case of the effective  
 301 viscosity,  $\eta$ , the coupling reads:

$$302 \quad \eta = \eta_0(1 - d)^\alpha, \quad (3)$$

303 where  $\eta_0$  is the bulk viscosity of the material, i.e., its viscosity in its undamaged state,  
 304 and  $\alpha$  is an exponent  $> 1$  such that the relaxation time,  $\lambda$ , setting the rate of dissipa-  
 305 tion of the stresses, decreases with the degree of fracturing of the material. This ad-hoc  
 306 but simple coupling allows, on the one hand, the dissipation of the stress through per-  
 307 manent deformations where the material is damaged and, on the other hand, the conserva-  
 308 tion of the stress associated to elastic deformations where the material is relatively  
 309 undamaged (Dansereau et al., 2016a; Weiss & Dansereau, 2017).

## 310 2.2 Progressive Damage Mechanism

311 The level of damage in the model evolves due to both fracturing and healing pro-  
 312 cesses. The first of these processes translates into an increase in  $d$  and its occurrence is  
 313 determined at any given model iteration by comparing the local state of stress to a criti-  
 314 cal stress value, set by a chosen damage criterion. The present implementation uses the  
 315 Mohr–Coulomb criterion

$$316 \quad \sigma_1 = q\sigma_2 + \sigma_c, \quad (4)$$

317 where  $\sigma_1$  and  $\sigma_2$  are the principal stresses,  $q = [(\mu^2 + 1)^{1/2} + \mu]^2$ ,  $\mu$  is the internal fric-  
 318 tion coefficient and  $\sigma_c = \frac{2C}{[(\mu^2 + 1)^{1/2} - \mu]}$ , where  $C$  is a non-zero cohesion (resistance of  
 319 the material to pure shear). No truncation is applied here to this criterion in the case

320 of  $\sigma_1, \sigma_2 < 0$  : hence it includes tensile stresses. In a manner similar to other damage  
 321 modelling frameworks, some noise is introduced in this criterion, by drawing the value  
 322 of  $C$  over each element of the discretized domain from a uniform distribution, to repre-  
 323 sent the heterogeneity of natural materials and insure progressive failure even under per-  
 324 fectly homogeneous forcing conditions.

325 As in the elasto-brittle model of (Amitrano et al., 1999),  $d$  evolves due to damag-  
 326 ing following

$$327 \quad 1 - d' = \delta d(1 - d), \quad (5)$$

328 where  $d'$  is the post-damaging value of damage,  $d$ , the pre-damaging value and  $\delta d$ , a con-  
 329 stant multiplication factor such that  $\delta d = 0$  when and where the state of stress is sub-  
 330 critical and  $0 < \delta d \leq 1$  when and where it is over-critical with respect to the damage  
 331 criterion. According to equations (2) and (3), each damage event implies that the local  
 332 elastic modulus and apparent viscosity decrease respectively as

$$333 \quad E' = \delta d E \quad (6)$$

$$334 \quad \eta' = \delta d^\alpha \eta \quad (7)$$

335 where the superscript  $'$  is hereinafter used to denote the post-damage strength, stress  
 336 and deformation. This local decrease in mechanical strength leads to an elastic redis-  
 337 tribution of the stresses from the over- to the sub-critical areas of the material, which  
 338 allows for the triggering of avalanches of damaging events, representing the propagation  
 339 of cracks at the mesoscale, as long as the elastic modulus (or relaxation time) or the ma-  
 340 terial remains significant. It is important to note that, as other damage frameworks, the  
 341 current model is not *dynamic* and as such, is not meant to capture the propagation of  
 342 the rupture that generates seismic waves. Instead, it aims at representing the effect of  
 343 such rupture processes on the deformation of the material.

344 In developing the model, we take advantage of the very large separation of scales  
 345 between the brittle and ductile deformations in faults to make the assumption that the  
 346 first type of deformation is quasi-instantaneous relative to the second type. As such, we  
 347 treat the evolution of the level of damage as independent of time. The same approxima-  
 348 tion is implicitly made in the time-independent (linear) elasto-brittle brittle model of (e.g.,  
 349 Amitrano et al., 1999). Here, we therefore follow a similar approach and formulate a steady-  
 350 state, iterative scheme for the stress redistribution associated with micro-fracturing and  
 351 fracture coalescence at the sub-grid scale. This formulation relies on two hypotheses:

- 352 1. the *immediate* effect of damage is to redistribute the local stresses, not strains.  
 353 In the following, this immediate post-damage state is referred to using the "\*" su-  
 354 perscript,
- 355 2. as the propagation of damage is quasi-instantaneous compared to viscous relax-  
 356 ation processes in the material considered, the viscous stress dissipation term in  
 357 equation (1) can be neglected when solving for the damage propagation. The con-  
 358 stitutive equation therefore reduces to that of a linear-elastic material:

$$359 \quad \sigma = E\mathbf{K} : \varepsilon,$$

360 where  $\varepsilon$  is the deformation (as opposed to the deformation rate) tensor.

361 The following constitutive equations thereby define respectively the pre- and immedi-  
 362 ate post-damage states:

$$363 \quad \sigma = E\mathbf{K} : \varepsilon,$$

$$364 \quad \sigma^* = E^*\mathbf{K} : \varepsilon^*,$$

365 Using the first hypothesis laid above, the following equality relating the pre-damage and  
 366 the immediate post-damage elastic modulus (respectively  $E$  and  $E^*$ ) and stresses ( $\sigma$  and

367  $\sigma^*$ ) can be written

$$368 \quad \frac{\sigma^*}{E^*} = \frac{\sigma}{E}.$$

369 Using equation (6), the immediate post-damage stress adjustment is therefore given by

$$370 \quad \sigma^* = \sigma \delta d.$$

371 Considering further that this local stress adjustment induced by the damage event will  
 372 lead, in a second time, to an adjustment in the neighbouring deformation and so, stress,  
 373 the new state of equilibrium between the post-damage stress,  $\sigma'$ , and the post-damage  
 374 deformation,  $\varepsilon'$ , is given by

$$375 \quad \sigma' - \sigma \delta d = E_0(1 - d')\mathbf{K} : \varepsilon'. \quad (8)$$

### 376 **2.3 Healing Mechanism**

377 Healing is another essential ingredient for the reproduction of the deformation of  
 378 fault zones (e.g., Bos & Spiers, 2002; Renard et al., 2000, and many others). In the case  
 379 of damaged rocks and rock gouges, it can include various processes, like sintering (e.g.,  
 380 Hirono et al., 2020), cementing and sealing from dissolution-precipitation processes (e.g.,  
 381 Sibson, 1992; R. T. Williams, Mozley, et al., 2019), motion/diffusion of asperities and  
 382 dislocations (e.g., Dieterich, 1979a, 1979b, and many others) and compaction (e.g., Hun-  
 383 feld et al., 2020). In the current model, the respective effects of all of these processes are  
 384 not differentiated but rather encapsulated into a single healing law that prescribes a de-  
 385 crease in the level of damage at a constant rate such that:

$$386 \quad \frac{Dd}{Dt} = -\frac{1}{t_h}d, \quad 0 \leq d < 1, \quad (9)$$

387 where  $t_h$  the healing time. Through their respective coupling to  $d$ , both the elastic mod-  
 388 ulus and apparent viscosity are therefore allowed to re-increase towards their bulk value  
 389 after damage events : a behaviour that is consistent with observations of the evolution  
 390 of seismic velocities (Li & Vidale, 2001; Brenguier et al., 2008). This very simple law,  
 391 used here for the purpose of demonstrating the general impact of healing on the mod-  
 392 elled mechanical behaviour, could be refined in more realistic implementations of the model  
 393 (see section 11).

### 394 **2.4 The Coupled Visco-Elasto-Brittle Model**

395 The proposed model couples the time-independent treatment of the damage prop-  
 396 agation with the time-dependant, visco-elastic Maxwell constitutive equation and the  
 397 time-dependant evolution equation for healing. To do so, the complete system of equa-  
 398 tions is solved in three steps or subproblems ( $P$ ):

- 399 ( $P1$ ) The full constitutive equation (1) is first solved together with the full momentum  
 400 equation, boundary and forcing conditions (see section 3) and using the field of  
 401 damage at the previous time step for a first estimate of the field of velocity and  
 402 stress at the current time step. The field of stress is then compared to the local  
 403 damage criterion.
- 404 ( $P2$ ) *If and only if* the stress locally exceeds the damage criterion, the forcing is paused  
 405 and the macroscopic deformation of the simulated material is held constant. The  
 406 model enters a steady-state subiteration in which (i) the level of damage,  $d$ , is ad-  
 407 justed to its post-damage value,  $d'$ , (ii) equation (8) is solved for the adjusted state  
 408 of stress,  $\sigma'$ . These two steps are carried iteratively until all states of stresses be-  
 409 come sub-critical, at which point the stress state at the current time is set to the  
 410 adjusted stress at the final subiteration.

411 (P3) The healing equation (9) is solved for the field of damage at the current time step,  
 412 using the post-damaging level of damage,  $d'$ .

413 This scheme is illustrated schematically in figure 3 and presented in full details in Ap-  
 414 pendix B.

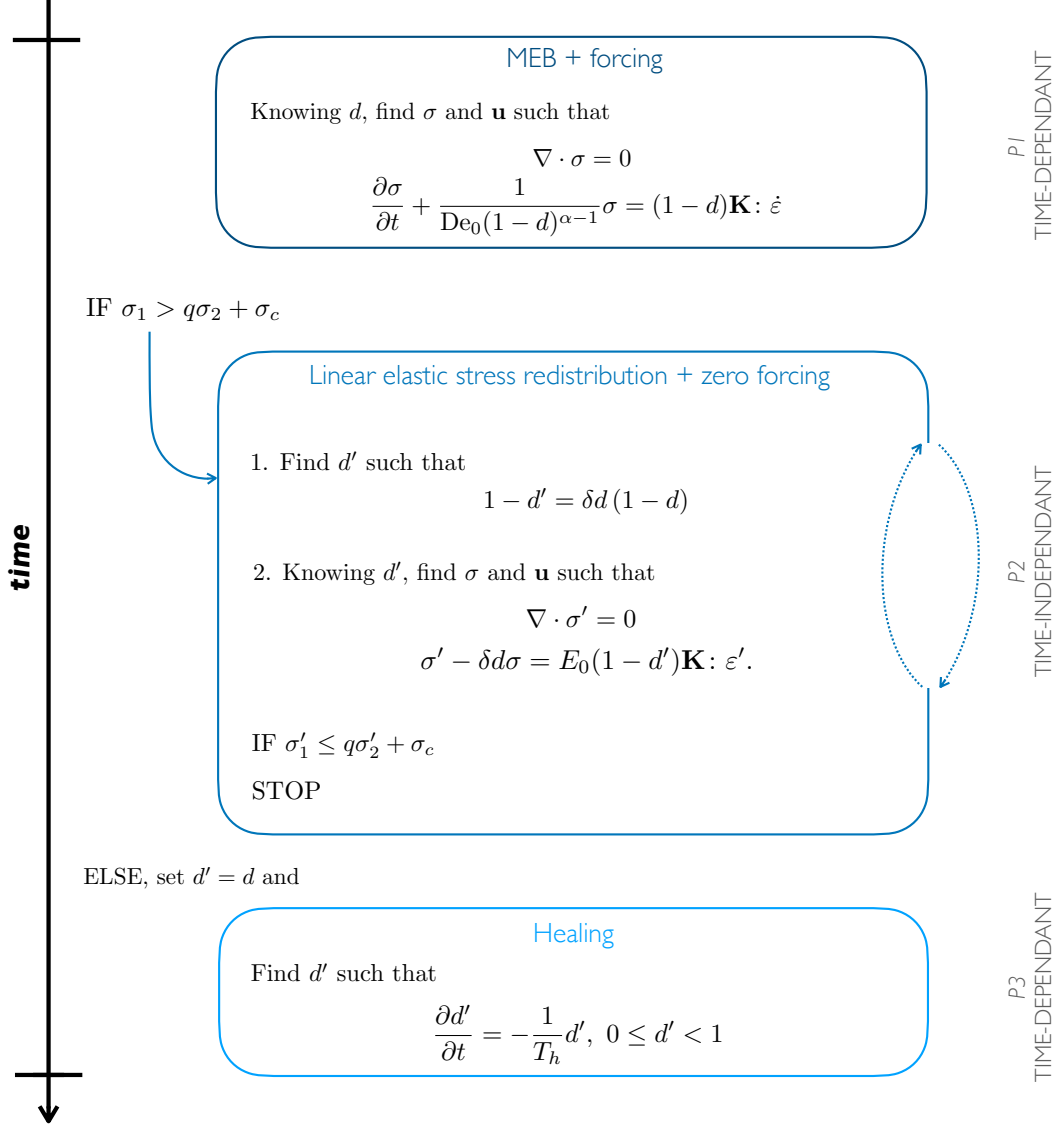


**Figure 3.** Schematic representation of the numerical scheme, composed of the three sub-problems, and its resolution over one model time step. For simplicity, the superscript ‘~’ for adimensional variables is dropped. The full numerical scheme and time discretization is described in Appendix B.

### 415 3 Implementation

416 The model is implemented here in a 2-dimensional shearing experiment (see figure  
 417 4), meant as a very idealized representation of a vertical cut  $(x, z)$  through a sub-  
 418 duction zone. Two layers of host rock are sheared by applying a constant  $x$ - velocity

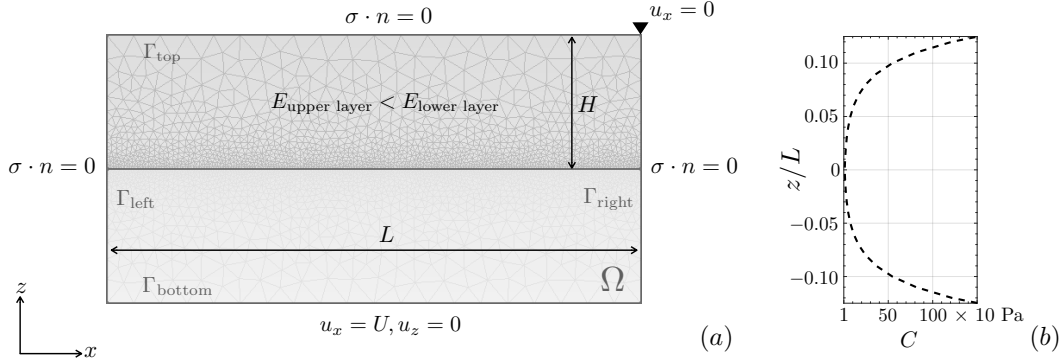


**Figure 4.** (a) Simulation setup. The domain, boundaries and boundary conditions are detailed in Appendix B. (b) Functional dependence of the cohesion,  $C$ , (i.e., of the damage criteria) on  $z$ , prescribed to avoid concentrating most of the deformation at the top and bottom boundaries, where the  $x$ -velocity is either locally or entirely prescribed.

419 at the bottom of the lower layer. No confinement is applied on the lateral sides and the  
 420 surface is free, except for the top, right corner of the domain (the furthest surface point  
 421 downstream and in the direction of the forcing), for which  $u_x = 0$ . The horizontal ext-  
 422 ent of the system perpendicular to the shearing direction is considered much greater than  
 423 the horizontal extent in the shearing direction. Plane strains are therefore assumed. No  
 424 discontinuity is introduced over the domain other than in the value of the undamaged  
 425 elastic modulus,  $E_0$ , which is lower by a factor of 3 in the upper layer, representing the  
 426 continental crust, than in the lower layer, representing the oceanic crust (see table 1).  
 427 Also, in order to avoid that all of the deformation be trivially accommodated near the  
 428 bottom boundary of the domain, where a non-zero  $x$ -velocity is prescribed, or near the  
 429 top, right corner of the domain, where the  $x$ -velocity is fixed to 0, a functional depen-  
 430 dence of  $C$  on  $z$  is prescribed, of the form  $C = C_0 \times \exp(|5.0 * z/H|)$ , where  $H$  is the  
 431 thickness of both layers (see figure 4b) and  $C_0$  is the minimum cohesion. This function  
 432 allows the magnitude of  $C$  to vary little over a wide enough range of values of  $z$  centred  
 433 on  $z = 0$  (e.g.,  $C(z = 0.01) = 1.5 \times C(z = 0)$ ) and therefore does not affect the degree  
 434 of localization of the deformation in the shearing zone that forms between the two sim-  
 435 ulated layers. Over each grid cell element, this function is locally multiplied by a value  
 436 that is picked randomly over a uniform distribution of values over the range  $[0.75 \ 1]$ , thereby  
 437 introducing some noise in the local damage criteria that represents the natural hetero-  
 438 geneity of the material (see section 2.2).

439 The balance of forces in the experiment neglects inertia and advection. In order  
 440 to avoid introducing artifacts in the solution related to our finite-size domain and bound-  
 441 ary conditions, we also neglect gravity. The momentum equation therefore reads:

$$442 \quad \nabla \cdot \sigma = 0. \quad (10)$$

443 As slow earthquakes entail deformations (i.e., slip) that are relatively small relative to  
 444 the horizontal and vertical extent of subduction zones, the advection, rotation and de-  
 445 formation terms which are included in material derivatives in the constitutive equation  
 446 (1) and healing equation (9), are all neglected, such that  $\frac{D\sigma}{Dt} = \frac{\partial\sigma}{\partial t}$  and  $\frac{Dd}{Dt} = \frac{\partial d}{\partial t}$ . In  
 447 all simulations performed here, the total, cumulative deformation of the system remains  
 448 below 10% of the the size of the smallest mesh element, ensuring that this approxima-  
 449 tion is indeed valid. The effect of the elastic deformations on the material's density are  
 450 neglected as well, such that mass conservation does not need to be imposed.

Model/setup parameters		Value
Length of the domain	$L$	$10^6, 10^4, 10^2$ m
Thickness of both layers	$H$	$\frac{1}{8}L$
Tectonic forcing velocity	$U$	$10^{-9}$ m s $^{-1}$
Undamaged relaxation time	$\lambda_0 = \frac{\eta_0}{E_0}$	$10^{12}$ s
Poisson's ratio	$\nu$	0.3
Internal friction coefficient	$\mu$	0.7
Maximal cohesion	$C_0$	$10^4$ Pa

**Table 1.** Model and simulation parameter values.

451 The model equations are discretized in time using a backward Euler scheme of order  
452 1 (see section B01 of the Appendix for the details) and discretized in space using fi-  
453 nite elements. In the following,  $\Delta t$  designate the model time step and  $\Delta x$ , the spatial  
454 resolution of the mesh grid. The triangular elements grid used is built using the Gmsh  
455 generator (Geuzaine & Remacle, 2009). As the model is isotropic by construction, and  
456 in order to avoid preferential orientations in the localization of the deformation, it is cho-  
457 sen unstructured. The spatial resolution,  $\Delta x$ , is set to be 1/20 of the horizontal extent,  
458  $L$ , of the domain at the top and bottom boundaries. It is refined by a factor of 10, so  
459 that to be 1/200 of  $L$ , at the junction of the two layers (see Figure 4) where deforma-  
460 tion is expected to be maximal. As cumulative deformations are small in all simulations,  
461 the deformation of the mesh is not calculated and the position of grid nodes, not updated  
462 in time. The resolution of the variational formulation of the equations make use of the  
463 C++ library RHEOLEF (Saramito, 2020). The polynomial approximations for  $\mathbf{u}$  are of  
464 order 1 and continuous at inter-element boundaries. As the stress tensor is a function  
465 of the velocity gradient and the damage, a function of the stress tensor, the approxima-  
466 tions for  $\sigma$ ,  $\sigma'$ ,  $d$  and  $d'$  are of degree 0 and discontinuous at inter-element boundaries.

#### 467 4 Adimensional System of Equations and Adimensional Parameters

468 In all of the simulations performed here, the system of equations is solved and re-  
469 sults are expressed in adimensional form. This allows describing and exploring the sen-  
470 sitivity of the rheological framework in terms of a reduced set of parameters and using  
471 the same idealized setup to represent systems with different physical dimensions and/or  
472 deformation time scales.

473 The model is made adimensional with respect to the horizontal extent,  $L$ , of the  
474 domain, the constant velocity prescribed at the bottom of the lower layer,  $U$ , and the  
475 average of the undamaged elastic modulus of the two layers,  $E_0$ . The time,  $T$ , charac-  
476 terizing the deformation process is therefore given by  $\frac{L}{U}$ . The superscript ‘~’ is used for  
477 all dimension-less variables and operators, which are listed in table A1. For a full descrip-  
478 tion of the adimensional formulation of the variables and equations, the reader can re-  
479 fer to Appendix A.

480 The complete adimensional system of equations reads

481 
$$\tilde{\nabla} \cdot \tilde{\sigma} = 0 \quad (11)$$

482 
$$\frac{\partial \tilde{\sigma}}{\partial \tilde{t}} + \frac{1}{\text{De}_0(1-d)^{\alpha-1}} \tilde{\sigma} = (1-d)\mathbf{K} : \tilde{\varepsilon}, \quad (12)$$

483 
$$1-d' = \delta d(1-d) \quad (13)$$

484 
$$\tilde{\nabla} \cdot \tilde{\sigma}' = 0 \quad (14)$$

485 
$$\tilde{\sigma}' - \delta d \tilde{\sigma} = (1-d')\mathbf{K} : \tilde{\varepsilon}' \quad (15)$$

486 
$$\frac{\partial d'}{\partial \tilde{t}} = -\frac{1}{T_h} d', \quad 0 \leq d' < 1, \quad (16)$$

487 with the damage criterion

488 
$$\tilde{\sigma}_1 = [(\mu^2 + 1)^{1/2} + \mu]^2 \tilde{\sigma}_2 + \frac{2C/E_0}{[(\mu^2 + 1)^{1/2} - \mu]}. \quad (17)$$

489 The value of Poisson's ratio,  $\nu$ , and of the internal friction coefficient,  $\mu$ , are fixed in the  
 490 following simulations to values common for geomaterials (Byerlee, 1978; Jaeger & Cook,  
 491 1979). The brittleness of the material, given by the ratio of the cohesion to the undam-  
 492 aged elastic modulus,  $C_0/E_0$ , is also kept constant. Besides these parameters, the four  
 493 adimensional parameters that characterize the model are:

- 494 1.  $\text{De}_0 = \frac{\eta_0}{E_0} \frac{U}{L}$ , the (undamaged) Deborah number,  
 495 2.  $\alpha$ , the damage parameter, setting the rate at which the viscosity (or relaxation  
 496 time) decreases with the level of damage,  
 497 3.  $\delta d$ , the damage increment,  
 498 4.  $T_h = \frac{t_h}{T}$ , the time for healing,

499 The limits and range of values over which these parameters are varied in the sensitiv-  
 500 ity experiments performed here are summarized in Table 2 and discussed in the follow-  
 501 ing sub-sections.

Adimensional parameter		Range of values
Characteristic healing time	$T_h$	$10^{-1} - 10^{-7}$
Undamaged Deborah number	$\text{De}_0$	0.01, 0.1, 10
Damage increment	$\delta d$	0.1, 0.3, 0.5, 0.7, 0.9
Damage parameter	$\alpha$	2, 3, 4, 6, 8

**Table 2.** Adimensional model parameters and the range of values over which they are varied in the model sensitivity experiments.

502 **4.1 The Deborah Number, De**

503 The Deborah number can be defined as the dimensionless ratio of the viscous re-  
 504 laxation time for the stress,  $\lambda$ , and of the time for the deformation process,  $T = \frac{L}{\dot{\gamma}}$ , (i.e.,  
 505 the inverse of the macroscopic shearing rate). It characterizes the fluid-like versus elas-  
 506 tic solid-like behaviour in unsteady flows, and as such is a relevant quantity to charac-  
 507 terize the deformation of faults and the slow earthquake phenomenon. Materials char-  
 508 acterized by a low Deborah number, either because they dissipate stresses rapidly or be-  
 509 cause they are deformed very slowly, have a behaviour that approaches that of a (New-

510 tonian) fluid and therefore flow steadily. Materials characterized by a high Deborah num-  
 511 ber, either because they dissipate stresses very slowly or because they are deformed rapidly,  
 512 behave like elastic solids and flow unsteadily.

513 Compared to classical earthquakes, slow earthquakes appear to be a less intermit-  
 514 tent, or equivalently a more steady, and therefore a more predictable form of deforma-  
 515 tion. Indeed, in some subduction zones like Cascadia (Dragert et al., 2001) and Guer-  
 516 rero, Mexico (Cotte et al., 2009; Radiguet et al., 2012) major slow earthquake episodes  
 517 show approximately stable recurrence times. However, the recurrence interval of slow  
 518 slip events varies greatly from one subduction zone to another. For instance, it is of a  
 519 few months in some segments of the Nankai subduction in Japan (e.g., Poiata et al., 2021),  
 520 on the order of one year in Cascadia, and of nearly four years in Guerrero. Recurrence  
 521 interval are also known to differ for different segments of the same subduction zone (e.g.,  
 522 Brudzinski & Allen, 2007) and are observed to decrease with depth (e.g., Wech & Crea-  
 523 ger, 2011; Frank, Radiguet, et al., 2015).

524 To take into account this variability in our simulations, as well as the variability  
 525 and uncertainty related to the mechanical properties of the crust (elastic modulus and  
 526 viscosity), we explore three values of the *undamaged* Deborah number (0.001, 0.1 and  
 527 0.1, see table 3) each separated by two orders of magnitude. Practically, in the simula-  
 528 tions, these different values are obtained by varying the time associated with the defor-  
 529 mation process,  $T = \frac{L}{\dot{\epsilon}}$ , and maintaining the undamaged relaxation time,  $\lambda_0 = \frac{\eta_0}{E_0}$ ,  
 530 constant ( $\lambda_0 = 10^{12}$  s). This relaxation time is consistent with an undamaged elastic  
 531 modulus,  $E_0$ , on the order of  $10^{11}$  Pa (in agreement with e.g., Dziewonski & Anderson,  
 532 1981) and a bulk, undamaged viscosity,  $\eta_0$ , of  $10^{23}$  Pa s (Siravo et al., 2019) for both the  
 533 continental and oceanic crust. The deformation process time,  $T$ , is set by considering  
 534 a typical tectonic velocity of  $10^{-9}$  m/s (on the order of a few cm/year) and considering  
 535 different horizontal extent,  $L$ , over which the fault is activated and slip occurs. The low-  
 536 est value of  $De_0$  explored considers  $L = 10^6$  m (1000 km), representative of a large sub-  
 537 duction zone. Following the definition of the Deborah number, this lower bound can be  
 538 interpreted alternatively as representing a smaller but deeper, hence lower viscosity seg-  
 539 ment of a fault. The highest value is representative of a small activated segment (1000  
 540 m) or alternatively, as a larger but shallower and hence more brittle part of a fault.

541 It is very important to note, however, that while  $De_0$  sets the bulk fluid-like ver-  
 542 sus elastic solid-like behaviour of the system and therefore is a relevant quantity to char-  
 543 acterize the macroscopic deformation cycle, for instance in terms of its duration, in the  
 544 visco-elasto-brittle model presented here, the *effective* Deborah number,  $De$ , is not ho-  
 545 mogeneous throughout the system but varies in space and time. Indeed, according to equa-  
 546 tions (2) and (3),  $De$  evolves locally as a function of the level of damage, as  $De = De_0 d^{\alpha-1}$ .  
 547 In all three systems, this decrease will leads to a more fluid-like behaviour where and when  
 548 the host rock becomes damaged.

## 549 4.2 The Healing Time, $T_h$

550 In the present model, the healing time represents the time it takes for a completely  
 551 damaged element ( $d = 1$ ) to evolve back to its undamaged state ( $d = 0$ ) and recover  
 552 entirely its mechanical strength. Since several different healing processes are thought to  
 553 be at play in faults (see section 2.3) and the rates at which these different processes very  
 554 likely depend on various local factors, like pressure, temperature, the availability of flu-  
 555 ids and the type of rock (see for instance McLaskey et al., 2012), estimating  $T_h$  is highly  
 556 non-trivial. Therefore, we define our estimation here based on lower and upper bounds  
 557 values. On the one hand, observations of post-seismic velocity changes, which estimates  
 558 the time required for the velocity of  $P$  and  $S$  waves (or, by extension, the elastic mod-  
 559 ulus of the crust in the vicinity of the fault) to re-increase to their pre-seismic value, place  
 560 the lower bound to a few (2-5) years (e.g., Li et al., 1998; Brenguier et al., 2008). Indeed,

561 while cracks that open during the mainshock probably close partially with time, one still  
 562 expects the vicinity of the shearing zone to remain highly damaged relative to the sur-  
 563 rounding host rock and that, at all times. On the other hand, assuming that the fault  
 564 heals completely between large earthquakes, the upper bound can be estimated from pseudo-  
 565 recurrence times, which reach a few thousand years in some faults (e.g., Li et al., 1998;  
 566 R. T. Williams, Davis, & Goodwin, 2019).

567 Four orders of magnitude of healing time are explored here, which vary between  
 568 these lower and upper bounds. In dimensional form, these values are:  $t_h = 10^8$  s, which  
 569 is equivalent to about  $\sim 3$  years,  $10^9$  s ( $\sim 30$  years),  $10^{10}$  s ( $\sim 300$  years) and  $10^{11}$  s  
 570 ( $\sim 3000$  years). Since different  $De_0$  numbers are explored by varying the process time  
 571  $T$ , and as time in our system of equations is made adimensional with respect to  $T$  (see  
 572 section 4), the different  $De_0$  lead to different adimensional values of the time of healing,  
 573  $T_h$ . The dimensional and corresponding adimensional values of  $t_h$  and  $T_h$  correspond-  
 574 ing to each  $De_0$  are listed in table 3.

### 575 4.3 The Damage Parameter, $\alpha$

576 As mentioned in section 2.2, the purpose of the rather "ad-hoc" damage param-  
 577 eter,  $\alpha$ , is that the model accounts for a more rapid dissipation of the stresses where the  
 578 material is highly damaged than where it is relatively undamaged. The only physical con-  
 579 straint on its value is therefore  $\alpha > 1$ . There is no theoretical upper bound for  $\alpha$ . How-  
 580 ever, for  $\alpha$  large, the relaxation time becomes very small at the onset of damage, what-  
 581 ever the damage level. Dansereau (2016b) and Weiss and Dansereau (2017) have demon-  
 582 strated that in this case, stresses are readily dissipated after each damage event and the  
 583 mechanical behaviour becomes essentially elasto-plastic. Here, the sensitivity of the model  
 584 is investigated for values of  $\alpha$  between 2 and 8, which proves to be a wide enough range  
 585 of values for the model to exhibit different mechanical behaviours relevant in the con-  
 586 text of faults and slow earthquakes.

### 587 4.4 The Damage Increment, $\delta d$

588 Similar to the damage parameter, the value of the damage increment is not con-  
 589 strained other than within the range of values intrinsic to its definition : between 0 and  
 590 1. It is however expected to be determinant on the mechanical response of the model.  
 591 For large values of  $\delta d$ , the decrease in  $E$  at each damage event, given by equations (6)  
 592 and (7) respectively, as well as the associated increase in the level of damage, given by  
 593 equation (5), are small. Conversely, for small values of  $\delta d$ , the decrease in  $E$  and  $\eta$  and  
 594 associated increase in  $d$  at each damage event is large. In the first limit, the dissipation  
 595 of the stress in permanent deformations is small. One can expect the emergence of a brit-  
 596 tle creep regime, in which the system remains always near criticality. In the second limit,  
 597 the dissipation of the stress into permanent deformations is large, which can impede elas-  
 598 tic interactions in the system and, by the same fact, the spatial and temporal localiza-  
 599 tion of the deformation (Dansereau, 2016b; Weiss & Dansereau, 2017). In the following,  
 600 the model behaviour is analyzed for damage increment values of 0.1, 0.3, 0.5, 0.7 and 0.9.

## 601 5 Results

### 602 5.1 Mechanical Model Response

603 Here we first describe the overall macroscopic behaviour of the model. This descrip-  
 604 tion is based on simulation results obtained for a specific set of model parameters ( $De_0 =$   
 605  $0.001$ ,  $T_h = 10^{-5}$ ,  $\tilde{\Delta}t = 10^{-10}$ ,  $\alpha = 4$ ,  $\delta d = 0.1$ ), but the conclusions broadly apply  
 606 to a wider range of values. Figure 5a shows the temporal evolution of the model response  
 607 in terms of the macroscopic shear stress, calculated by integrating the shear stress on  
 608 the entire top boundary of the domain, and of the *macroscopic damage increment*, de-

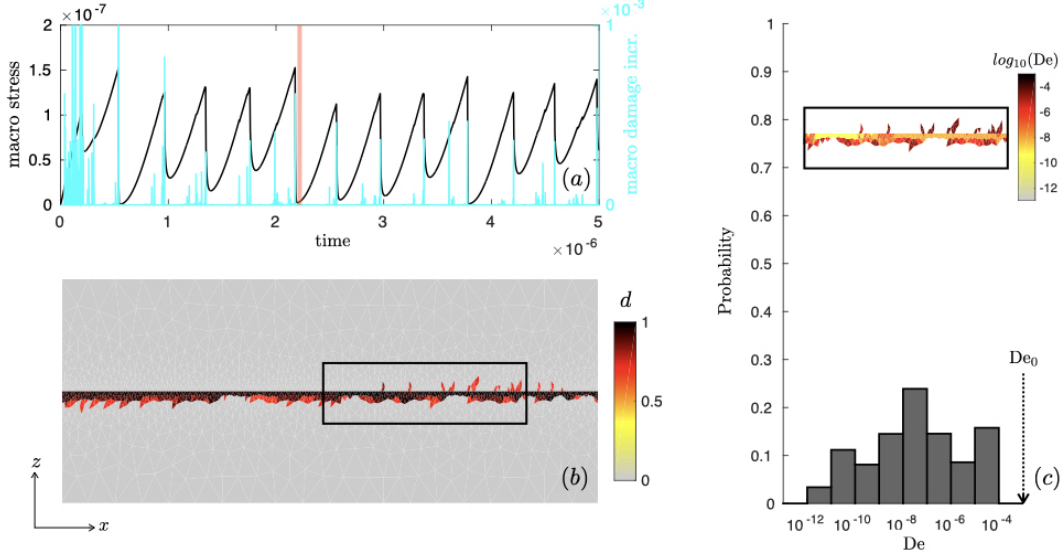


**Figure 5.** (a) Temporal evolution of the macroscopic shear stress (black line) and of the macroscopic damage increment (as defined by eq. 18, cyan line) for a simulation using  $De_0 = 0.001$ ,  $\tilde{\Delta}t = 10^{-10}$ ,  $\alpha = 4$ ,  $\delta d = 0.1$  and  $T_h = 10^{-5}$ . (b) Instantaneous field of the level of damage after the large avalanche of damage events and associated unloading phase indicated by the vertical red line on panel (a). (c) Zoom-in on the instantaneous field of  $De$  (in logarithmic scale) corresponding to the black box indicated on panel (b) and normalized distribution of the instantaneous values of  $De$  for all damaged elements of the domain corresponding to the unloading phase indicated by the vertical red line on panel (a).

609 fined as the local damage increment integrated over all elements  $I$  that are damaged during  
 610 a stress redistribution subiteration  $k$  and over the  $K$  subiterations realized over the  
 611 current model time step,  $n + 1$ :

$$612 \quad \sum_{k=1}^K \sum_{i=1}^I (1 - \delta d)(1 - d_i^{n,k}). \quad (18)$$

613 An animation of this simulation, showing the temporal evolution of the field of damage  
 614 (in logarithmic scale) and of both the macroscopic shear stress and damage increment  
 615 is available as Supporting Information to this paper (see S1). After the initial and al-  
 616 most linear-elastic loading phase, this response is characterized by asymmetric cycles com-  
 617 prised of an either partial or total stress drop (hereinafter called unloading phase) and  
 618 a subsequent healing and stress increase phase (hereinafter called loading phase). Dam-  
 619 age can occur at any moment of the cycle, but unloading phases are generally charac-  
 620 terized by the largest avalanches of damaging events, which can span either a large part  
 621 of or the entire domain (see S1). When the stress drop is partial, it is generally comprised  
 622 of an initial brutal drop associated to a large damage avalanche, followed by a slower re-  
 623 laxation phase, not necessarily associated to significant further damage. This post-rupture,  
 624 or "post-seismic", relaxation results from viscous-like permanent deformations along a  
 625 fault made of highly damaged, hence low viscosity, material. Such behaviour is made pos-  
 626 sible by the rheology proposed above. The occurrence of pre-rupture (akin to foreshocks)  
 627 or post-rupture (akin to aftershocks) damage events varies with the choice of model pa-  
 628 rameters (see section 11 below). However, for all simulations and parameter values cov-  
 629 ered here, the damaging activity localizes at the interface of the two layers (mostly within  
 630 the lower plate, see figure 5b), a behaviour that is not prescribed but that arises natu-  
 631 rally due to the forcing condition applied at the bottom of the lower layer and to the small

632 difference in elastic modulus assigned to each layer. Consequently, the deformation of  
 633 the system is also highly localized at this interface. Figure 5b also indicates that dam-  
 634 age is heterogeneously distributed along the interface. As a consequence of the prescribed  
 635 coupling between  $d$  and both the  $E$  and  $\eta$  (see eq. 2 and 3), this heterogeneity in dam-  
 636 age leads to a large heterogeneity in the value of the relaxation time, or equivalently of  
 637 the effective De number, along the interface. As indicated by the distribution shown in  
 638 Figure 5c, the values of De associated with damaged grid elements indeed span several  
 639 orders of magnitude. The lowest values of De are obtained at the end of unloading phases  
 640 and re-increase as the system heals towards the end of loading phases.

641 However, it is worth noting that, over the range of parameter values explored here,  
 642 the vicinity of the interface remains relatively highly damaged at all times (see S1) and  
 643 never completely heals: a behaviour that is expected in the context of active faults. By  
 644 the same fact, and because the simulations are initialized from a uniformly undamaged  
 645 state ( $d = 0$  everywhere), the behaviour during the first loading-unloading cycle is very  
 646 different from the subsequent ones : the damaging activity is relatively much higher be-  
 647 cause the damaged zone is created from scratch while over all subsequent cycles, the in-  
 648 terface is already damaged to a relatively large degree. In all further analyses of the model  
 649 behaviour, this first loading-unloading cycle is therefore discarded.

## 650 5.2 Convergence and Numerical Efficiency

651 Here we verify that the macroscopic behaviour of the model converges with increas-  
 652 ing temporal resolution. To do so, for the three identified values of  $De_0$  (see section 4.1),  
 653 simulations are run with five different values of the (adimensional) time step,  $\tilde{\Delta}t$ . All of  
 654 these simulations use the same value of the damage increment ( $\delta d = 0.1$ ) and of the  
 655 damage parameter ( $\alpha = 4$ ) and are initiated with the same field of noise on the cohe-  
 656 sion. We explored a range of values of the healing time for these simulations, and retained  
 657 the one value that produced the most physically sound results for each set of simulations  
 658 with a given  $De_0$  value (see section 5.3.1).

659 Figure 6 shows the temporal evolution of the model response in terms of the macro-  
 660 scopic stress (a) and of the macroscopic damage increment (b), defined as in eq. (18).  
 661 It indicates that the largest value of the time step explored here leads to a pathologi-  
 662 cal model response. This is expected, as this  $\tilde{\Delta}t$  value approaches the order of magni-  
 663 tude of the main period of the loading-unloading cycles : this temporal resolution there-  
 664 fore does not allow resolving the progressive propagation of the damage in the system,  
 665 nor the sharp stress drop associated with each macroscopic rupture. For smaller values  
 666 of the time step, the model response converges well in terms of the main frequency and  
 667 amplitude of the macroscopic stress variations when increasing the temporal resolution.  
 668 It is also the case for the macroscopic variations in the deformation of the system (not  
 669 shown) and in the damage increment.

670 To robustly test the convergence of the model response, we use a single metric that  
 671 combines these three different pieces of information : the local damage increments and  
 672 the resulting redistribution of the stress and of strains over the entire system. This is  
 673 the elastic energy released within the system due to the propagation of damage,  $E_{brit}$ ,  
 674 the temporal evolution of which is shown in figure 6c. The distribution of this energy  
 675 can be directly related to that of acoustic emissions associated to the micro-fracturing  
 676 of rocks (e.g., Amitrano, 2003) and can therefore serve as a proxy for the seismic signal  
 677 recorded at the geophysical scale. At each current ( $n+1$ ) model time step,  $E_{brit}$  is es-  
 678 timated as

$$679 E_{brit}^{(n+1)} = \sum_{i=1}^I \frac{A_i}{A_{tot}} \left( \sigma_i^{(n+1,0)} : \varepsilon_i^{(n+1,0)} - \sigma_i^{(n+1,K)} : \varepsilon_i^{(n+1,K)} \right), \quad (19)$$

680 where  $i$  designate each element,  $I$ , the total number of elements over the domain,  $A_i$  the  
 681 area of each element and  $A_{tot}$ , the area of the entire domain. The superscripts  $n + 1, 0$

682 and  $n + 1, K$  refer respectively to the stress and strain values before and at the end of  
 683 the avalanche of damaging events, which takes a total of  $K$  stress redistribution sub-  
 684 iterations. To compare simulations using different time steps,  $E_{brit}$  is normalized by  $\tilde{\Delta}t$ .  
 685 In agreement with the observed convergence in the variations of the macroscopic stress,  
 686 deformation and damage increment, figure 6d clearly shows that the shape of the prob-  
 687 ability density function (PDF) of the normalized  $E_{brit}$  stabilizes over the three small-  
 est values of time step explored here.

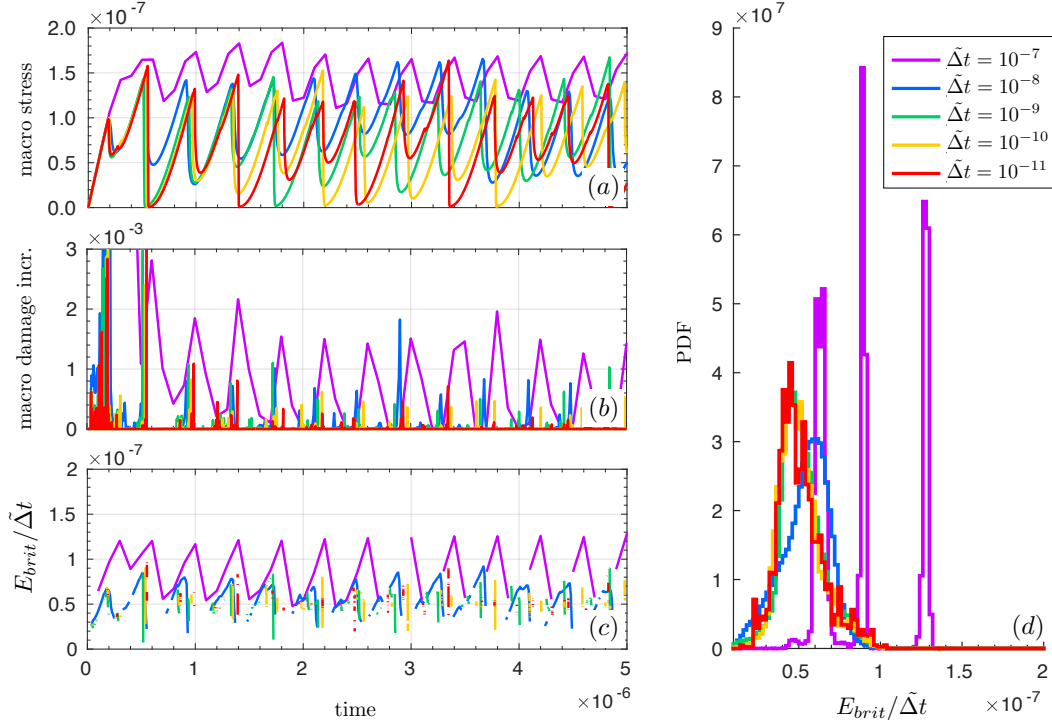


**Figure 6.** Temporal evolution of (a) the macroscopic stress, (b) the macroscopic damage increment and (c) the macroscopic elastic energy released due to the propagation of damage within the system, normalized by the time step  $\tilde{\Delta}t$ , for simulations using  $De_0 = 0.001$ ,  $\alpha = 4$ ,  $\delta d = 0.1$ ,  $T_h = 10^{-5}$  and  $\tilde{\Delta}t = 10^{-11}, 10^{-10}, 10^{-9}, 10^{-8}, 10^{-7}$  (corresponding to  $\Delta t = 10^4$  s,  $10^5$  s,  $10^6$  s,  $10^7$  s,  $10^8$  s) (d) Probability density function of  $E_{brit}/\tilde{\Delta}t$ .

688

689 Simulations ran with  $De_0 = 0.1$  and  $De_0 = 10$ , the same values of  $\delta d$  (0.1) and  
 690 of the damage parameter,  $\alpha$ , (4) and values of healing time of  $T_h = 10^{-4}$  and  $T_h =$   
 691  $10^{-3}$  respectively show that a similar convergence is retrieved in both cases over a range  
 692 of values of  $\tilde{\Delta}t$  (see figure C1 of Appendix C). These values are summarized in table 3:  
 693 the red ones indicating a non-converged model response. The comparison of these val-  
 694 ues across the three  $De_0$  explored here suggests that the time step should be chosen such  
 695 that  $\frac{\Delta t}{T} \lesssim 10^{-8}$  to ensure a fully converged and therefore physically meaningful model  
 696 behaviour. The time step values corresponding to each  $De_0$  value and retained for the  
 697 sensitivity analyses on the other model parameters are indicated in green in table 3.

698 We further compare the simulations presented in figure 6 in terms of CPU and real  
 699 simulation time. Each simulation was ran for a fixed (adimensional) total time of  $5.0 \cdot$   
 700  $10^{-6}$ , which represents, in dimensional equivalent, 160 years of evolution of the system.  
 701 With the specific choice of model parameters employed in this particular simulation, each  
 702 loading-unloading cycle covers about 12 years. The model response converges for time

$T$ (s)	$De_0$	$\Delta t$ (s)	$\tilde{\Delta}t$	$t_h$ (s)	$T_h$
$10^{15}$	0.001	$10^4$	$10^{-11}$	$10^8$	$10^{-7}$
		$10^5$	$10^{-10}$	$10^9$	$10^{-6}$
		$10^6$	$10^{-9}$	$10^{10}$	$10^{-5}$
		$10^7$	$10^{-8}$	$10^{11}$	$10^{-4}$
		$10^8$	$10^{-7}$		
$10^{13}$	0.1	$10^3$	$10^{-10}$	$10^8$	$10^{-5}$
		$10^4$	$10^{-9}$	$10^9$	$10^{-4}$
		$10^5$	$10^{-8}$	$10^{10}$	$10^{-3}$
		$10^6$	$10^{-7}$	$10^{11}$	$10^{-2}$
		$10^7$	$10^{-6}$		
$10^{11}$	10	$10^2$	$10^{-9}$	$10^8$	$10^{-3}$
		$10^3$	$10^{-8}$	$10^9$	$10^{-2}$
		$10^4$	$10^{-7}$	$10^{10}$	$10^{-1}$
		$10^5$	$10^{-6}$	$10^{11}$	$10^0$
		$10^6$	$10^{-5}$		

**Table 3.** Values of the deformation timescale,  $T$ , the model time step,  $\Delta t$ , and healing time,  $t_h$ , explored in the present sensitivity experiments, with their adimensional counterpart : respectively,  $De_0$ ,  $\tilde{\Delta}t$  and  $T_h$ . For each value of  $De_0$ , the values of  $\Delta t$  (or  $\tilde{\Delta}t$ ) for which the model response is not fully converged are indicated in red. The value of  $\Delta t$  (or  $\tilde{\Delta}t$ ) retained for the sensitivity analyses on  $T_h$ ,  $\delta d$  and  $\alpha$  is indicated in green. For each  $De_0$  value also, the optimal value of  $t_h$  (or  $T_h$ ) retained for the sensitivity analyses on  $\alpha$  and  $\delta d$  are indicated in green.

703 step values of  $\tilde{\Delta}t = 10^{-11}, 10^{-10}$  and  $10^{-9}$  (or  $\Delta t = 10^4, 10^5$  and  $10^6$  s), which are  
704 equivalent to about 1/10, 1 and 10 days respectively. For these three time steps, and for  
705 the spatial resolution described in section 3, the calculated CPU time is of about 25, 3  
706 and 0.4 hours respectively (see figure 7). Considering that each simulation ran sequen-  
707 tially on a personal DELL computer equipped with 2.40 GHz Intel Xeon processors, these  
708 computational times demonstrate that the present numerical scheme makes it possible  
709 to run long-term simulations in the context of faults that cover several loading-unloading  
710 cycles in very reasonable simulation times. It is also interesting to note that, for the same  
711 three time steps for which convergence of the macroscopic model response is obtained,  
712 the calculated CPU time scales linearly with  $\frac{1}{\tilde{\Delta}t}$ , while it does not scale linearly for larger  
713 time steps ( $\tilde{\Delta}t > 10^{-9}$ ). This indicates that for the smallest three  $\tilde{\Delta}t$  values, the num-  
714 ber of steady-state stress redistribution subiterations performed at each time step is nearly  
715 constant and hence does not depend on the model time step. Conversely, for larger  $\tilde{\Delta}t$ 's,  
716 the system is driven further out of equilibrium at each time (i.e., deformation) increment.  
717 The number of subiterations required for the stresses to be redistributed over the domain  
718 and to become sub-critical again then increases significantly with  $\tilde{\Delta}t$ , thereby reducing  
719 the gain in computational time.

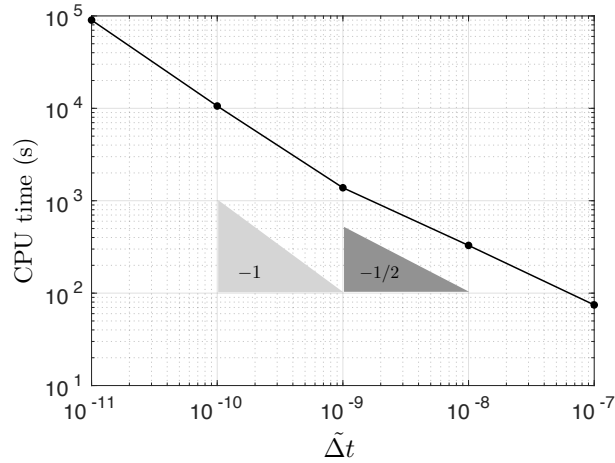


**Figure 7.** CPU time as a function of the (adimensional) model time step, for simulations using  $De_0 = 0.001$ ,  $\alpha = 4$ ,  $\delta d = 0.1$ , and  $T_h = 10^{-5}$  (see figure 6). Each simulation ran on a single (2.40 GHz Intel Xeon) processor on a personal DELL computer.

720

### 5.3 Sensitivity Analyses

721

#### 5.3.1 Healing Time, $T_h$

722

723

724

725

726

727

728

729

730

731

To investigate the effect of healing in the model, we compare the macroscopic stress-strain time series and the power spectral density (PSD) of the elastic energy released within the system during the propagation of damage,  $E_{brit}$  (see figure 8), for simulations using  $De_0 = 0.001, 0.1$  and  $10$  and four different values of the time for healing, corresponding to dimensional times of  $t_h = 10^8$  s,  $10^9$  s,  $10^{10}$  s and  $10^{11}$  s. All simulations use  $\alpha = 4$  and  $\delta d = 0.1$  and a value of the time step that ensures the convergence of the model response for each  $De_0$  value (see table 3). To account for the adjustment of the system following the first rupture, the first loading-unloading cycle is discarded when computing the PSD. Each curve shown on figure 8 is the average of 5 PSDs, on which a running mean centred over a window of 5 frequency values is applied.

732

733

734

735

736

737

738

739

740

741

742

The results clearly indicate that the prescribed time of healing controls the frequency of the loading-unloading cycles in the model: the larger the healing time, the lower the frequency. However in all of the simulations analyzed, the frequency associated to the prescribed healing time, indicated by the vertical lines on figure 8, does not correspond to the frequency of the loading-unloading cycles, but is systematically one or several orders or magnitude lower. This discrepancy is consistent that the interface always remains relatively highly damaged (see animation in Supporting Informations): less time is therefore required to re-initiate an avalanche of damaging events than it would be necessary if the system had completely heal. The discrepancy increases with the value of  $De_0$ , in agreement with a more elastic behaviour at high  $De_0$  number, i.e. a lower contribution from viscous dissipation that delays the reloading of the system.

743

744

745

746

747

748

749

Another tendency in the model behaviour emerges. For all values of  $De$  explored here, large values of the healing time (slow healing) lead to a  $E_{brit}$  release, or equivalently a damaging activity, that concentrates around a narrow range of low frequencies: the PSD is therefore flat for high frequencies. The corresponding stress-strain curves indicates that the stress is very rapidly and completely dissipated at each unloading (damaging) event. This behaviour can be explained by the fact that these large values of healing time approach the value of the bulk relaxation time (i.e, the relaxation time of undamaged el-

750 ements, or  $De_0$ ). Healing is therefore too slow relative to the dissipation of the stress to  
 751 play a significant role in the dynamics of the system.

752 Conversely, for low values of the healing time (fast healing), the PSD is flat for low  
 753 frequencies, with the activity concentrated around a narrow range of high frequencies,  
 754 and the stress is very rapidly but only partially dissipated at each damaging event: heal-  
 755 ing dominates the dynamics as  $T_h$  approaches the value of the relaxation time for the  
 756 stresses over the most damaged elements in the system (i.e.,  $De_{min}$ ). This value tends  
 757 to decrease inversely to  $T_h$ , as indicated by the coloured dotted lines on figure 8b.

758 For intermediate values of  $T_h$  and the two lowest values of  $De$  explored here (see  
 759 figure 8a to d), the slope of the PSDs indicates the presence of correlations in the tem-  
 760 poral evolution of  $E_{brit}$  (or, by extension, of the damaging activity). Such temporal cor-  
 761 relation or clustering is systematically observed for seismic tremors in subduction zones  
 762 and covers large spectrum of time scales, from hours to years (e.g., Idehara et al., 2014;  
 763 Frank et al., 2016; Poiata et al., 2021). Therefore, for each investigated  $De$  value, we iden-  
 764 tify an "optimal" healing time as the value of  $T_h$  for which these correlations span the  
 765 largest range of frequencies. It is important to note however, that the frequency at which  
 766 spatial correlations emerge in the system is upper bounded in all simulations due to the  
 767 finite dimension of the domain and the spatial resolution of the mesh. An intrinsic min-  
 768 imum time required to load the system can indeed be estimated, that depends only on  
 769 the mechanical strength (the ratio  $C_0/E_0$ ) and the spatial discretization of the model.  
 770 It corresponds to the time it takes to load an initially undamaged system until the first  
 771 damage event occurs, if all of the deformation is accommodated over a single single grid  
 772 element. Figure 8b shows that the frequency associated to this time, indicated as  $\frac{1}{t_{loading}}$   
 773 indeed marks the transition to a flat PSD at higher frequencies (for the other two sys-  
 774 tems, the time step employed is too large and does not allow exploring the model be-  
 775 haviour up to this frequency). For the "optimal"  $T_h$  values, corresponding to  $t_h = 10^{10}$   
 776 s for  $De = 0.001$  (figure 8a, b blue curve) and  $t_h = 10^9$  s for  $De = 0.1$  (figure 8c, d  
 777 green curve), the times associated with the loading, the relaxation of the stresses over  
 778 damaged elements and the healing of these elements are such that the three processes  
 779 interact and give rise to temporal correlations in the system that span a wide range of  
 780 time scales. Interestingly, the stress-strain behaviour of the model in these cases is char-  
 781 acterized by loading-unloading cycles in which the stress is sometimes partially and more  
 782 gradually dissipated and sometimes completely and drastically dissipated.

783 The optimal value of  $T_h$  decreases as the value of  $De_0$  increases, indicating that sys-  
 784 tems that are more elastic-solid like (large relaxation time,  $\lambda$ ) or characterized by a faster  
 785 dynamics (small deformation time,  $\frac{L}{U}$ , either due to a small horizontal extent,  $L$  or a fast  
 786 loading velocity,  $U$ ) must encompass faster healing mechanisms for these interactions to  
 787 take place.

788 However, for the largest  $De$  value used here (see figure 8e, f), temporal correlations  
 789 in the damaging activity are restricted to a small range of time scale and that, for all  
 790 of the  $T_h$  values explored, which we consider as lying in a realistic range in the context  
 791 of faults. The associated macroscopic stress-strain behaviour is characterized by regularly-  
 792 spaced, almost instantaneous (as opposed to transient) and complete unloading phases,  
 793 akin to the stick-slip behaviour observed in block-slider experiments. In the context of  
 794 slow earthquakes, this suggests that fault systems that are either very brittle (as near  
 795 the surface), small in extent, or loaded too rapidly cannot host the complex spatio-temporal  
 796 interactions that give rise to the observed transient deformations.

797 In the remaining sensitivity experiments (next section), we therefore leave the case  
 798 of  $De = 10$  aside and concentrate on simulations using  $De = 0.001$  and  $De = 0.1$ .  
 799 The optimal values of  $T_h$  identified for these two cases are indicated in green in table 3  
 800 and used by default in all simulations.

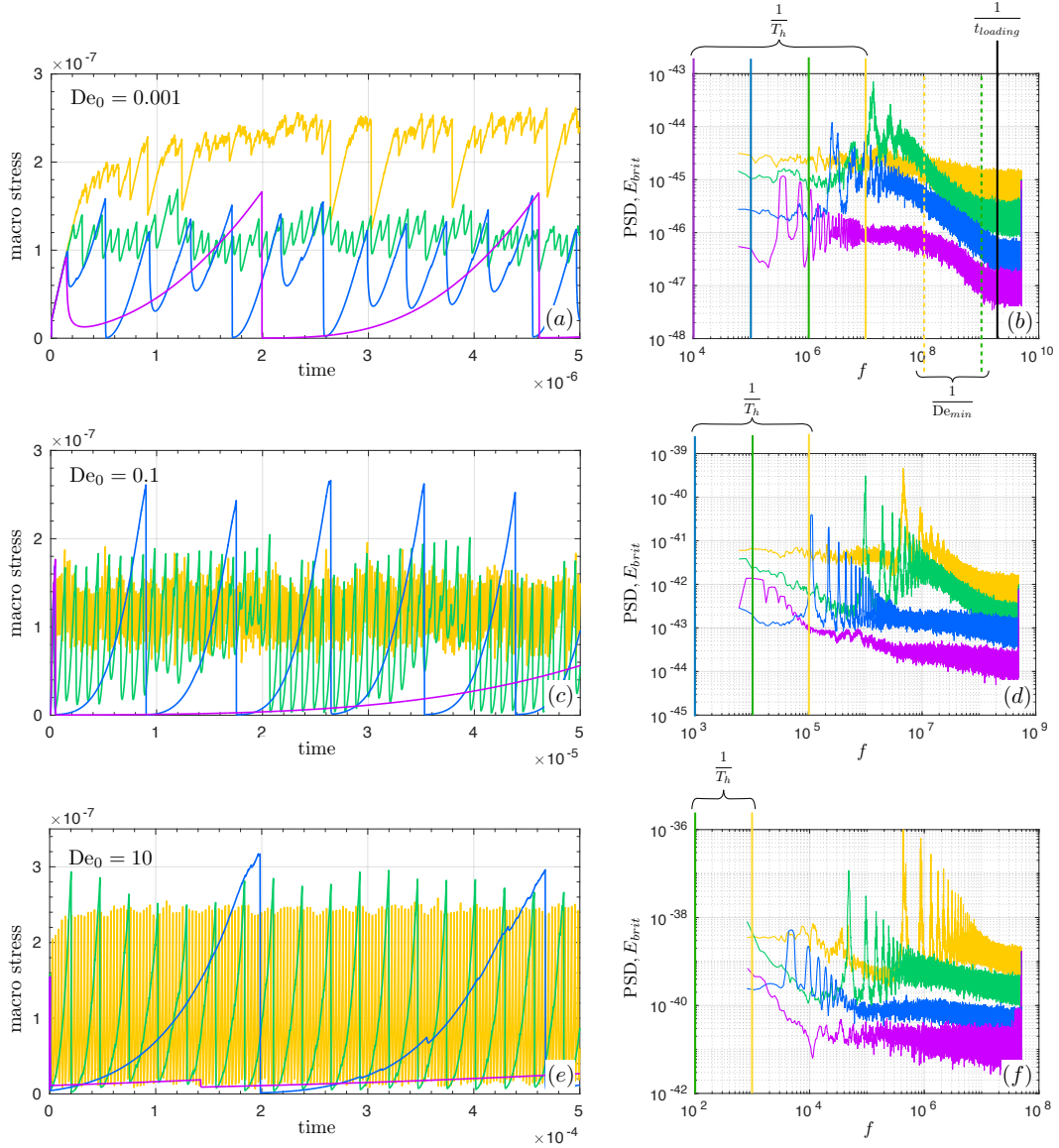


**Figure 8.** (a, c, d) Time series of the macroscopic stress and (b, d, f) power spectral density of the  $E_{brit}$  time series for simulations using (a, b)  $De_0 = 0.001$  ( $\tilde{\Delta}t = 10^{-10}$ ), (c, d)  $De_0 = 0.1$  ( $\tilde{\Delta}t = 10^{-9}$ ) and (e, f)  $De_0 = 10$  ( $\tilde{\Delta}t = 10^{-8}$ ) and four adimensional values of the prescribed time of healing, corresponding to dimensional values of  $t_h = 10^8$  s (yellow),  $10^9$  s (green),  $10^{10}$  s (blue) and  $10^{11}$  s (purple curve). All simulations use  $\alpha = 4$  and  $\delta d = 0.1$ . Each PSD curve is an average of 5 PSD calculated for 5 simulations initiated with different realizations of the noise on  $C$  and on which a running mean centred over a window of 5 frequency values is applied. The vertical lines on the PSDs indicate, when these frequencies fall within the range of frequencies covered in the simulations, the frequencies associated with the four adimensional values of the prescribed time of healing,  $1/T_h$  (plain coloured lines), the minimum time required to load the system,  $1/t_{loading}$  (plain black line), and the relaxation time associated with the most highly damaged elements in the system,  $1/De_{min}$  (dashed coloured lines).

### 5.3.2 Damage Parameter, $\alpha$ , and Damage Increment, $\delta d$

The last set of sensitivity experiment focuses on the brittle versus ductile character of the model behaviour. As the parameters  $\alpha$  and  $\delta d$  both regulate the rate at which the mechanical strength decreases locally and the behaviour changes from elastic solid-like and viscous fluid-like as a function of the level of damage, we expect their effect in this regard to be closely related. We therefore run a set of sensitivity experiments in which both parameters are varied simultaneously. The results of these experiments for the case of  $De_0 = 0.001$  ( $\tilde{\Delta}t = 10^{-10}$  s and  $T_h = 10^{-5}$  s) and  $De_0 = 0.1$  ( $\tilde{\Delta}t = 10^{-9}$  s and  $T_h = 10^{-4}$  s) are presented here.

We recall that for large values of  $\delta d$ , the local decrease in the elastic modulus,  $E$ , and apparent viscosity,  $\eta$ , at each damaging event is small. Conversely, for small values of  $\delta d$ , the local decrease in both  $E$  and  $\eta$  is large. Small values of  $\alpha$  lead to a small decrease in the relaxation time,  $\frac{\eta}{E}$ , at each damaged element (the damaged material retains stresses longer), while large values of  $\alpha$  lead to a large decrease in  $\frac{\eta}{E}$  (stresses are dissipated more readily).

#### Damage Increment, $\delta d$

Time series of the macroscopic stress (see figure 9 and 10, left panels) show that for all values of  $\alpha$ , increasing  $\delta d$  decreases the amplitude of the macroscopic stress drop associated with each unloading phase. As the stress is then never completely released at each loading-unloading cycle but stabilizes around a non-zero value, the loading time required for critical values of stress to be reached is reduced and the frequency of each cycle is thereby increased. For large values of  $\delta d$ , the PDF of the macroscopic damage increment, defined as in equation (18), is a truncated power law that is confined to small values of damage increment (see figure 9, right panels, which indicates that damage and deformation take place through isolated events, with small spatial extents).

Conversely, as  $\delta d$  is decreased, the amplitude in the variations of the macroscopic stress and the length of the loading-unloading cycles is increased. The unloading phases are characterized by sharper stress drops, indicating a more brittle behaviour. The distributions of the macroscopic damage increment are shifted towards larger values of damage increments.

#### Damage Parameter, $\alpha$

For a given value of  $\delta d$ , increasing the value of  $\alpha$  also induces larger macroscopic stress drops, lower frequency loading-unloading cycles and larger values of the macroscopic damage increment. Another effect of increasing  $\alpha$  is that the stress relaxation and re-increase in the vicinity of each stress minimum is more progressive in time, consistent with a more rapid decrease in the viscosity of the material at the onset of damaging and a more viscous fluid-like, i.e, dissipative, behaviour. The inverse is true when decreasing  $\alpha$ : the macroscopic behaviour is more brittle-like, with smaller but quasi-instantaneous stress relaxation phases and rapid, quasi-elastic stress loading phases.

#### Limit Cases

For virtually all values of  $\alpha$ , large values of  $\delta d$  give rise to a macroscopic stress-strain behaviour in which, after the initial elastic loading phase, where is no stress relaxation but rather a slow stress increase akin to the behaviour of a strain hardening creeping material. In this case, the PDFs of the macroscopic damage increment are upper-truncated power laws.

For small values of  $\alpha$  and small values of  $\delta d$  (e.g., see figure 9a or 10a for  $\alpha = 2$  and  $\delta d = 0.1$ ), the macroscopic behaviour, showing very sharp but small amplitude stress drops at each loading-unloading cycle, is reminiscent of a quasi-brittle material in which the stress relaxation through viscous-like deformation is insignificant. Each stress un-

loading phase is associated with a large avalanche of damage events that spans the entire domain. This explains the sharp mode in the PDF of the macroscopic damage increments at large increment values, which indicates that a characteristic avalanche size emerges, associated to a finite-size effect.

For large values of  $\alpha$  and small values of  $\delta d$  (e.g., see figure 9 or 10, d and e, for  $\alpha = 6$  or 8), the dissipation of stresses at the onset of damaging is the largest and the material becomes readily fluid-like. The stress is regularly and completely dissipated at each loading-unloading cycle. Local damage events are suppressed, which is expressed by the translation of the PDF of macroscopic damage increments towards larger increment values. The elastic redistribution of stresses are inherited and, therefore, the spatio-temporal correlations in the damaging activity are limited, which reduces the horizontal extent of avalanches and explains the appearance of broad modes in the PDFs of damage increments as well as their departure from a power law.

For intermediate values of  $\alpha$  (e.g.,  $\alpha = 3, 4$ , see figure 9 or 10, b and c) and small values of  $\delta d$  (0.1, 0.3, 0.5), the distribution of damage increments can be well-fitted with a power-law, that extends at large damage increment values. This suggests that the model simulates a mechanical behaviour that is, at least to some extent, scale-invariant. Unloading phases are characterized by stress drops of variable amplitudes, which are initially almost-instantaneous and then followed by a transient period.

## 6 Discussions

In this section, we further discuss what the model in its current state is able and not able to simulate in the context of fault deformation and slow earthquakes. To do so, we investigate the simulated dynamical behaviour for one specific case in which only  $\delta d$  is varied and all other mechanical parameters are identical. This simulation is identified by the black box on figure 10c and uses  $De_0 = 0.1$ ,  $\alpha = 4$ , with the corresponding default values of  $\tilde{\Delta}t$  and  $T_h$  (see table 3). In particular, we analyze the temporal evolution of pointwise displacements and velocities at the top boundary of the domain, which constitute proxies for the surface displacements and velocities as measured by Global Positioning Systems (GPS). In the following, we focus on the horizontal displacement and velocity at one point, the top left corner of the domain, which is furthest from the top right corner and therefore less influenced by the prescribed boundary condition there ( $u_x = 0$ ). It is important to note that on figures 11a, b and e, f, the prescribed velocity forcing,  $U$ , is subtracted from the recorded horizontal surface velocity. Also, the first few loading-unloading cycles are omitted from the analysis, as they are susceptible to carry the signature the first (outlier) rupture event.

The comparison of two simulations in which only the damage increment is varied between 0.1 and 0.5, summarized in figure 11, suggests that over a certain range of mechanical parameters the model can reproduce two different types of mechanical behaviour, which are more analogous to classical earthquakes and slow slip events, respectively. In the first case ( $\delta d = 0.1$ , left panels), the macroscopic shear stress on the top boundary indeed shows very rapid and large-amplitude release phases followed by short post-seismic stress relaxation phases and much longer reloading phases (see figure 11a). Each brutal stress release event is associated with a sharp reversal of the surface horizontal ( $x$ -) velocity and an equally sharp drop in the surface horizontal displacement (see figure 11c), which suggests a strong decoupling of the upper and lower plates following large damage events, reminiscent of classical earthquakes. In the second case ( $\delta d = 0.5$ , right panels), the asymmetry in the loading-unloading cycles is much less pronounced (see figures 11b and d): the stress is much more progressively dissipated at each loading-unloading cycle, which is accompanied by lower amplitude variations of the surface velocity and a progressive decrease in the surface displacement, reminiscent of slow slip events (e.g., Rogers & Dragert, 2003; Radiguet et al., 2016).

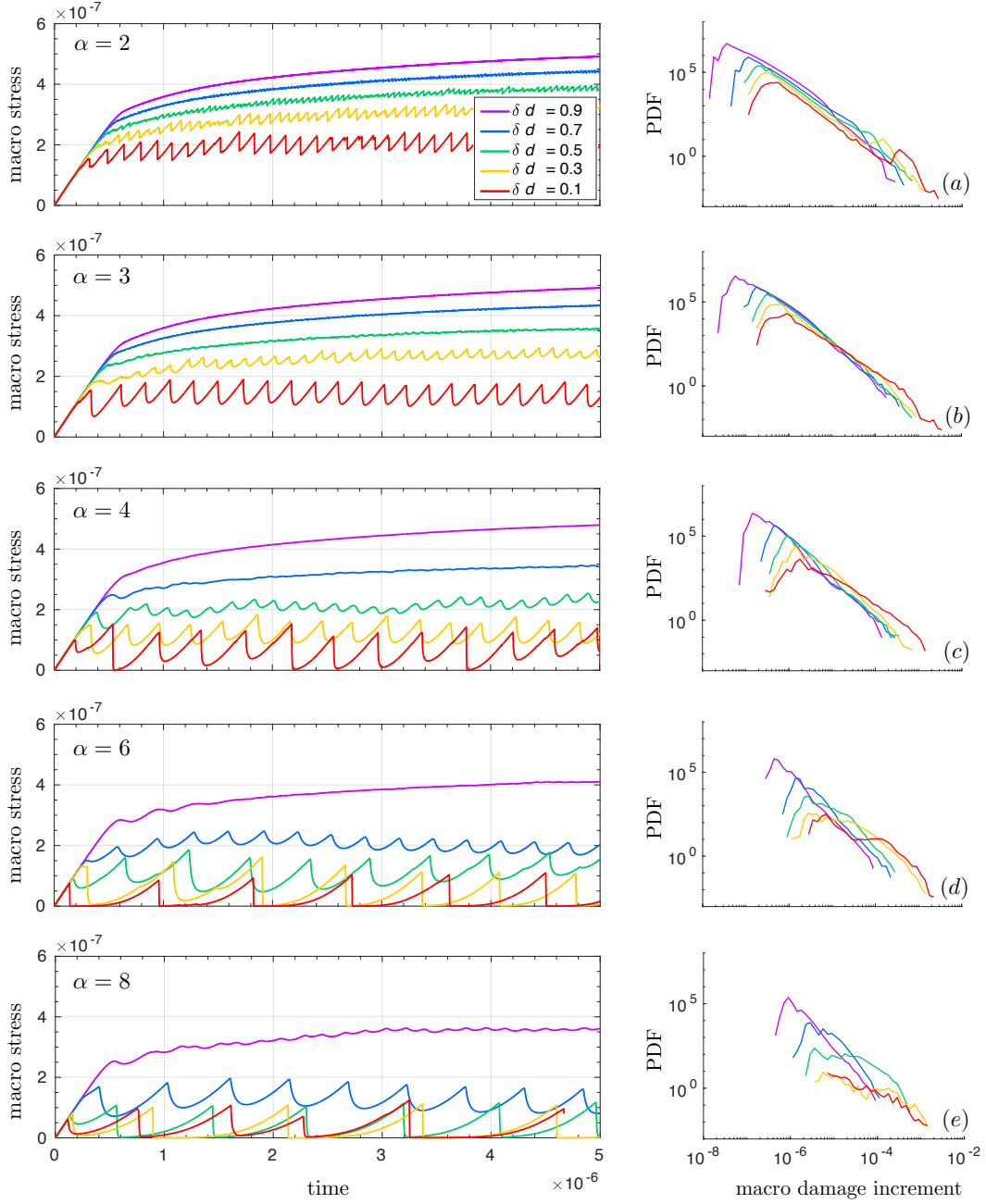


**Figure 9.** Time series of the macroscopic stress (left panels) and probability density function of the macroscopic damage increment (right panels) for  $De_0 = 0.001$  ( $\tilde{\Delta}t = 10^{-10}$ ,  $T_h = 10^{-5}$ ) and  $\delta d = 0.1, 0.3, 0.5, 0.7, 0.9$  and (a)  $\alpha = 2$ , (b)  $\alpha = 3$ , (c)  $\alpha = 4$ , (d)  $\alpha = 6$ , (e)  $\alpha = 8$ .

901 The damaging activity also differs between the two cases (see figures 11c, d). In  
 902 the first, fewer damage events are recorded over the same simulation time. The damag-  
 903 ing activity concentrates over large events that either precede (as in foreshocks) or co-  
 904 incide with stress release phases. In the second case, the damaging activity is more sym-  
 905 metric with respect to unloading phases, with damaging event both preceding (as in fore-  
 906 shocks) and following (as in aftershocks) stress release events.

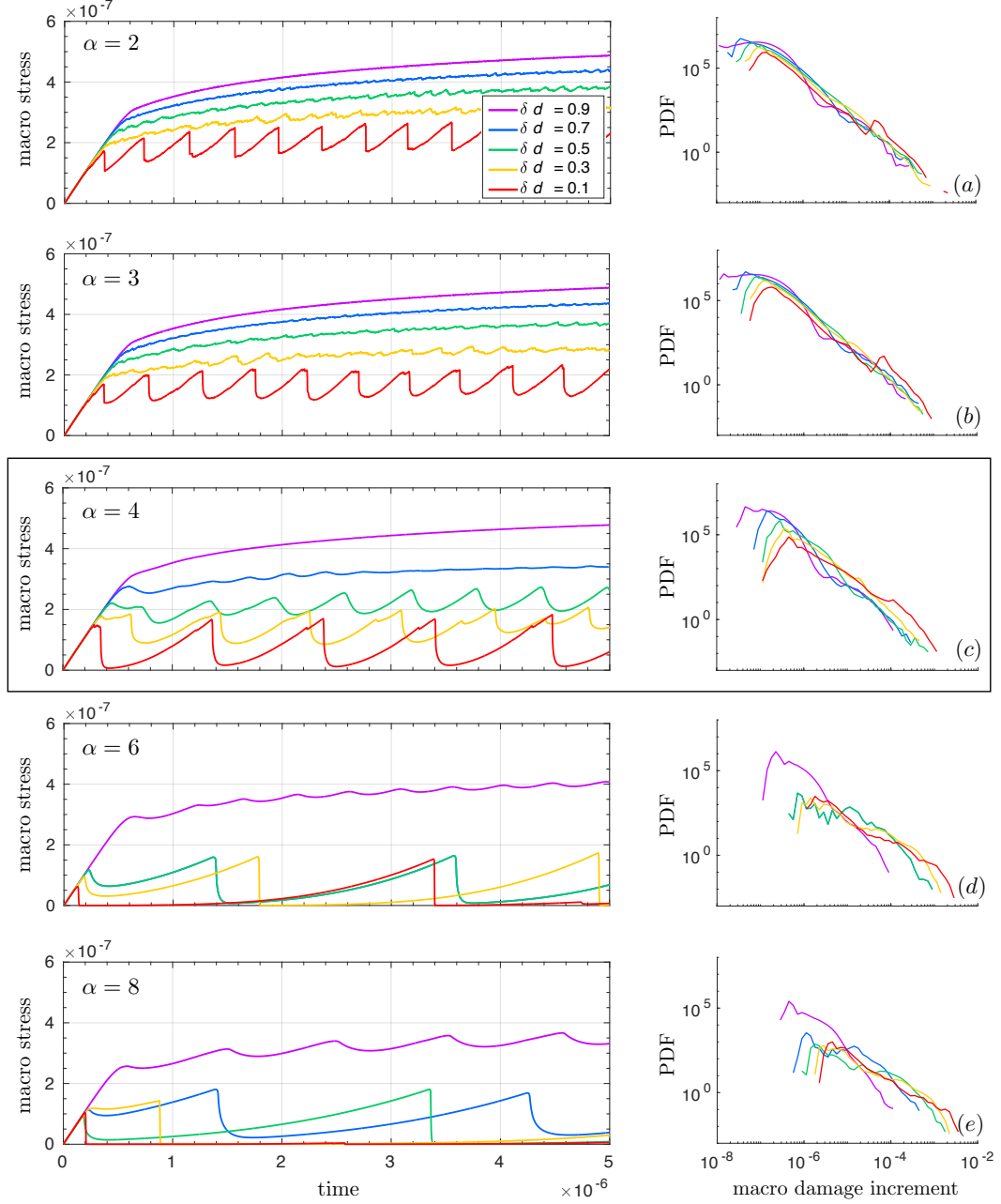


**Figure 10.** Time series of the macroscopic stress (left panels) and probability density function of the macroscopic damage increment (right panels) for  $De_0 = 0.1$  ( $\tilde{\Delta}t = 10^{-10}$ ,  $T_h = 10^{-5}$ ) and  $\delta d = 0.1, 0.3, 0.5, 0.7, 0.9$  and (a)  $\alpha = 2$ , (b)  $\alpha = 3$ , (c)  $\alpha = 4$ , (d)  $\alpha = 6$ , (e)  $\alpha = 8$ .

907 We further analyze the temporal evolution of the surface horizontal velocity during  
 908 each loading-unloading cycle, that is, over a period of time that starts at the onset  
 909 of each stress release phase and extends until the next phase, as delimited by the dashed  
 910 lines and arrows on figures 11a, b and c, d. In the first case, using  $\delta d = 0.1$ , the model  
 911 reproduces a power law decay of the velocity of the form

$$912 \quad V(t) \sim \frac{1}{t^p}, \quad (20)$$

913 where  $t$  is the time after the onset of stress release, and the exponent  $p$  is slightly smaller  
 914 than 1 (see figure 11e). This behaviour is akin to the observed Omori-like decay of post-  
 915 earthquake surface velocities (Perfettini & Avouac, 2004; Savage et al., 2005; Ingleby &  
 916 Wright, 2017; Periollat et al., 2022), which suggests that long-term temporal correlations  
 917 in the system control the evolution of post-earthquake surface velocities in the case of  
 918 classical earthquakes. It is important to note however that in the present case, this trend  
 919 spans a little more than two orders of magnitude, which is much less than what the ob-  
 920 servations cover. This is due to the fact that, for the purpose of this paper, we have cho-  
 921 sen our mechanical parameters (in particular the ratio  $C_0/E_0$ , which controls the sys-  
 922 tem loading time, see section 5.3.1) to be consistent with the typical recurrence time of  
 923 slow earthquakes, not with the larger time scales associated with classical earthquakes.

924 In the second case, using  $\delta d = 0.5$ , the post-rupture surface velocities are signif-  
 925 icantly smaller than in the previous case, and remain relatively stable for some time, be-  
 926 fore slowly decaying at larger timescales (see figure 11f). Such behaviour is similar to  
 927 what is observed during some largest SSEs for which the details of the displacement time  
 928 series can be resolved (Cotte et al., 2009; Radiguet et al., 2012).

929 These results suggest that the proposed modeling framework could be able to re-  
 930 produce both slow earthquakes and classical earthquakes. Numerically at least, it can  
 931 do it because it is efficient enough.

932 One important point however is that, not over the entire range of model param-  
 933 eter values but over the range that generates a mechanical behaviour most analogous to  
 934 slow and classical earthquakes, the model definitely exhibits a pseudo-periodic behaviour.  
 935 While it might be consistent with slow earthquakes (e.g., Dragert et al., 2001; Cotte et  
 936 al., 2009; Radiguet et al., 2016), such behaviour is less consistent with classical earth-  
 937 quakes. While recent studies have found that large (classical) earthquakes occur more  
 938 regularly than a purely random process (e.g., T. Williams et al., 2019; Griffin et al., 2020),  
 939 the temporal evolution of classical earthquakes in general is indeed more intermittent  
 940 and their recurrence time, hardly predictable (e.g., Gardner & Knopoff, 1974; Michael,  
 941 2011). We however believe that more variability in recurrence times and stress drop mag-  
 942 nitudes and an intermittent behaviour covering a wider range of time scales could be ob-  
 943 tained by incorporating additional physical components to the model. Leaving aside the  
 944 more complex dynamics of fluids aspects, we list some simple and logical options below.

945 The first consists in moving to a healing law that does not prescribe a unique, con-  
 946 stant healing time. Such a law would be in better agreement with available observations.  
 947 Measurements of relative seismic velocity changes after majors earthquakes indeed in-  
 948 dicate a healing rate that is not constant but decrease in time after the main shock, sug-  
 949 gesting that the damaged region within the fault regains strength rapidly in the early  
 950 stage of the interseismic period and progressively more slowly in the later stages (e.g.,  
 951 Li & Vidale, 2001; Brenguier et al., 2008). In the present model, this behaviour could  
 952 be parameterized through a logarithmic healing law that does not include any charac-  
 953 teristic time for healing but that instead depends locally on the time elapsed since the  
 954 last damage event. Such a law would agree with the aging version of the rate-and-state  
 955 interface model of (Ruina, 1983), which imply that the surfaces that are in contact and  
 956 at rest strengthen logarithmically and would allow the system to evolve in a less deter-  
 957 ministic manner.

958 The second consists in accounting for a representation of the rheological stratifi-  
 959 cation of subduction zones, which is known to depend strongly on temperature (e.g. Pea-  
 960 cock, 2009) and therefore on depth. In the present 2-dimensional, idealized numerical  
 961 experiments, this stratification could be coarsely accounted for by allowing the bulk, un-  
 962 damaged viscosity of the host rock in the two plates to vary as a simple function (for in-  
 963 stance, linear) of the horizontal distance ( $x$ ) parallel to the interface, so that to repre-

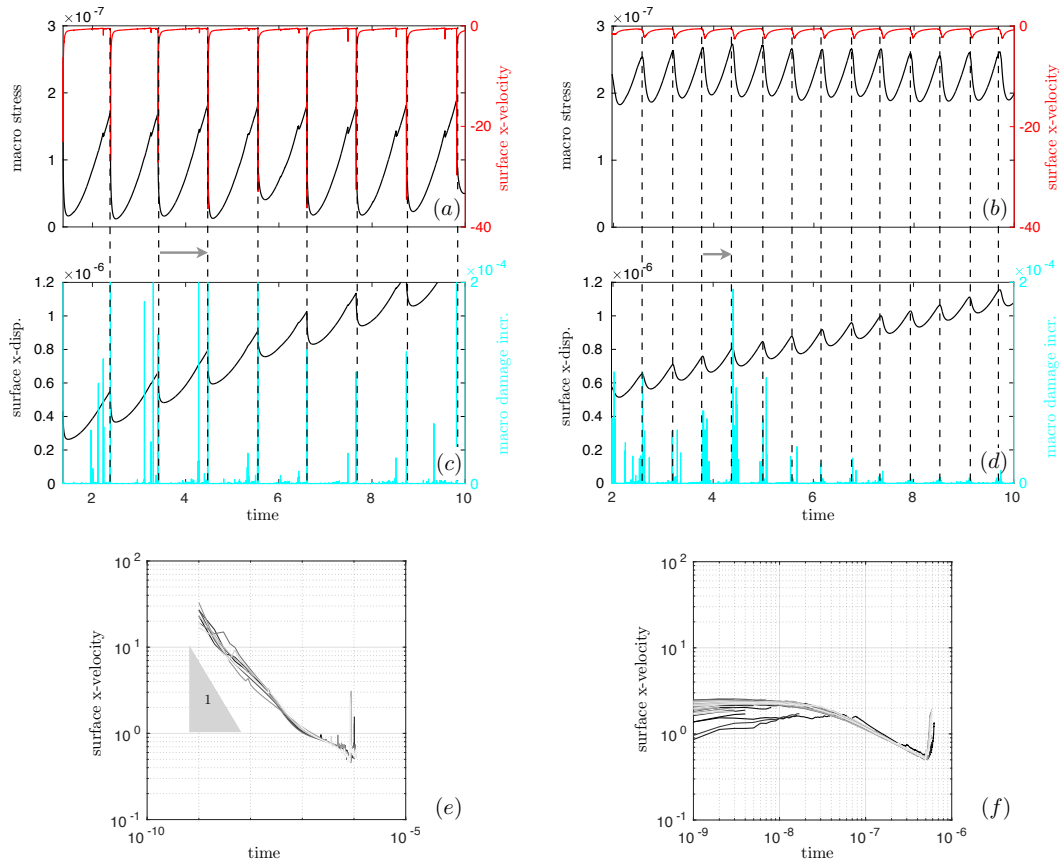


**Figure 11.** (a, b) Temporal evolution of the macroscopic stress (black curve) and of the surface  $x$ -velocity at the upper left corner of the domain (red curve) for a simulation in which  $De_0 = 0.1$  ( $\tilde{\Delta}t = 10^{-9}$ ,  $T_h = 10^{-4}$ ),  $\alpha = 4$  and (a)  $\delta d = 0.1$  and (b)  $\delta d = 0.5$ . (c, d) Corresponding temporal evolution of the cumulated surface  $x$ -displacement at the upper left corner of the domain (black curve) and of macroscopic damage increment (cyan curve). (e, f) Corresponding surface  $x$ -velocity at the upper left corner of the domain as a function of the time elapsed between each unloading event, as indicated by the dashed lines and arrows on figures (a) to (d). In figures a, b, e and f, the prescribed forcing velocity,  $U$ , is subtracted from the  $x$ -velocity.

964 sent a more brittle (high viscosity) behaviour towards the surface and a more ductile (low  
 965 viscosity) behaviour at depth. Such a dependence of the viscosity with depth would al-  
 966 low mitigating the impact of finite size effects and at the same time, exploring spatial  
 967 and temporal interactions between the different types of mechanical behaviours simul-  
 968 ated by the model, that is, an essentially brittle behaviour akin to low-depth, classical  
 969 earthquakes, a mixed brittle-ductile behaviour akin to slow-slip events and diffuse, duc-  
 970 tile deformations akin to the deeper parts of subduction zones. In the same line of ideas,  
 971 the use of the full Burger model, that is, incorporating the Kelvin component that was  
 972 left aside in the present experiments but which is meant to accounts for the deforma-  
 973 tion of the mantle (e.g., Nur & Mavko, 1974; Pollitz et al., 2001), would act as an ad-  
 974 ditional source of post-seismic transient deformation and as such would bring some ex-  
 975 tra complexity in the temporal behaviour of the model.

976 The third addition would account for friction, which most likely plays a first-order  
 977 role in the brittle part of the shear zone (e.g., Byerlee, 1967; Scholz, 1998, and many oth-  
 978 ers), where asperities can become locked, thereby allowing for stresses to locally build-

979 up and local quakes to be triggered. To simulate the effect of static friction in a simple  
 980 manner, an additional threshold on the the minimum stress required for the occurrence  
 981 of viscous deformation (as opposed to damage) could be coupled to the viscous stress  
 982 dissipation term of equation 1. This criterion, of the cohesion-less Mohr-Coulomb type,  
 983 would ensure that for low states of stress, slip would be hindered and elastic stresses would  
 984 build-up locally towards critically.

## 985 7 Conclusions

986 In this paper, we have presented a continuum, volumetric mechanical model suited  
 987 for modelling slow earthquakes. We have also presented a numerical framework for this  
 988 model that is efficient enough to cover several deformation cycles in very reasonable sim-  
 989 ulation times in a 2-dimensional setup, while allowing to resolve both the very short-term  
 990 and localized damage initiation and propagation processes associated with the co-seismic  
 991 rupture and the diffuse deformations within the bulk of the host rock that relaxes stresses  
 992 over very long time scales. In between these very short and very long time scales and  
 993 over a certain range of parameters, the model can simulate a correlated seismic (i.e., dam-  
 994 age) activity as well as different transient, seismic and aseismic processes akin to clas-  
 995 sical and slow earthquakes, such as the post-seismic stress relaxation phase.

996 In particular, the fact that the model can reproduce the observed Omori-like de-  
 997 cay in surface post-seismic velocities over a certain range of mechanical parameter val-  
 998 ues, even in the presently highly idealized simulation setup, is an important result, as  
 999 it supports the hypothesis of (Ingleby & Wright, 2017) that visco-elastic models, either  
 1000 of the Maxwell or the Burgers type, require a continuously varying viscosity or, equiv-  
 1001 alently, a continuously varying relaxation time, to reproduce this observed trend. Here,  
 1002 this continuous variation in the relaxation time is achieved by applying a unique rheo-  
 1003 logical law over the entire system, hence avoiding the need to prescribe the mechanical  
 1004 behaviour in different parts of the system or the location of the shearing zone, but let-  
 1005 ting both the elastic modulus and viscosity evolve in time and in space as simple func-  
 1006 tions of the level of damage.

1007 Leaving aside for the moment the inclusion of the dynamics of fluids, we have sug-  
 1008 gested several simple additions to the current rheological framework that aim at extend-  
 1009 ing its application to the representation of the entire seismic "cycle": that is a deforma-  
 1010 tion that comprises both classical and slow earthquakes. The one-by-one inclusion of these  
 1011 additions - a logarithmic, time-since-damage-dependant healing law, a variation of the  
 1012 viscosity with depth and a deformation threshold for static friction -, the evaluation of  
 1013 their respective impact on the simulated mechanical behaviour and the assessment of their  
 1014 relative contribution towards a more realistic reproduction of the deformation cycle of  
 1015 faults is the aim of our next paper.

## 1016 Appendix A Adimensional system of equations

1017 The model is made adimensional with respect to

- 1018 1. the horizontal extent,  $L$ , of the domain in the direction of the forcing,
- 1019 2. the prescribed forcing velocity,  $U$ ,
- 1020 3. the undamaged elastic modulus,  $E_0$ .

1021 The time characterizing the deformation process is therefore  $T = \frac{L}{U}$ . In the following,  
 1022 the superscript '˜' is used for all dimension-less variables and operators, which are listed  
 1023 in table A1.

Variables, dimensions and operators		Non-dimensional equivalent
Spatial (2D) dimension	$\mathbf{x}$	$\tilde{\mathbf{x}} = \frac{\mathbf{x}}{L}$
Time	$t$	$\tilde{t} = \frac{t}{T}$
Velocity	$\mathbf{u}$	$\tilde{\mathbf{u}} = \frac{\mathbf{u}}{U}$
Internal stress	$\sigma$	$\tilde{\sigma} = \frac{\sigma}{E_0}$
Level of damage	$d, d'$	$d, d'$
Del Operator	$\nabla$	$\tilde{\nabla} = L\nabla$

**Table A1.** Dimensional model variables and operators and their adimensional counterpart.

1024 In terms of these adimensional variables and operators, the momentum equation  
1025 reads:

$$1026 \tilde{\nabla} \cdot \tilde{\sigma} = 0 \quad (\text{A1})$$

1027 for either the pre- or post-damage stress,  $\sigma$  or  $\sigma'$ .

1028 The full constitutive equation becomes

$$1029 \frac{U}{L} E_0 \frac{\partial \tilde{\sigma}}{\partial \tilde{t}} + \frac{E_0}{\lambda_0(1-d^{\alpha-1})} \tilde{\sigma} = \frac{U}{L} E_0 (1-d) \mathbf{K} : \tilde{\varepsilon},$$

1030 or

$$1031 \frac{\partial \tilde{\sigma}}{\partial \tilde{t}} + \frac{1}{\text{De}_0(1-d)^{\alpha-1}} \tilde{\sigma} = (1-d) \mathbf{K} : \tilde{\varepsilon}, \quad (\text{A2})$$

1032 where  $\text{De}_0 = \frac{\eta_0 U}{E_0 L}$  is the (undamaged) Deborah number. The constitutive equation for  
1033 the post-damage stress redistribution is:

$$1034 \tilde{\sigma}' - \delta d \tilde{\sigma} = (1-d') \mathbf{K} : \tilde{\varepsilon}. \quad (\text{A3})$$

1035 Damage being a non-dimensional variable, the damage equation (5) is itself adimensional:

$$1036 1 - d' = \delta d (1 - d). \quad (\text{A4})$$

1037 The adimensional healing equation reads

$$1038 \frac{1}{T} \frac{\partial d'}{\partial \tilde{t}} = -\frac{1}{t_h} d', \quad 0 \leq d' < 1,$$

1039 or

$$1040 \frac{\partial d'}{\partial \tilde{t}} = -\frac{1}{T_h} d', \quad 0 \leq d' < 1. \quad (\text{A5})$$

1041 where  $T_h = \frac{t_h}{T}$ .

## 1042 Appendix B Numerical Scheme

1043 Here we present the time discretization and the numerical algorithm employed to  
1044 solve the system of equations in the shearing experiments. For simplicity, the superscript  
1045 '~~' for adimensional variables is drop in the following notations.

1046 This system of equations (A1 for  $\sigma$  and for  $\sigma'$ , A2, A3, A4, A5) forms a problem  
1047 that is solved for the following unknowns :  $\dot{\varepsilon}$  and  $\varepsilon'$  (3 components each),  $\sigma$  and  $\sigma'$  (3  
1048 components each) and  $d'$ , starting from an initial state of rest and zero damage. It is solved

1049 over a closed 2-dimensional domain  $\Omega \in \mathbb{R}$  (see figure 4), with an external boundary  
 1050 partitioned as  $\partial\Omega = \Gamma_{\text{top}}, \Gamma_{\text{bottom}}, \Gamma_{\text{left}}, \Gamma_{\text{right}}$ . A constant  $x$ -velocity is applied on  $\Gamma_{\text{bottom}}$ .  
 1051 It is fixed to 0 during the steady-state, stress redistribution process. The  $z$ -velocity is  
 1052 fixed to 0 on  $\Gamma_{\text{bottom}}$  and  $u_x = 0$  on the right upper corner of the domain. The top and  
 1053 lateral boundaries are free, hence  $\sigma \cdot \mathbf{n} = 0$  on  $\Gamma_{\text{top}}, \Gamma_{\text{left}}$  and  $\Gamma_{\text{right}}$ .

### 1054 ***B01 Time discretization***

1055 We discretize the time,  $t$ , such that  $t_n = n\Delta t$ , with  $\Delta t > 0$  and  $n = 0, 1, 2, \dots$   
 1056 and use a backward Euler (implicit) scheme of order 1. Expressing the strain rate tensor  
 1057 as  $\dot{\epsilon} = D(\mathbf{u}) = \frac{1}{2}(\nabla\mathbf{u} + \nabla\mathbf{u}^T)$  and the strain tensor as  $D(\mathbf{u})\Delta t$ , the time-discretized  
 1058 system of equations reads:

$$\begin{aligned}
 1059 \quad & \nabla \cdot \sigma^{n+1} = 0, \\
 1060 \quad & \frac{\sigma^{n+1} - \sigma^n}{\Delta t} + \frac{1}{\text{De}_0 (1 - d^n)^{\alpha-1}} \sigma^{n+1} = (1 - d^n) \mathbf{K} : D(\mathbf{u}^{n+1}), \\
 1061 \quad & 1 - d'^n = \delta d (1 - d^n) \\
 1062 \quad & \nabla \cdot \sigma'^{n+1} = 0, \\
 1063 \quad & \sigma'^{n+1} - \delta d \sigma^{n+1} = (1 - d'^n) \mathbf{K} : D(\mathbf{u}'^{n+1} \Delta t), \\
 1064 \quad & \frac{d'^{n+1} - d'^n}{\Delta t} = -\frac{1}{T_h} d'^n, \quad 0 < d'^{n+1} \leq 1.
 \end{aligned}$$

1065 The numerical scheme divides this time-discretized problem,  $P_d$ , into three subprob-  
 1066 lems. Using the superscript  $k = 0, 1, 2, \dots$  for the steady-state stress-redistribution sub-  
 1067 iteration in subproblem 2, these problems reads:

- 1068 ( $P1_d$ ) The momentum and constitutive equations are first solved simultaneously for the  
 1069 fields of velocity and stress,  $\sigma^{n+1}$  and  $\mathbf{u}^{n+1}$  at the current time step, by apply-  
 1070 ing the constant  $x$ -velocity forcing on  $\Gamma_{\text{bottom}}$  and the other boundary conditions  
 1071 and using the level of damage at the previous time step,  $d^n$ .
- 1072 ( $P2_d$ ) The steady-state stress redistribution equations are solved iteratively, with the  $x$ -velocity  
 1073 on  $\Gamma_{\text{bottom}}$  now set to zero. In this subproblem, the damage equation is first solved  
 1074 for  $d'^{n,k+1}$  by comparing the field of stress at the current subiteration,  $\sigma^{n+1,k}$ , to  
 1075 the local damage criteria,  $\sigma_c$ . The updated level of damage is then substituted into  
 1076 the post-damage constitutive equation. Together with the momentum equation,  
 1077 it is solved for the adjusted fields of velocity,  $\mathbf{u}'^{n+1,k+1}$ , and stress,  $\sigma'^{n+1,k+1}$ . These  
 1078 steps are iterated until all of the adjusted stresses become sub-critical. Then the  
 1079 post-damage level of damage,  $d'^n$ , is set to  $d'^{n,k+1}$ .
- 1080 ( $P3_d$ ) The healing equation is finally solved for the level of damage at the current time  
 1081 step,  $d'^{n+1}$  and  $d^{n+1}$  is set to  $d'^{n+1}$ .

1082 The complete algorithm reads:

1083 *Initialization* ( $n = 0$ )

$$\begin{aligned}
 1084 \quad & \mathbf{u}^n = 0 \text{ in } \Omega, \\
 1085 \quad & \sigma^n = 0 \text{ in } \Omega, \\
 1086 \quad & d^n = d'^n = 0 \text{ in } \Omega.
 \end{aligned}$$

1087 For  $n \geq 0$ , set  $k = 0$

1088 (P1<sub>d</sub>) With  $\sigma^n$  and  $d^n$  known, find  $\sigma^{n+1}$  and  $\mathbf{u}^{n+1}$  such that

$$1089 \quad \nabla \cdot \sigma^{n+1} = 0,$$

$$1090 \quad \frac{\sigma^{n+1} - \sigma^n}{\Delta t} + \frac{1}{\text{De}_0(1-d^n)^{\alpha-1}} \sigma^{n+1} = (1-d^n) \mathbf{K} : D(\mathbf{u}^{n+1}),$$

1091

1092 and with

$$1093 \quad u_z^{n+1} = 0 \text{ on } \Gamma_{\text{bottom}},$$

$$1094 \quad u_x^{n+1} = 1 \text{ on } \Gamma_{\text{bottom}},$$

$$1095 \quad u_x^{n+1} = 0 \text{ on } \Gamma_{\text{top}} \cap \Gamma_{\text{right}},$$

$$1096 \quad \sigma^{n+1} \cdot \mathbf{n} = 0 \text{ on } \Gamma_{\text{top}}, \Gamma_{\text{left}} \text{ and } \Gamma_{\text{right}}, .$$

1097 IF anywhere in  $\Omega$   $\sigma_1^{n+1} > q\sigma_2^{n+1} + \sigma_c$ , set  $\sigma'^{n+1,k} = \sigma^{n+1}$  and  $d'^{n,k} = d^n$ .

1098 (P2<sub>d</sub>) For  $k \geq 0$ ,

1099 1. Find  $d'^{n,k+1}$  such that

$$1100 \quad 1 - d'^{n,k+1} = \delta d (1 - d'^{n,k}),$$

1101 2. Find  $\sigma^{n+1,k+1}$  and  $\mathbf{u}^{n+1,k+1}$  such that

$$1102 \quad \nabla \cdot \sigma^{n+1,k+1} = 0,$$

$$1103 \quad \sigma'^{n+1,k+1} - \delta d \sigma'^{n+1,k} = E_0(1 - d'^{n,k+1}) \mathbf{K} : (D(\mathbf{u}'^{n+1,k+1}) \Delta t)$$

1104 and with

$$1105 \quad u_z'^{n+1,k+1} = 0 \text{ on } \Gamma_{\text{bottom}},$$

$$1106 \quad u_x'^{n+1,k+1} = 0 \text{ on } \Gamma_{\text{bottom}},$$

$$1107 \quad u_x'^{n+1,k+1} = 0 \text{ on } \Gamma_{\text{top}} \cap \Gamma_{\text{right}},$$

$$1108 \quad \sigma'^{n+1,k+1} \cdot \mathbf{n} = 0 \text{ on } \Gamma_{\text{top}}, \Gamma_{\text{left}} \text{ and } \Gamma_{\text{right}}, .$$

1109 IF  $\sigma_1'^{n+1,k+1} \leq q\sigma_2'^{n+1,k+1} + \sigma_c$ ,  
 1110 STOP and set  $\sigma^{n+1} = \sigma'^{n+1,k+1}$  and  $d'^n = d'^{n,k+1}$  (P3<sub>d</sub>) Find  $d'^{n+1}$  such that

$$1111 \quad \frac{d'^{n+1} - d'^n}{\Delta t} = -\frac{1}{T_h} d'^n, \quad 0 < d'^{n+1} \leq 1.$$

1112 Set  $d^{n+1} = d'^{n+1}$ .

## 1113 Appendix C Convergence

1114 Figure C1 shows the probability density function of  $E_{\text{brit}}/\tilde{\Delta}t$  obtained in the case  
 1115 of  $\text{De}_0 = 0.1$  and  $\text{De}_0 = 10$ , using  $\alpha = 4$ ,  $\delta d = 0.1$  and  $T_h = 10^{-4}$  and  $T_h = 10^{-3}$  re-  
 1116 spectively. The PDFs indicate that the macroscopic model response converges as  $\tilde{\Delta}t$  is  
 1117 decreased, as for the case of  $\text{De}_0 = 0.001$  described in section 5.2. The values of  $\tilde{\Delta}t$  for  
 1118 which the response is not converged are indicated in red in table 3. The value of  $\tilde{\Delta}t$  cor-  
 1119 responding to each  $\text{De}_0$  value and used in the sensitivity analyses on  $T_h$ ,  $\alpha$  and  $\delta d$  are  
 1120 indicated in green in the same table.

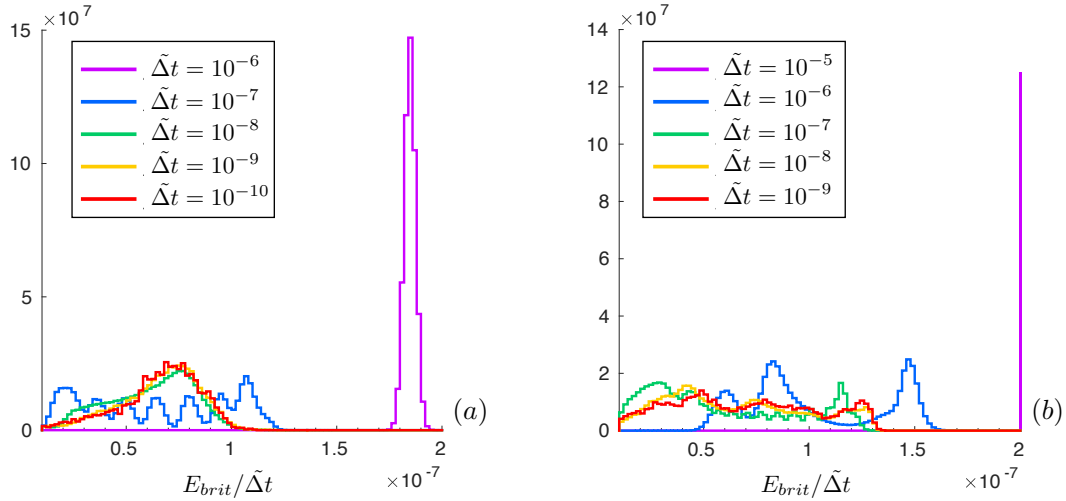


**Figure C1.** Probability density function of  $E_{brit}/\tilde{\Delta t}$  for simulations using  $\alpha = 4$ ,  $\delta d = 0.1$  and (a)  $De_0 = 0.1$ ,  $T_h = 10^{-4}$  and  $\tilde{\Delta t} = 10^{-10}, 10^{-9}, 10^{-8}, 10^{-7}, 10^{-6}$  and (b)  $De_0 = 10$ ,  $T_h = 10^{-3}$  and  $\tilde{\Delta t} = 10^{-9}, 10^{-8}, 10^{-7}, 10^{-6}, 10^{-5}$  (corresponding to  $\Delta t = 10^4$  s,  $10^5$  s,  $10^6$  s,  $10^7$  s,  $10^8$  s respectively).

## 1121 Acknowledgments

1122 The authors thank David Amitrano and Jean-Luc Got for insightful discussions about  
 1123 this paper and related topics. V. D., N. S. and M. C. acknowledge support from the Eu-  
 1124 ropean Research Council (ERC) under the European Union’s Horizon 2020 research and  
 1125 innovation program (Grant agreements no 787399, SEISMAZE for N. S. and V. D. and  
 1126 742335, F-IMAGE for M. C.).

1127 The outputs of numerical simulations can be found at: XXXZenodo. The post-processing  
 1128 MATLAB codes used to produce the figures and movie presented in this paper and SI  
 1129 are available at: <https://github.com/vdansereau/Multi-Scale-Deformation-Cycle-AGU-Solid-Earth-paper.git>. The model equations and the numerical scheme (time  
 1130 and space discretizations) are fully described in sections 2.4 and 3 of the main text and  
 1131 in the Appendix A and Appendix B, to allow reproducibility. The C++ library RHE-  
 1132 OLEF used to set the domain and boundary conditions and to solve the set of equations  
 1133 is documented and available for download at <https://membres-ljk.imag.fr/Pierre.Saramito/rheolef/html/index.html>.  
 1134  
 1135

## 1136 References

- 1137 Amitrano, D. (2003). Brittle-ductile transition and associated seismicity: Exper-  
 1138 imental and numerical studies and relationship with the  $b$  value. *Journal of*  
 1139 *Geophysical Research*, *108*(B1). doi: 10.1029/2001JB000680  
 1140 Amitrano, D., Grasso, J.-R., & Hantz, D. (1999). From diffuse to localised damage  
 1141 through elastic interaction. *Geophysical Research Letters*, *26*(14), 2109-2112.  
 1142 Angiboust, S., Kirsch, J., Oncken, O., G., J., Monié, P., & Rybacki, E. (2015).  
 1143 Probing the transition between seismically coupled and decoupled segments  
 1144 along an ancient subduction interface. *Geochemistry, Geophysics, Geosys-*  
 1145 *tems*, *16*(6), 1905-1922. Retrieved from [https://agupubs.onlinelibrary](https://agupubs.onlinelibrary.wiley.com/doi/abs/10.1002/2015GC005776)  
 1146 [.wiley.com/doi/abs/10.1002/2015GC005776](https://agupubs.onlinelibrary.wiley.com/doi/abs/10.1002/2015GC005776) doi: [https://doi.org/10.1002/](https://doi.org/10.1002/2015GC005776)  
 1147 [2015GC005776](https://doi.org/10.1002/2015GC005776)  
 1148 Ashby, M. F., & Sammis, C. G. (1990). The damage mechanics of brittle solids in

- 1149 compression. *pure and applied geophysics*, 133(3), 489–521. Retrieved from  
 1150 <https://doi.org/10.1007/BF00878002> doi: 10.1007/BF00878002
- 1151 Audet, P., Bostock, M., Christensen, N., & Peacock, S. M. (2009). Seismic evidence  
 1152 for overpressured subducted oceanic crust and megathrust fault sealing. *Nature*,  
 1153 457(7225), 76–78. doi: 10.1038/nature07650
- 1154 Ben-Zion, Y., & Lyakhovsky, V. (2002). Accelerated seismic release and related  
 1155 aspects of seismicity patterns on earthquake faults. In M. Matsu'ura,  
 1156 P. Mora, A. Donnellan, & X.-c. Yin (Eds.), *Earthquake processes: Physical modelling, numerical simulation and data analysis part ii* (pp. 2385–  
 1157 2412). Basel: Birkhäuser Basel. Retrieved from [https://doi.org/10.1007/](https://doi.org/10.1007/978-3-0348-8197-5_12)  
 1158 [978-3-0348-8197-5\\_12](https://doi.org/10.1007/978-3-0348-8197-5_12) doi: 10.1007/978-3-0348-8197-5\_12
- 1160 Ben-Zion, Y., & Lyakhovsky, V. (2006, 04). Analysis of aftershocks in a lithospheric  
 1161 model with seismogenic zone governed by damage rheology. *Geophysical Journal International*,  
 1162 165(1), 197–210. Retrieved from [https://doi.org/10](https://doi.org/10.1111/j.1365-246X.2006.02878.x)  
 1163 [.1111/j.1365-246X.2006.02878.x](https://doi.org/10.1111/j.1365-246X.2006.02878.x) doi: 10.1111/j.1365-246X.2006.02878.x
- 1164 Bhat, H. S., Rosakis, A. J., & Sammis, C. G. (2012, 04). A Micromechanics Based  
 1165 Constitutive Model for Brittle Failure at High Strain Rates. *Journal of Applied Mechanics*,  
 1166 79(3). Retrieved from <https://doi.org/10.1115/1.4005897>  
 1167 (031016) doi: 10.1115/1.4005897
- 1168 Bos, B., & Spiers, C. J. (2002). Fluid-assisted healing processes in gouge-bearing  
 1169 faults: Insights from experiments on a rock analogue system. *pure and applied*  
 1170 *geophysics*, 159(11), 2537–2566. Retrieved from [https://doi.org/10.1007/](https://doi.org/10.1007/s00024-002-8747-2)  
 1171 [s00024-002-8747-2](https://doi.org/10.1007/s00024-002-8747-2) doi: 10.1007/s00024-002-8747-2
- 1172 Bostock, M. G., Royer, A. A., Hearn, E. H., & Peacock, S. M. (2012). Low  
 1173 frequency earthquakes below southern vancouver island. *Geochemistry, Geophysics, Geosystems*,  
 1174 13(11), Q11007. doi: [https://doi.org/10.1029/](https://doi.org/10.1029/2012GC004391)  
 1175 [2012GC004391](https://doi.org/10.1029/2012GC004391)
- 1176 Brenguier, F., Campillo, M., Hadziioannou, C., Shapiro, N. M., Nadeau, R. M.,  
 1177 & Larose, E. (2008). Postseismic relaxation along the san andreas fault at  
 1178 parkfield from continuous seismological observations. *Science*, 321(5895),  
 1179 1478–1481. Retrieved from [https://science.sciencemag.org/content/321/](https://science.sciencemag.org/content/321/5895/1478)  
 1180 [5895/1478](https://science.sciencemag.org/content/321/5895/1478) doi: 10.1126/science.1160943
- 1181 Brown, K. M., Tryon, M. D., DeShon, H. R., Dorman, L. M., & Schwartz, S. Y.  
 1182 (2005). Correlated transient fluid pulsing and seismic tremor in the costa rica  
 1183 subduction zone. *Earth and Planetary Science Letters*, 238(1), 189–203. doi:  
 1184 <https://doi.org/10.1016/j.epsl.2005.06.055>
- 1185 Brudzinski, M. R., & Allen, R. M. (2007, 10). Segmentation in episodic tremor and  
 1186 slip all along Cascadia. *Geology*, 35(10), 907–910. doi: 10.1130/G23740A.1
- 1187 Burov, E. B. (2011). Rheology and strength of the lithosphere. *Marine and Petroleum Geology*,  
 1188 28(8), 1402 - 1443. Retrieved from [http://](http://www.sciencedirect.com/science/article/pii/S0264817211001425)  
 1189 [www.sciencedirect.com/science/article/pii/S0264817211001425](http://www.sciencedirect.com/science/article/pii/S0264817211001425) doi:  
 1190 <https://doi.org/10.1016/j.marpetgeo.2011.05.008>
- 1191 Burridge, R., & Knopoff, L. (1967). Model and theoretical seismicity. *Bulletin of the*  
 1192 *Seismological Society of America*, 57(3), 341–371.
- 1193 Byerlee, J. D. (1967). Frictional characteristics of granite under high con-  
 1194 fining pressure. *Journal of Geophysical Research*, 72(14), 3639–3648.  
 1195 Retrieved from <http://dx.doi.org/10.1029/JZ072i014p03639> doi:  
 1196 [10.1029/JZ072i014p03639](https://doi.org/10.1029/JZ072i014p03639)
- 1197 Byerlee, J. D. (1978). Friction of rocks. *Pure and Applied Geophysics*, 116, 615–626.  
 1198 doi: <https://doi.org/10.1007/BF00876528>
- 1199 Caine, J. S., Evans, J. P., & Forster, C. B. (1996, 11). Fault zone architecture  
 1200 and permeability structure. *Geology*, 24(11), 1025–1028. Retrieved from  
 1201 [https://doi.org/10.1130/0091-7613\(1996\)024<1025:FZAAPS>2.3.CO;2](https://doi.org/10.1130/0091-7613(1996)024<1025:FZAAPS>2.3.CO;2)  
 1202 doi: 10.1130/0091-7613(1996)024(1025:FZAAPS)2.3.CO;2
- 1203 Carlson, J. M., & Langer, J. S. (1989). Properties of earthquakes generated by fault

- 1204 dynamics. *Phys. Rev. Lett.*, *62*, 2632–2635. Retrieved from <https://link>  
 1205 [.aps.org/doi/10.1103/PhysRevLett.62.2632](https://link.aps.org/doi/10.1103/PhysRevLett.62.2632) doi: 10.1103/PhysRevLett.62  
 1206 [.2632](https://link.aps.org/doi/10.1103/PhysRevLett.62.2632)
- 1207 Carrier, A., Got, J.-L., Peltier, A., Ferrazzini, V., Staudacher, T., Kowalski, P.,  
 1208 & Boissier, P. (2015, January). A damage model for volcanic edifices:  
 1209 Implications for edifice strength, magma pressure, and eruptive processes.  
 1210 *Journal of Geophysical Research (Solid Earth)*, *120*(1), 567–583. doi:  
 1211 [10.1002/2014JB011485](https://doi.org/10.1002/2014JB011485)
- 1212 Chen, J., Niemeijer, A. R., & Spiers, C. J. (2017). Microphysically derived expres-  
 1213 sions for rate-and-state friction parameters,  $a$ ,  $b$ , and  $dc$ . *Journal of Geophys-*  
 1214 *ical Research: Solid Earth*, *122*(12), 9627–9657. Retrieved from [https://](https://agupubs.onlinelibrary.wiley.com/doi/abs/10.1002/2017JB014226)  
 1215 [agupubs.onlinelibrary.wiley.com/doi/abs/10.1002/2017JB014226](https://agupubs.onlinelibrary.wiley.com/doi/abs/10.1002/2017JB014226) doi:  
 1216 <https://doi.org/10.1002/2017JB014226>
- 1217 Cotte, N., Walpersdorf, A., Kostoglodov, V., Vergnolle, M., Santiago, J.-A., &  
 1218 Campillo, M. (2009). Anticipating the next large silent earthquake in mex-  
 1219 ico. *Eos, Transactions American Geophysical Union*, *90*(21), 181–182. doi:  
 1220 <https://doi.org/10.1029/2009EO210002>
- 1221 Cruz-Atienza, V. M., Villafuerte, C., & Bhat, H. S. (2018). Rapid tremor migration  
 1222 and pore-pressure waves in subduction zones. *Nature Communications*, *9*(1),  
 1223 2900. doi: [10.1038/s41467-018-05150-3](https://doi.org/10.1038/s41467-018-05150-3)
- 1224 Dansereau, V. (2016b). *A Maxwell-Elasto-Brittle model for the drift and deforma-*  
 1225 *tion of sea ice* (Theses, Université Grenoble Alpes). Retrieved from [https://](https://tel.archives-ouvertes.fr/tel-01316987)  
 1226 [tel.archives-ouvertes.fr/tel-01316987](https://tel.archives-ouvertes.fr/tel-01316987)
- 1227 Dansereau, V., Weiss, J., Saramito, P., & Lattes, P. (2016a). A Maxwell-elasto-  
 1228 brittle rheology for sea ice modelling. *The Cryosphere*, *10*, 1339–1359.
- 1229 Dieterich, J. H. (1978). Time-dependent friction and the mechanics of stick-  
 1230 slip. *pure and applied geophysics*, *116*(4), 790–806. Retrieved from  
 1231 <https://doi.org/10.1007/BF00876539> doi: [10.1007/BF00876539](https://doi.org/10.1007/BF00876539)
- 1232 Dieterich, J. H. (1979a). Modeling of rock friction: 1. experimental results and  
 1233 constitutive equations. *Journal of Geophysical Research: Solid Earth*, *84*(B5),  
 1234 2161–2168. Retrieved from [https://agupubs.onlinelibrary.wiley.com/](https://agupubs.onlinelibrary.wiley.com/doi/abs/10.1029/JB084iB05p02161)  
 1235 [doi/abs/10.1029/JB084iB05p02161](https://doi.org/10.1029/JB084iB05p02161) doi: [https://doi.org/10.1029/](https://doi.org/10.1029/JB084iB05p02161)  
 1236 [JB084iB05p02161](https://doi.org/10.1029/JB084iB05p02161)
- 1237 Dieterich, J. H. (1979b). Modeling of rock friction: 2. simulation of preseismic  
 1238 slip. *Journal of Geophysical Research: Solid Earth*, *84*(B5), 2169–2175.  
 1239 Retrieved from [https://agupubs.onlinelibrary.wiley.com/doi/abs/](https://agupubs.onlinelibrary.wiley.com/doi/abs/10.1029/JB084iB05p02169)  
 1240 [10.1029/JB084iB05p02169](https://doi.org/10.1029/JB084iB05p02169) doi: <https://doi.org/10.1029/JB084iB05p02169>
- 1241 Dragert, H., Wang, K., & James, T. (2001). A silent slip event on the deeper casca-  
 1242 dia subduction interface. *Science*, *292*, 1525–1528.
- 1243 Dragert, H., Wang, K., & Rogers, G. (2004). Geodetic and seismic signatures of  
 1244 episodic tremor and slip in the northern Cascadia subduction zone. *Earth,*  
 1245 *Planets and Space*, *56*, 1143–1150.
- 1246 Dublanchet, P. (2019). Fluid driven shear cracks on a strengthening rate-and-state  
 1247 frictional fault. *Journal of the Mechanics and Physics of Solids*, *132*, 103672.  
 1248 doi: <https://doi.org/10.1016/j.jmps.2019.07.015>
- 1249 Dziewonski, A. M., & Anderson, D. L. (1981). Preliminary reference earth model.  
 1250 *Physics of the Earth and Planetary Interiors*, *25*(4), 297 - 356. Retrieved from  
 1251 <http://www.sciencedirect.com/science/article/pii/0031920181900467>  
 1252 doi: [https://doi.org/10.1016/0031-9201\(81\)90046-7](https://doi.org/10.1016/0031-9201(81)90046-7)
- 1253 Farge, G., Jaupart, C., & Shapiro, N. M. (2021). Episodicity and migration of low  
 1254 frequency earthquakes modeled with fast fluid pressure transients in the per-  
 1255 meable subduction interface. *Journal of Geophysical Research: Solid Earth*,  
 1256 *126*(9), e2021JB021894. doi: <https://doi.org/10.1029/2021JB021894>
- 1257 Frank, W. B., Radiguet, M., Rousset, B., Shapiro, N. M., Husker, A. L., Kos-  
 1258 toglodov, V., ... Campillo, M. (2015). Uncovering the geodetic signature

- 1259 of silent slip through repeating earthquakes. *Geophysical Research Letters*, *42*,  
1260 2774–2779. doi: 10.1002/2015GL063685
- 1261 Frank, W. B., Shapiro, N. M., Husker, A., Kostoglodov, V., Bhat, H. S., &  
1262 Campillo, M. (2015). Along-fault pore-pressure evolution during a slow-slip  
1263 event in guerrero, mexico. *Earth and Planetary Science Letters*, *413*, 135–143.  
1264 doi: <https://doi.org/10.1016/j.epsl.2014.12.051>
- 1265 Frank, W. B., Shapiro, N. M., Husker, A. L., Kostoglodov, V., Gusev, A. A., &  
1266 Campillo, M. (2016). The evolving interaction of low-frequency earth-  
1267 quakes during transient slip. *Science Advances*, *2*(4). Retrieved from  
1268 <https://advances.sciencemag.org/content/2/4/e1501616> doi:  
1269 10.1126/sciadv.1501616
- 1270 Frank, W. B., Shapiro, N. M., Husker, A. L., Kostoglodov, V., Romanenko, A.,  
1271 & Campillo, M. (2014). Using systematically characterized low-frequency  
1272 earthquakes as a fault probe in guerrero, mexico. *Journal of Geophysi-  
1273 cal Research: Solid Earth*, *119*(10), 7686–7700. Retrieved from [https://  
1274 agupubs.onlinelibrary.wiley.com/doi/abs/10.1002/2014JB011457](https://agupubs.onlinelibrary.wiley.com/doi/abs/10.1002/2014JB011457) doi:  
1275 <https://doi.org/10.1002/2014JB011457>
- 1276 Frederiksen, S., & Braun, J. (2001). Numerical modelling of strain localisation dur-  
1277 ing extension of the continental lithosphere. *Earth and Planetary Science Let-  
1278 ters*, *188*, 241–251.
- 1279 Gao, X., & Wang, K. (2017). Rheological separation of the megathrust seismogenic  
1280 zone and episodic tremor and slip. *Nature*, *543*, 416–419. doi: [https://doi.org/  
1281 10.1038/nature21389](https://doi.org/10.1038/nature21389)
- 1282 Gardner, J. K., & Knopoff, L. (1974, 10). Is the sequence of earthquakes in Southern  
1283 California, with aftershocks removed, Poissonian? *Bulletin of the Seismologi-  
1284 cal Society of America*, *64*(5), 1363–1367. Retrieved from [https://doi.org/10  
1285 .1785/BSSA0640051363](https://doi.org/10.1785/BSSA0640051363) doi: 10.1785/BSSA0640051363
- 1286 Geuzaine, C., & Remacle, J.-F. (2009). Gmsh: A 3-d finite element mesh gener-  
1287 ator with built-in pre- and post-processing facilities. *International Journal  
1288 for Numerical Methods in Engineering*, *79*(11), 1309–1331. Retrieved from  
1289 <https://onlinelibrary.wiley.com/doi/abs/10.1002/nme.2579> doi:  
1290 <https://doi.org/10.1002/nme.2579>
- 1291 Got, J.-L., Carrier, A., Marsan, D., Jouanne, F., Vogfjörd, K., & Villetent, T.  
1292 (2017). An analysis of the non-linear magma-edifice coupling at grimsvötn  
1293 volcano (iceland). *Journal of Geophysical Research Solid Earth*, *122*. doi:  
1294 10.1002/2016JB012905
- 1295 Griffin, J. D., Stirling, M. W., & Wang, T. (2020). Periodicity and clustering  
1296 in the long-term earthquake record. *Geophysical Research Letters*, *47*(22),  
1297 e2020GL089272. Retrieved from [https://agupubs.onlinelibrary.wiley  
1298 .com/doi/abs/10.1029/2020GL089272](https://agupubs.onlinelibrary.wiley.com/doi/abs/10.1029/2020GL089272) (e2020GL089272 2020GL089272) doi:  
1299 <https://doi.org/10.1029/2020GL089272>
- 1300 Gutenberg, B., & Richter, C. F. (1949). *Seismicity of the earth and associated phe-  
1301 nomena*. Princeton NJ USA: Princeton University Press.
- 1302 Hamiel, Y., Liu, Y., Lyakhovskiy, V., Ben-Zion, Y., & Lockner, D. (2004). A  
1303 viscoelastic damage model with applications to stable and unstable frac-  
1304 turing. *Geophysical Journal International*, *159*, 1155–1165. doi: 10.1111/  
1305 j.1365-246X.2004.02452.x
- 1306 Handwerker, A. L., Rempel, A. W., Skarbek, R. M., Roering, J. J., & Hilley, G. E.  
1307 (2016). Rate-weakening friction characterizes both slow sliding and catas-  
1308 trophic failure of landslides. *Proceedings of the National Academy of Sciences*,  
1309 *113*(37), 10281–10286. Retrieved from [https://www.pnas.org/content/113/  
1310 37/10281](https://www.pnas.org/content/113/37/10281) doi: 10.1073/pnas.1607009113
- 1311 Hayman, N. W., & Lavier, L. L. (2014). The geologic record of deep episodic tremor  
1312 and slip. *Geology*, *42*(3), 195–198. Retrieved from [https://doi.org/10.1130/  
1313 G34990.1](https://doi.org/10.1130/G34990.1) doi: 10.1130/G34990.1

- 1314 Hetland, E. A., & Hager, B. H. (2005). Postseismic and interseismic displacements near a strike-slip fault: A two-dimensional theory for general linear viscoelastic rheologies. *Journal of Geophysical Research: Solid Earth*, *110*(B10). Retrieved from <https://agupubs.onlinelibrary.wiley.com/doi/abs/10.1029/2005JB003689> doi: <https://doi.org/10.1029/2005JB003689>
- 1315  
1316  
1317  
1318
- 1319 Hetland, E. A., & Hager, B. H. (2006, 07). The effects of rheological layering on post-seismic deformation. *Geophysical Journal International*, *166*(1), 277-292. Retrieved from <https://doi.org/10.1111/j.1365-246X.2006.02974.x> doi: [10.1111/j.1365-246X.2006.02974.x](https://doi.org/10.1111/j.1365-246X.2006.02974.x)
- 1320  
1321  
1322
- 1323 Hirono, T., Kaneki, S., Ishikawa, T., Kameda, J., Tonoike, N., Ito, A., & Miyazaki, Y. (2020). Generation of sintered fault rock and its implications for earthquake energetics and fault healing. *Communications Earth & Environment*, *1*(1), 3. Retrieved from <https://doi.org/10.1038/s43247-020-0004-z> doi: [10.1038/s43247-020-0004-z](https://doi.org/10.1038/s43247-020-0004-z)
- 1324  
1325  
1326  
1327
- 1328 Hunfeld, L. B., Chen, J., Hol, S., Niemeijer, A. R., & Spiers, C. J. (2020). Healing behavior of simulated fault gouges from the groningen gas field and implications for induced fault reactivation. *Journal of Geophysical Research: Solid Earth*, *125*(7), e2019JB018790. Retrieved from <https://agupubs.onlinelibrary.wiley.com/doi/abs/10.1029/2019JB018790> (e2019JB018790 2019JB018790) doi: <https://doi.org/10.1029/2019JB018790>
- 1329  
1330  
1331  
1332  
1333
- 1334 Idehara, K., Yabe, S., & Ide, S. (2014, December). Regional and global variations in the temporal clustering of tectonic tremor activity. *Earth, Planets and Space*, *66*(1), 66. doi: [10.1186/1880-5981-66-66](https://doi.org/10.1186/1880-5981-66-66)
- 1335  
1336
- 1337 Ingleby, T., & Wright, T. J. (2017). Omori-like decay of postseismic velocities following continental earthquakes. *Geophysical Research Letters*, *44*(7), 3119-3130. Retrieved from <https://agupubs.onlinelibrary.wiley.com/doi/abs/10.1002/2017GL072865> doi: <https://doi.org/10.1002/2017GL072865>
- 1338  
1339  
1340
- 1341 Jaeger, J. C., & Cook, N. G. W. (1979). *Fundamentals of rock mechanics*. Cambridge UK: Chapman and Hall.
- 1342
- 1343 Kachanov, L. M. (1958). On rupture time under condition of creep. *Izvestia Akademi Nauk SSSR, Otd. Tekhn. Nauk*, *8*, 26-31. ((in Russian))
- 1344
- 1345 Kostoglodov, V., Singh, S. K., Santiago, J. A., Franco, S. I., Larson, K. M., Lowry, A. R., & Bilham, R. (2003). A large silent earthquake in the guerrero seismic gap, mexico. *Geophysical Research Letters*, *30*(15), 1807. doi: [10.1029/2003GL017219](https://doi.org/10.1029/2003GL017219)
- 1346  
1347  
1348
- 1349 Lacroix, P., Perfettini, H., Taïpe, E., & Guillier, B. (2014). Coseismic and post-seismic motion of a landslide: Observations, modeling, and analogy with tectonic faults. *Geophysical Research Letters*, *41*(19), 6676-6680. Retrieved from <https://agupubs.onlinelibrary.wiley.com/doi/abs/10.1002/2014GL061170> doi: <https://doi.org/10.1002/2014GL061170>
- 1350  
1351  
1352  
1353
- 1354 Li, Y.-G., & Vidale, J. E. (2001). Healing of the shallow fault zone from 1994-1998 after the 1992 m7.5 landers, california, earthquake. *Geophysical Research Letters*, *28*(15), 2999-3002. Retrieved from <https://agupubs.onlinelibrary.wiley.com/doi/abs/10.1029/2001GL012922> doi: <https://doi.org/10.1029/2001GL012922>
- 1355  
1356  
1357  
1358
- 1359 Li, Y.-G., Vidale, J. E., Aki, K., Xu, F., & Burdette, T. (1998). Evidence of shallow fault zone strengthening after the 1992 m7.5 landers, california, earthquake. *Science*, *279*(5348), 217-219. Retrieved from <https://www.science.org/doi/abs/10.1126/science.279.5348.217> doi: [10.1126/science.279.5348.217](https://doi.org/10.1126/science.279.5348.217)
- 1360  
1361  
1362  
1363
- 1364 Liu, Y., & Rice, J. R. (2005). Aseismic slip transients emerge spontaneously in three-dimensional rate and state modeling of subduction earthquake sequences. *Journal of Geophysical Research: Solid Earth*, *110*(B8). Retrieved from <https://agupubs.onlinelibrary.wiley.com/doi/abs/10.1029/2004JB003424> doi: <https://doi.org/10.1029/2004JB003424>
- 1365  
1366  
1367  
1368

- 1369 Liu, Y., & Rice, J. R. (2007). Spontaneous and triggered aseismic deformation  
1370 transients in a subduction fault model. *Journal of Geophysical Research:*  
1371 *Solid Earth*, *112*(B9). Retrieved from <https://agupubs.onlinelibrary>  
1372 [.wiley.com/doi/abs/10.1029/2007JB004930](https://agupubs.onlinelibrary.wiley.com/doi/abs/10.1029/2007JB004930) doi: <https://doi.org/10.1029/>  
1373 [2007JB004930](https://doi.org/10.1029/2007JB004930)
- 1374 Luo, Y., & Liu, Z. (2019). Rate-and-state model casts new insight into episodic  
1375 tremor and slow-slip variability in cascadia. *Geophysical Research Letters*,  
1376 *46*(12), 6352-6362. doi: <https://doi.org/10.1029/2019GL082694>
- 1377 Luo, Y., & Liu, Z. (2021). Fault zone heterogeneities explain depth-dependent pat-  
1378 tern and evolution of slow earthquakes in cascadia. *Nature Communications*,  
1379 *12*(1), 1959. doi: [10.1038/s41467-021-22232-x](https://doi.org/10.1038/s41467-021-22232-x)
- 1380 Lyakhovskiy, V., Ben-Zion, Y., & Agnon, A. (1997). Distributed damage, faulting  
1381 and friction. *Journal of Geophysical Research*, *102*(B12), 27635-27649.
- 1382 Lyakhovskiy, V., Ben-Zion, Y., & Agnon, A. (2001). Earthquake cycle, fault zones,  
1383 and seismicity patterns in a rheologically layered lithosphere. *Journal of Geo-*  
1384 *physical Research: Solid Earth*, *106*(B3), 4103-4120. Retrieved from [https://](https://agupubs.onlinelibrary.wiley.com/doi/abs/10.1029/2000JB900218)  
1385 [agupubs.onlinelibrary.wiley.com/doi/abs/10.1029/2000JB900218](https://agupubs.onlinelibrary.wiley.com/doi/abs/10.1029/2000JB900218) doi:  
1386 <https://doi.org/10.1029/2000JB900218>
- 1387 Lyakhovskiy, V., Reches, Z., Weinberger, R., & Scott, T. E. (1997). Non-linear elas-  
1388 tic behaviour of damaged rocks. *Geophysical Journal International*, *130*(1),  
1389 157-166. Retrieved from [https://onlinelibrary.wiley.com/doi/abs/](https://onlinelibrary.wiley.com/doi/abs/10.1111/j.1365-246X.1997.tb00995.x)  
1390 [10.1111/j.1365-246X.1997.tb00995.x](https://onlinelibrary.wiley.com/doi/abs/10.1111/j.1365-246X.1997.tb00995.x) doi: <https://doi.org/10.1111/>  
1391 [j.1365-246X.1997.tb00995.x](https://doi.org/10.1111/j.1365-246X.1997.tb00995.x)
- 1392 McLaskey, G. C., Thomas, A. M., Glaser, S. D., & Nadeau, R. M. (2012).  
1393 Fault healing promotes high-frequency earthquakes in laboratory experi-  
1394 ments and on natural faults. *Nature*, *491*(7422), 101-104. Retrieved from  
1395 <https://doi.org/10.1038/nature11512> doi: [10.1038/nature11512](https://doi.org/10.1038/nature11512)
- 1396 Michael, A. J. (2011). Random variability explains apparent global clustering  
1397 of large earthquakes. *Geophysical Research Letters*, *38*(21). Retrieved  
1398 from [https://agupubs.onlinelibrary.wiley.com/doi/abs/10.1029/](https://agupubs.onlinelibrary.wiley.com/doi/abs/10.1029/2011GL049443)  
1399 [2011GL049443](https://agupubs.onlinelibrary.wiley.com/doi/abs/10.1029/2011GL049443) doi: <https://doi.org/10.1029/2011GL049443>
- 1400 Nur, A., & Mavko, G. (1974). Postseismic viscoelastic rebound. *Science*, *183*(4121),  
1401 204-206. Retrieved from [https://www.science.org/doi/abs/10.1126/](https://www.science.org/doi/abs/10.1126/science.183.4121.204)  
1402 [science.183.4121.204](https://www.science.org/doi/abs/10.1126/science.183.4121.204) doi: [10.1126/science.183.4121.204](https://doi.org/10.1126/science.183.4121.204)
- 1403 Obara, K. (2002). Nonvolcanic deep tremor associated with subduction in south-  
1404 west japan. *Science*, *296*(5573), 1679-1681. Retrieved from [https://science](https://science.sciencemag.org/content/296/5573/1679)  
1405 [.sciencemag.org/content/296/5573/1679](https://science.sciencemag.org/content/296/5573/1679) doi: [10.1126/science.1070378](https://doi.org/10.1126/science.1070378)
- 1406 Obara, K., & Kato, A. (2016). Connecting slow earthquakes to huge earthquakes.  
1407 *Science*, *353*(6296), 253-257. Retrieved from [https://science.sciencemag](https://science.sciencemag.org/content/353/6296/253)  
1408 [.org/content/353/6296/253](https://science.sciencemag.org/content/353/6296/253) doi: [10.1126/science.aaf1512](https://doi.org/10.1126/science.aaf1512)
- 1409 Ólason, E., Rampal, P., & Dansereau, V. (2021). On the statistical properties of sea-  
1410 ice lead fraction and heat fluxes in the arctic. *The Cryosphere*, *15*(2), 1053-  
1411 1064. Retrieved from <https://tc.copernicus.org/articles/15/1053/2021/>  
1412 doi: [10.5194/tc-15-1053-2021](https://doi.org/10.5194/tc-15-1053-2021)
- 1413 Omori, F. (1894). On the aftershocks of earthquakes. *Journal of the College of Sci-*  
1414 *ence, Imperial University of Tokyo*, *7*, 111-120.
- 1415 Parisio, F., Vinciguerra, S., Kolditz, O., & Nagel, T. (2019). The brittle-  
1416 ductile transition in active volcanoes. *Scientific Reports*, *9*(1), 143. Re-  
1417 trieved from <https://doi.org/10.1038/s41598-018-36505-x> doi:  
1418 [10.1038/s41598-018-36505-x](https://doi.org/10.1038/s41598-018-36505-x)
- 1419 Payero, J. S., Kostoglodov, V., Shapiro, N., Mikumo, T., Iglesias, A., Pérez-Campos,  
1420 X., & Clayton, R. W. (2008). Nonvolcanic tremor observed in the mexi-  
1421 can subduction zone. *Geophysical Research Letters*, *35*(7), L07305. doi:  
1422 [10.1029/2007GL032877](https://doi.org/10.1029/2007GL032877)
- 1423 Peacock, S. M. (2009). Thermal and metamorphic environment of subduction

- 1424 zone episodic tremor and slip. *Journal of Geophysical Research: Solid Earth*,  
 1425 114(B8). Retrieved from [https://agupubs.onlinelibrary.wiley.com/doi/](https://agupubs.onlinelibrary.wiley.com/doi/abs/10.1029/2008JB005978)  
 1426 [abs/10.1029/2008JB005978](https://agupubs.onlinelibrary.wiley.com/doi/abs/10.1029/2008JB005978) doi: <https://doi.org/10.1029/2008JB005978>
- 1427 Peng, Z., & Gomberg, J. (2010). An integrated perspective of the continuum be-  
 1428 tween earthquakes and slow-slip phenomena. *Nature Geoscience*, 3, 599–607.  
 1429 doi: <https://doi.org/10.1038/ngeo940>
- 1430 Perfettini, H., & Avouac, J.-P. (2004). Postseismic relaxation driven by brittle  
 1431 creep: A possible mechanism to reconcile geodetic measurements and  
 1432 the decay rate of aftershocks, application to the chi-chi earthquake, tai-  
 1433 wan. *Journal of Geophysical Research: Solid Earth*, 109(B2). doi:  
 1434 <https://doi.org/10.1029/2003JB002488>
- 1435 Periollat, A., Radiguet, M., Weiss, J., Twardzik, C., Amitrano, D., Cotte, N., ...  
 1436 Socquet, A. (2022). Transient brittle creep mechanism explains early post-  
 1437 seismic phase of the 2011 tohoku-oki megathrust earthquake: Observations by  
 1438 high-rate gps solutions. *Journal of Geophysical Research: Solid Earth*, 127(8),  
 1439 e2022JB024005. doi: <https://doi.org/10.1029/2022JB024005>
- 1440 Poiata, N., Vilotte, J.-P., Shapiro, N. M., Supino, M., & Obara, K. (2021). Com-  
 1441 plexity of deep low-frequency earthquake activity in shikoku (japan) imaged  
 1442 from the analysis of continuous seismic data. *Journal of Geophysical Re-*  
 1443 *search: Solid Earth*, 126(11), e2021JB022138. doi: [https://doi.org/10.1029/](https://doi.org/10.1029/2021JB022138)  
 1444 [2021JB022138](https://doi.org/10.1029/2021JB022138)
- 1445 Poli, P. (2017). Creep and slip: Seismic precursors to the nuugaatsiaq landslide  
 1446 (greenland). *Geophysical Research Letters*, 44(17), 8832–8836. Retrieved  
 1447 from [https://agupubs.onlinelibrary.wiley.com/doi/abs/10.1002/](https://agupubs.onlinelibrary.wiley.com/doi/abs/10.1002/2017GL075039)  
 1448 [2017GL075039](https://agupubs.onlinelibrary.wiley.com/doi/abs/10.1002/2017GL075039) doi: <https://doi.org/10.1002/2017GL075039>
- 1449 Pollitz, F. F. (2003). Transient rheology of the uppermost mantle beneath the  
 1450 mojave desert, california. *Earth and Planetary Science Letters*, 215(1), 89 -  
 1451 104. Retrieved from [http://www.sciencedirect.com/science/article/pii/](http://www.sciencedirect.com/science/article/pii/S0012821X03004321)  
 1452 [S0012821X03004321](http://www.sciencedirect.com/science/article/pii/S0012821X03004321) doi: [https://doi.org/10.1016/S0012-821X\(03\)00432-1](https://doi.org/10.1016/S0012-821X(03)00432-1)
- 1453 Pollitz, F. F. (2005). Transient rheology of the upper mantle beneath central  
 1454 alaska inferred from the crustal velocity field following the 2002 denali earth-  
 1455 quake. *Journal of Geophysical Research: Solid Earth*, 110(B8). Retrieved  
 1456 from [https://agupubs.onlinelibrary.wiley.com/doi/abs/10.1029/](https://agupubs.onlinelibrary.wiley.com/doi/abs/10.1029/2005JB003672)  
 1457 [2005JB003672](https://agupubs.onlinelibrary.wiley.com/doi/abs/10.1029/2005JB003672) doi: <https://doi.org/10.1029/2005JB003672>
- 1458 Pollitz, F. F., Wicks, C., & Thatcher, W. (2001). Mantle flow beneath a  
 1459 continental strike-slip fault: Postseismic deformation after the 1999 hec-  
 1460 tor mine earthquake. *Science*, 293(5536), 1814–1818. Retrieved from  
 1461 <https://www.science.org/doi/abs/10.1126/science.1061361> doi:  
 1462 [10.1126/science.1061361](https://www.science.org/doi/abs/10.1126/science.1061361)
- 1463 Popov, A., & Sobolev, S. V. (2008). Slim3d: A tool for three-dimensional ther-  
 1464 momechanical modeling of lithospheric deformation with elasto-visco-plastic  
 1465 rheology. *Physics of the Earth and Planetary Interiors*, 171(1), 55–75. Re-  
 1466 trieved from [https://www.sciencedirect.com/science/article/pii/](https://www.sciencedirect.com/science/article/pii/S003192010800054X)  
 1467 [S003192010800054X](https://www.sciencedirect.com/science/article/pii/S003192010800054X) (Recent Advances in Computational Geodynam-  
 1468 ics: Theory, Numerics and Applications) doi: [https://doi.org/10.1016/](https://doi.org/10.1016/j.pepi.2008.03.007)  
 1469 [j.pepi.2008.03.007](https://doi.org/10.1016/j.pepi.2008.03.007)
- 1470 Radiguet, M., Cotton, F., Vergnolle, M., Campillo, M., Walpersdorf, A., Cotte, N.,  
 1471 & Kostoglodov, V. (2012). Slow slip events and strain accumulation in the  
 1472 guerrero gap, mexico. *Journal of Geophysical Research: Solid Earth*, 117(B4).  
 1473 Retrieved from [https://agupubs.onlinelibrary.wiley.com/doi/abs/](https://agupubs.onlinelibrary.wiley.com/doi/abs/10.1029/2011JB008801)  
 1474 [10.1029/2011JB008801](https://agupubs.onlinelibrary.wiley.com/doi/abs/10.1029/2011JB008801) doi: <https://doi.org/10.1029/2011JB008801>
- 1475 Radiguet, M., Perfettini, H., Cotte, N., & et al. (2016). Triggering of the 2014 Mw  
 1476 7.3 Papanoa earthquake by a slow slip event in guerrero, mexico. *Nature Geo-*  
 1477 *science*, 9, 829–833. doi: <https://doi.org/10.1038/ngeo2817>
- 1478 Rampal, P., Dansereau, V., Olason, E., Bouillon, S., Williams, T., Korosov, A.,

- 1479 & Samaké, A. (2019). On the multi-fractal scaling properties of sea  
 1480 ice deformation. *The Cryosphere*, *13*(9), 2457–2474. Retrieved from  
 1481 <https://tc.copernicus.org/articles/13/2457/2019/> doi: 10.5194/  
 1482 tc-13-2457-2019
- 1483 Renard, F., Gratier, J.-P., & Jamtveit, B. (2000). Kinetics of crack-sealing, in-  
 1484 tergranular pressure solution, and compaction around active faults. *Jour-  
 1485 nal of Structural Geology*, *22*(10), 1395–1407. Retrieved from [https://  
 1486 www.sciencedirect.com/science/article/pii/S019181410000064X](https://www.sciencedirect.com/science/article/pii/S019181410000064X) doi:  
 1487 [https://doi.org/10.1016/S0191-8141\(00\)00064-X](https://doi.org/10.1016/S0191-8141(00)00064-X)
- 1488 Rivet, D., Campillo, M., Shapiro, N. M., Cruz-Atienza, V., Radiguet, M., Cotte, N.,  
 1489 & Kostoglodov, V. (2011). Seismic evidence of nonlinear crustal deforma-  
 1490 tion during a large slow slip event in Mexico. *Geophysical Research Letters*,  
 1491 *38*(8). Retrieved from [https://agupubs.onlinelibrary.wiley.com/doi/  
 1492 abs/10.1029/2011GL047151](https://agupubs.onlinelibrary.wiley.com/doi/abs/10.1029/2011GL047151) doi: <https://doi.org/10.1029/2011GL047151>
- 1493 Rogers, G., & Dragert, H. (2003). Episodic tremor and slip on the Cascadia subduc-  
 1494 tion zone: The chatter of silent slip. *Science*, *300*(5627), 1942–1943. Retrieved  
 1495 from <http://www.jstor.org/stable/3834528>
- 1496 Royden, L. H., Burchfiel, B. C., King, R. W., Wang, E., Chen, Z., Shen, F., & Liu,  
 1497 Y. (1997). Surface Deformation and Lower Crustal Flow in Eastern Tibet.  
 1498 *Science*, *276*(5313), 788–790. doi: 10.1126/science.276.5313.788
- 1499 Ruina, A. (1983). Slip instability and state variable friction laws. *Journal  
 1500 of Geophysical Research: Solid Earth*, *88*(B12), 10359–10370. Retrieved  
 1501 from [https://agupubs.onlinelibrary.wiley.com/doi/abs/10.1029/  
 1502 JB088iB12p10359](https://agupubs.onlinelibrary.wiley.com/doi/abs/10.1029/JB088iB12p10359) doi: <https://doi.org/10.1029/JB088iB12p10359>
- 1503 Saramito, P. (2020). *Efficient c++ finite element computing with rheolef*. CNRS-  
 1504 CCSD ed. (<http://hal.archives-ouvertes.fr/cel-00573970>)
- 1505 Savage, J., Svarc, J., & Yu, S.-B. (2005). Postseismic relaxation and transient creep.  
 1506 *Journal of Geophysical Research: Solid Earth*, *110*(B11).
- 1507 Scholz, C. H. (1998). Earthquakes and friction laws. *Nature*, *391*, 37–42.
- 1508 Segall, P., & Bradley, A. M. (2012). The Role of Thermal Pressurization and Di-  
 1509 latancy in Controlling the Rate of Fault Slip. *Journal of Applied Mechanics*,  
 1510 *79*(3). Retrieved from <https://doi.org/10.1115/1.4005896> (031013) doi:  
 1511 10.1115/1.4005896
- 1512 Segall, P., & Rice, J. R. (1995). Dilatancy, compaction, and slip instability of a  
 1513 fluid-infiltrated fault. *Journal of Geophysical Research: Solid Earth*, *100*(B11),  
 1514 22155–22171. Retrieved from [https://agupubs.onlinelibrary.wiley.com/  
 1515 doi/abs/10.1029/95JB02403](https://agupubs.onlinelibrary.wiley.com/doi/abs/10.1029/95JB02403) doi: <https://doi.org/10.1029/95JB02403>
- 1516 Seydoux, L., Balestrieri, R., Poli, P., de Hoop, M., Campillo, M., & Baraniuk, R.  
 1517 (2020). Clustering earthquake signals and background noises in continuous  
 1518 seismic data with unsupervised deep learning. *Nature Communications*, *11*(1),  
 1519 3972. Retrieved from <https://doi.org/10.1038/s41467-020-17841-x> doi:  
 1520 10.1038/s41467-020-17841-x
- 1521 Shapiro, N. M., Campillo, M., Kaminski, E., Vilotte, J.-P., & Jaupart, C. (2018).  
 1522 Low-frequency earthquakes and pore pressure transients in subduction zones.  
 1523 *Geophysical Research Letters*, *45*(20), 11,083–11,094. doi: [https://doi.org/  
 1524 10.1029/2018GL079893](https://doi.org/10.1029/2018GL079893)
- 1525 Shcherbakov, R., Turcotte, D. L., & Rundle, J. B. (2005). Aftershock statistics. *Pure  
 1526 and applied geophysics*, *162*(6), 1051–1076.
- 1527 Shelly, D. R., Beroza, G. C., Ide, S., & Nakamura, S. (2006). Low-frequency earth-  
 1528 quakes in Shikoku, Japan, and their relationship to episodic tremor and slip.  
 1529 *Nature*, *442*(7099), 188–191. doi: 10.1038/nature04931
- 1530 Sibson, R. H. (1992). Implications of fault-valve behaviour for rupture nucle-  
 1531 ation and recurrence. *Tectonophysics*, *211*(1), 283–293. Retrieved from  
 1532 <http://www.sciencedirect.com/science/article/pii/004019519290065E>  
 1533 doi: [https://doi.org/10.1016/0040-1951\(92\)90065-E](https://doi.org/10.1016/0040-1951(92)90065-E)

- 1534 Siravo, G., Faccenna, C., G erault, M., Becker, T. W., Fellin, M. G., Herman, F., &  
 1535 Molin, P. (2019). Slab flattening and the rise of the eastern cordillera, colombia.  
 1536 *Earth and Planetary Science Letters*, 512, 100 - 110. Retrieved from  
 1537 <http://www.sciencedirect.com/science/article/pii/S0012821X19300925>  
 1538 doi: <https://doi.org/10.1016/j.epsl.2019.02.002>
- 1539 Sun, T., & Wang, K. (2015). Viscoelastic relaxation following subduction earth-  
 1540 quakes and its effects on afterslip determination. *Journal of Geophysi-  
 1541 cal Research: Solid Earth*, 120(2), 1329-1344. Retrieved from [https://  
 1542 agupubs.onlinelibrary.wiley.com/doi/abs/10.1002/2014JB011707](https://agupubs.onlinelibrary.wiley.com/doi/abs/10.1002/2014JB011707) doi:  
 1543 <https://doi.org/10.1002/2014JB011707>
- 1544 Tang, C. (1997). Numerical simulation of progressive rock failure and associated  
 1545 seismicity. *International Journal of Rock Mechanics and Mining Sciences*,  
 1546 34(2), 249-261.
- 1547 Turcotte, D. L. (1992). *Fractals and chaos in geology and geophysics*. New York, NY,  
 1548 USA: Cambridge University Press.
- 1549 Turcotte, D. L., Newman, W. I., & Shcherbakov, R. (2003). Micro and macroscopic  
 1550 models of rock fracture. *Geophysical Journal International*, 152, 718-728.
- 1551 van den Ende, M., Chen, J., Ampuero, J.-P., & Niemeijer, A. (2018). A comparison  
 1552 between rate-and-state friction and microphysical models, based on numeri-  
 1553 cal simulations of fault slip. *Tectonophysics*, 733, 273 - 295. Retrieved from  
 1554 <http://www.sciencedirect.com/science/article/pii/S0040195117305024>  
 1555 (Physics of Earthquake Rupture Propagation) doi: [https://doi.org/10.1016/  
 1556 j.tecto.2017.11.040](https://doi.org/10.1016/j.tecto.2017.11.040)
- 1557 Wang, K., Hu, Y., & He, J. (2012). Deformation cycles of subduction earthquakes  
 1558 in a viscoelastic Earth. *Nature*, 484, 327-332. doi: [https://doi.org/10.1038/  
 1559 nature11032](https://doi.org/10.1038/nature11032)
- 1560 Wang, Q.-Y., Campillo, M., Brenguier, F., Lecointre, A., Takeda, T., & Hashima, A.  
 1561 (2019). Evidence of changes of seismic properties in the entire crust beneath  
 1562 japan after the mw 9.0, 2011 tohoku-oki earthquake. *Journal of Geophys-  
 1563 ical Research: Solid Earth*, 124(8), 8924-8941. Retrieved from [https://  
 1564 agupubs.onlinelibrary.wiley.com/doi/abs/10.1029/2019JB017803](https://agupubs.onlinelibrary.wiley.com/doi/abs/10.1029/2019JB017803) doi:  
 1565 <https://doi.org/10.1029/2019JB017803>
- 1566 Wech, A. G., & Creager, K. C. (2011). A continuum of stress, strength and slip in  
 1567 the cascadia subduction zone. *Nature Geoscience*, 4(9), 624-628. doi: 10.1038/  
 1568 ngeo1215
- 1569 Weiss, J., & Dansereau, V. (2017). Linking scales in sea ice mechanics.  
 1570 *Philosophical Transaction Royal Society A: Mathematical, Physical and  
 1571 Engineering Sciences*, 375(2086), 20150352. Retrieved from [http://  
 1572 rsta.royalsocietypublishing.org/content/375/2086/20150352](http://rsta.royalsocietypublishing.org/content/375/2086/20150352) doi:  
 1573 10.1098/rsta.2015.0352
- 1574 Williams, R. T., Davis, J. R., & Goodwin, L. B. (2019). Do large earthquakes oc-  
 1575 cur at regular intervals through time? a perspective from the geologic record.  
 1576 *Geophysical Research Letters*, 46(14), 8074-8081. Retrieved from [https://  
 1577 agupubs.onlinelibrary.wiley.com/doi/abs/10.1029/2019GL083291](https://agupubs.onlinelibrary.wiley.com/doi/abs/10.1029/2019GL083291) doi:  
 1578 <https://doi.org/10.1029/2019GL083291>
- 1579 Williams, R. T., Mozley, P. S., Sharp, W. D., & Goodwin, L. B. (2019). U-th dating  
 1580 of syntectonic calcite veins reveals the dynamic nature of fracture cementa-  
 1581 tion and healing in faults. *Geophysical Research Letters*, 46(22), 12900-12908.  
 1582 Retrieved from [https://agupubs.onlinelibrary.wiley.com/doi/abs/  
 1583 10.1029/2019GL085403](https://agupubs.onlinelibrary.wiley.com/doi/abs/10.1029/2019GL085403) doi: <https://doi.org/10.1029/2019GL085403>
- 1584 Williams, T., Korosov, A., Rampal, P., & Olason, E. (2019). Presentation and eval-  
 1585 uation of the Arctic sea ice forecasting system neXtSIM-F. *The Cryosphere  
 1586 Discussions*, 2019, 1-31. Retrieved from [https://tc.copernicus.org/  
 1587 preprints/tc-2019-154/](https://tc.copernicus.org/preprints/tc-2019-154/) doi: 10.5194/tc-2019-154

# Supporting Information for "Modeling Multi-Scale Deformation Cycles in Subduction Zones with a Continuum Visco-Elastic-Brittle Framework"

Véronique Dansereau<sup>1</sup>, Nikolai Shapiro<sup>1</sup>, Michel Campillo<sup>1</sup>, Jérôme Weiss<sup>1</sup>

<sup>1</sup>Institut des Sciences de la Terre, Université Grenoble Alpes, CNRS (5275), Grenoble, France

**Contents of this file Additional Supporting Information (Files uploaded separately)**

1. Captions for Movie S1

**Introduction** The movie provided as Supporting Information is an animation of the numerical model simulation results that supplements the description of the model mechanical response provided in section 5.1. The simulation is ran with a specific set of model parameters, but the main features of this mechanical response are also observed over a range of parameter values.

## **Movie S1.**

Animation of the numerical simulation results obtained using the following model mechanical parameters:  $De_0 = 0.001$ ,  $T_h = 10^{-5}$ ,  $\tilde{\Delta}t = 10^{-10}$ ,  $\alpha = 4$ ,  $\delta d = 0.1$ , and corresponding to the snapshots and time series presented in figure 5, described in section 5.1. The upper panel represents the temporal evolution of the field of level of damage,  $d$  (in logarithmic scale) and the lower panel, the corresponding temporal evolution of the macro-

---

scopic shear stress, calculated by integrating the shear stress on the entire top boundary of the domain (black curve) and of the macroscopic damage increment, calculated as in equation (17) (grey curve).